C 52.15: ERL 176-ESL9

ESSA TR ERL 176-ESL 9

A UNITED STATES DEPARTMENT OF COMMERCE PUBLICATION

ESSA Technical Report ERL 176-ESL 9

U.S. DEPARTMENT OF COMMERCE
Environmental Science Services Administration
Research Laboratories

Norsar Microseisms

JAMES N. MURDOCK

JOHN H. PFLUKE

BOULDER, COLO.
JULY 1970

PENNSYLVANIA STATE UNIVERSITY
DOCUMENTS COLLECTION

ESSA RESEARCH LABORATORIES

The mission of the Research Laboratories is to study the oceans, inland waters, the lower and upper atmosphere, the space environment, and the earth, in search of the understanding needed to provide more useful services in improving man's prospects for survival as influenced by the physical environment. Laboratories contributing to these studies are:

Earth Sciences Laboratories: Geomagnetism, seismology, geodesy, and related earth sciences; earthquake processes, internal structure and accurate figure of the Earth, and distribution of the Earth's mass.

Atlantic Oceanographic and Meteorological Laboratories: Oceanography, with emphasis on the geology and geophysics of ocean basins, oceanic processes, sea-air interactions, hurricane research, and weather modification (Miami, Florida).

Pacific Oceanographic Laboratories: Oceanography; geology and geophysics of the Pacific Basin and margins; oceanic processes and dynamics; tsunami generation, propagation, modification, detection, and monitoring (Seattle, Washington).

Atmospheric Physics and Chemistry Laboratory: Cloud physics and precipitation; chemical composition and nucleating substances in the lower atmosphere; and laboratory and field experiments toward developing feasible methods of weather modification.

Air Resources Laboratories: Diffusion, transport, and dissipation of atmospheric contaminants; development of methods for prediction and control of atmospheric pollution (Silver Spring, Maryland).

Geophysical Fluid Dynamics Laboratory: Dynamics and physics of geophysical fluid systems; development of a theoretical basis, through mathematical modeling and computer simulation, for the behavior and properties of the atmosphere and the oceans (Princeton, New Jersey).

National Severe Storms Laboratory: Tornadoes, squall lines, thunderstorms, and other severe local convective phenomena toward achieving improved methods of forecasting, detecting, and providing advance warnings (Norman, Oklahoma).

Space Disturbances Laboratory: Nature, behavior, and mechanisms of space disturbances; development and use of techniques for continuous monitoring and early detection and reporting of important disturbances.

Aeronomy Laboratory: Theoretical, laboratory, rocket, and satellite studies of the physical and chemical processes controlling the ionosphere and exosphere of the earth and other planets.

Wave Propagation Laboratory: Development of new methods for remote sensing of the geophysical environment; special emphasis on propagation of sound waves, and electromagnetic waves at millimeter, infrared, and optical frequencies.

Institute for Telecommunication Sciences: Central federal agency for research and services in propagation of radio waves, radio properties of the earth and its atmosphere, nature of radio noise and interference, information transmission and antennas, and methods for the more effective use of the radio spectrum for telecommunications.

Research Flight Facility: Outfits and operates aircraft specially instrumented for research; and meets needs of ESSA and other groups for environmental measurements for aircraft (Miami, Florida).

ENVIRONMENTAL SCIENCE SERVICES ADMINISTRATION

BOULDER, COLORADO 80302

U. S. DEPARTMENT OF COMMERCE
Maurice H. Stans, Secretary

ENVIRONMENTAL SCIENCE SERVICES ADMINISTRATION
Robert M. White, Administrator

RESEARCH LABORATORIES
Wilmot N. Hess, Director

ESSA TECHNICAL REPORT ERL 176-ESL 9

Norsar Microseisms

JAMES N. MURDOCK

JOHN H. PFLUKE

This work was sponsored by the Advanced Research Projects Agency under ARPA Order No. 800, Amendment No. 11.

EARTH SCIENCES LABORATORIES
BOULDER, COLORADO
July 1970

For sale by the Superintendent of Documents, U. S. Government Printing Office, Washington, D. C. 20402
Price $1.75

U. S. Depository Copy

The Research Laboratories of the Environmental Science Services Administration do not approve, recommend, or endorse any product, and the results reported in this document shall not be used in advertising or sales promotion, or in any manner to indicate, either implicitly or explicitly, endorsement by the United States Government of any specific product or manufacturer.

CONTENTS

1. INTRODUCTION 1

2. NORWAY OPERATIONS AND PRECISION OF THE DATA 2
   2.1 Data Acquisition 2
   2.2 Precision of the Data 5
   2.3 Production of Seismograms in Norway 9

3. DIFFERENCES BETWEEN THE SURFACE AND SUBSURFACE SEISMIC FIELDS 12
   3.1 Microseisms 12
   3.2 Seismic Signals 22
   3.3 Other Observations 22

4. PARAMETERS OF THE TIME-VARYING MICROSEISMIC FIELD 24
   4.1 Estimates by Analog Techniques 24
   4.2 Estimates by Digital Techniques 25
   4.3 Statistical Properties of the Data 28

5. COHERENCE OF MICROSEISMS 33
   5.1 Data Reduction and Construction of Displays 33
   5.2 Observed Sample Coherence 34
   5.3 Model of the Coherence Variations 46
   5.4 Comparison of Models with Observations 52
   5.5 Time Parameters of the Model 56

6. MICROSEISM AND METEOROLOGICAL CONDITIONS 59
   6.1 Correlation of Meteorological Activity with Time-Varying Microseismic Trends 59
   6.2 Discussion 74

7. OBSERVED EARTHQUAKE SIGNALS 75
   7.1 Data Reduction Techniques 75
   7.2 NORSAR Detection Threshold for Teleseisms 76
   7.3 Average Signal Frequencies of Teleseisms 79
   7.4 Discussion 79

8. SUMMARY 83

9. ACKNOWLEDGMENTS 84

10. REFERENCES 86

APPENDIX 87

ABSTRACT

Spectral density and coherence estimates, depicting seismic noise recorded at the Norway Seismic Array by the Earthquake Mechanism Laboratory, show the following for the P signal band: (1) the difference between the surface microseism field and that sensed in a 60-m well is normally less than 1 dB, even at times of high wind velocities; (2) the coherence between adjacent subarray sensors is quite small.

The coherence of microseisms, particularly at frequencies of 0.1 to 0.6 Hz, shows a strong azimuthal dependency. At lower frequencies, the estimated coherence is greatest in the direction of apparent propagation, perhaps indicating that the noise field is a propagating interference pattern. A mathematical model of the coherence of the postulated interference process agrees qualitatively with the observations.

Analog and digital estimates, produced to describe the time-varying microseism trends, demonstrate that the noise field is approximately space stationary at the eight center subarrays. There is a weak correlation between time-varying barometric gradients and time-varying microseisms for the bands near 0.3 and 1.0 Hz.

For epicentral distances of 20 to 90°, the single seismometer P detection threshold ranges from approximately 4.3 to 5.4 m_b. Earthquakes perceived showed P waves predominantly in the 0.8- to 2.0-Hz band. Signal frequency increases as a function of decreasing magnitude.

Key Words: coherence of microseisms, interference patterns, microseisms and atmospheric conditions, NORSAR, Norway Seismic Array, detection threshold for teleseisms, spectral analyses of interference processes, spectral estimates of microseisms, surface and subsurface seismic fields.

NORSAR MICROSEISMS

James N. Murdock and John H. Pfluke

1. INTRODUCTION

The Earthquake Mechanism Laboratory (EML), an Environmental Science Services Administration (ESSA) research facility, was requested by the Advanced Research Projects Agency (ARPA) to perform tests on instrumentation installed in Norway during the winter of 1968-1969 (the Norway Seismic Array Project). The EML participation is monitored by the Electronics System Division (ESD) of the United States Air Force. Primary objectives of our study program were: (1) to describe the difference between seismic activity sensed in a shallow (60 m) well and at the surface directly above, and (2) to describe the coherence of microseisms recorded by sensors emplaced 2 km to 6 km apart. Secondary objectives included descriptions of the time-varying microseism field and its correlation with meteorological conditions.

This paper describes the EML field operations in Norway and presents interpretations of data gathered at the Norway Seismic Array (NORSAR) facility. In section 2 we show map positions of the field installations, describe the chronology of operations in Norway, and comment on the precision of the data. Section 3 presents differences in the seismic field observed from simultaneous recordings of surface and subsurface activity; section 4 describes time-varying microseism trends; section 5 presents both microseism coherence estimates and our hypothetical noise model. Section 6 gives a description of meteorological conditions

correlated with microseism amplitudes. Section 7 describes the earthquake signal frequencies observed and gives an estimate of detection threshold for a single NORSAR seismometer. Observations and interpretations are summarized in section 8. The appendix describes instrumentation used, outlines digital data reduction techniques, and presents seismograms recorded during times of high wind.

2. NORWAY OPERATIONS AND PRECISION OF THE DATA

2.1 Data Acquisition

When completed, the NORSAR instrument will consist of two concentric rings of subarrays (named B and C) centered on the subarray 01A. Seismometers, amplifiers, and signal cables for the subarrays 01A and 01B to 07B (see fig. 2.1) were emplaced by NORSAR contractors during the fall of 1968 and the winter of 1968-1969. Each subarray consists of a central terminal vault (CTV), a long-period seismometer vault (LPV), and six permanent short-period (1.0 Hz free-period) vertical seismometer installations. The CTV, LPV, and a short-period seismometer emplaced in a 60-m well occupy a common position in each subarray. A seventh short-period vertical seismometer was emplaced in the LPV to allow simultaneous descriptions of the surface and subsurface seismic fields. The EML signal processing and recording instruments were emplaced in the central terminal vaults (see fig. 2.2 and app.) to acquire information from the seismometer positioned in the well, in the LPV, and from four remote subarray seismometers. Because high winds might produce noise at the surface that would be attenuated at depth, anemometers

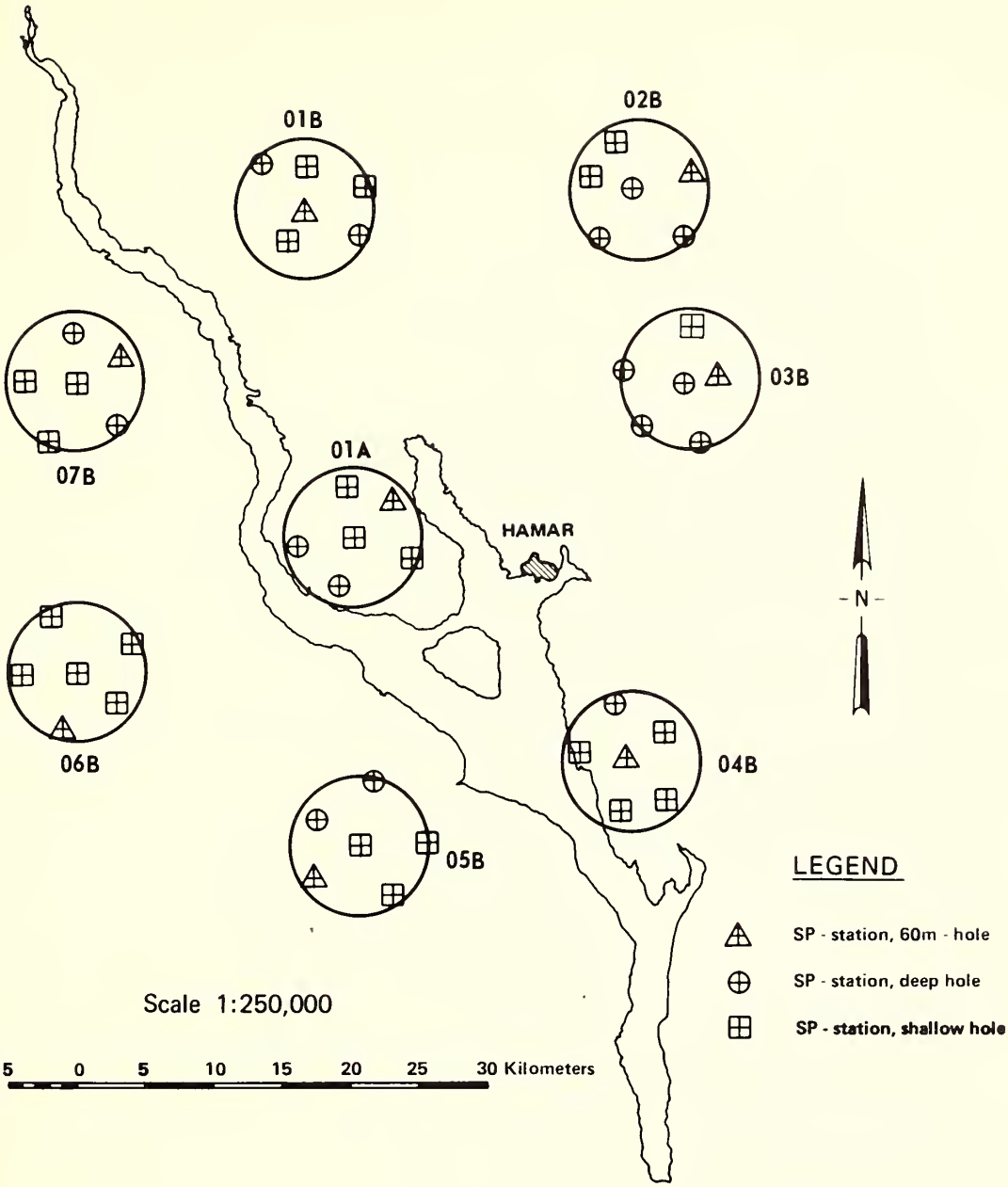

Figure 2.1. The NORSAR subarrays 01A and 01B to 07B. Hamar is approximately 130 km north of Oslo, Norway.

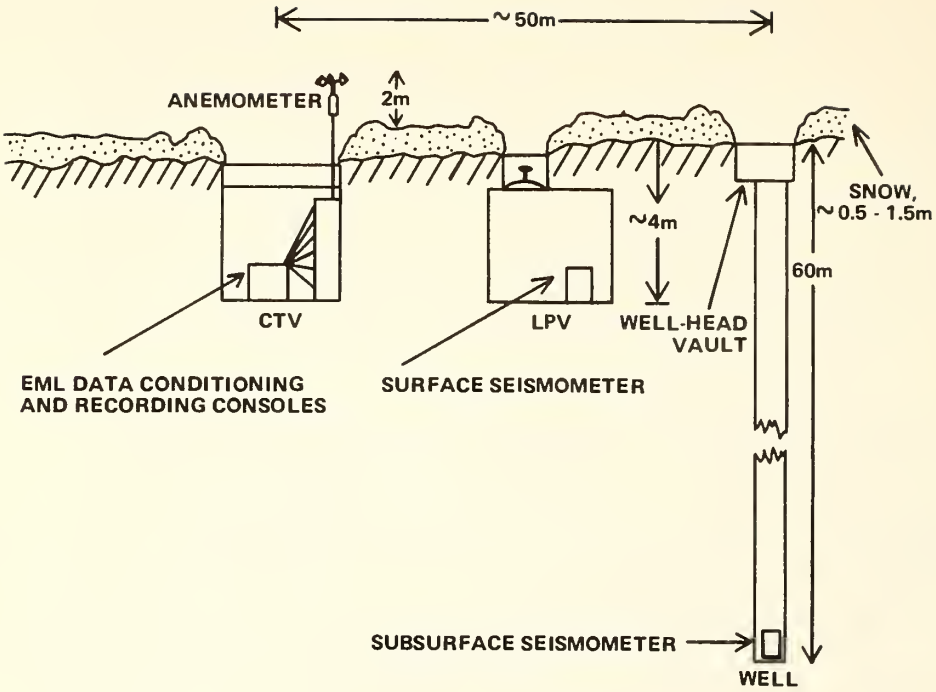

Figure 2.2. Artist's concept of the CTV-LPV-well area.

were installed (fig. 2.2) to provide continuous wind velocity information.

During the first week of January 1969, EML occupied positions 01A, 01B, and 04B (fig. 2.1). In mid-January, EML in addition occupied positions 02B and 03B. In late February, the instruments at 01A, 01B, and 04B were moved to positions 05B, 06B, and 07B. We operated EML instruments at positions in the B ring until early April 1969. Figure 2.3 depicts the history of operations and also indicates periods during which significant malfunctions occurred. During the operational period, one NORSAR seismic data amplifier and one NORSAR seismometer failed. The EML instrumental malfunctions we judge significant included two tape recorder stoppages, several instances of tape recorder spiking, and EML amplifier gain drift at position 06B.

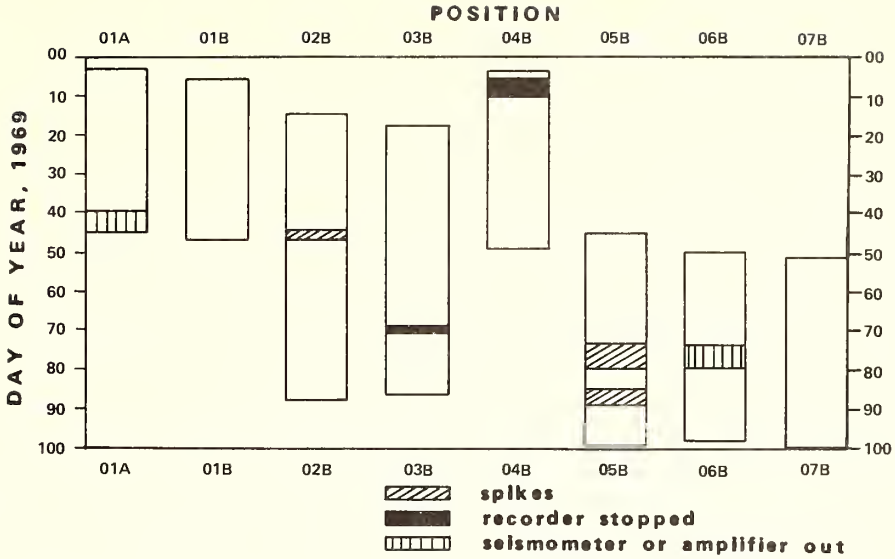

Figure 2.3. History of operations and intervals of malfunctions.

2.2 Precision of the Data

The following calibrations and tests were normally conducted by the field party for each element being monitored (see app. for more details):

(1) seismometer frequency response calibrations (one calibration per 10-day magnetic tape),

(2) seismic data amplifier frequency response calibrations (one calibration per 10-day magnetic tape),

(3) electrical analog calibrations of the anemometer channel (one for each EML instrument package), and

(4) system noise tests (one at the beginning and one at the end of each 10-day magnetic tape).

Referenced to the first applied calibration signal, from field recordings and field logs, we estimate the NORSAR seismic data amplifiers to have normally drifted less than 5 percent (at 1.0 Hz) during a 40-day recording period. From laboratory playback displays, we estimate the entire NORSAR system plus the entire EML system to have normally drifted less than 8 percent at a typical subarray. Drifts of 30 percent were observed for the EML amplifier positioned at 06B; this amplifier was replaced on day 089.

From the field anemometer channel calibrations, and from a wind tunnel test conducted at the manufacturer's laboratory, we believe most of our estimated average wind velocities are accurate to within several miles per hour.

We used two different digital data reduction techniques: one primarily for spectral density estimates, and another for coherence estimates; both are described in the appendix. For the spectral density estimates, a typical system noise sample is compared with a typical microseism spectral density estimate in figure 2.4. For the coherence estimates, figure 2.5 shows the spectral density estimate of a system noise sample, believed to depict the worst-case system noise, compared with a typical microseism spectral density estimate. In figure 2.4, peaks in system noise approach the microseismic level at 2.8 Hz; this noise peak may have been caused by the EML tape recorder. The peak at 0.6 Hz was introduced primarily in the digitizing process. From redundant processing of microseism samples, we have found errors as high as 3 dB caused by the 0.6-Hz noise peak, a noise common to all magnetic

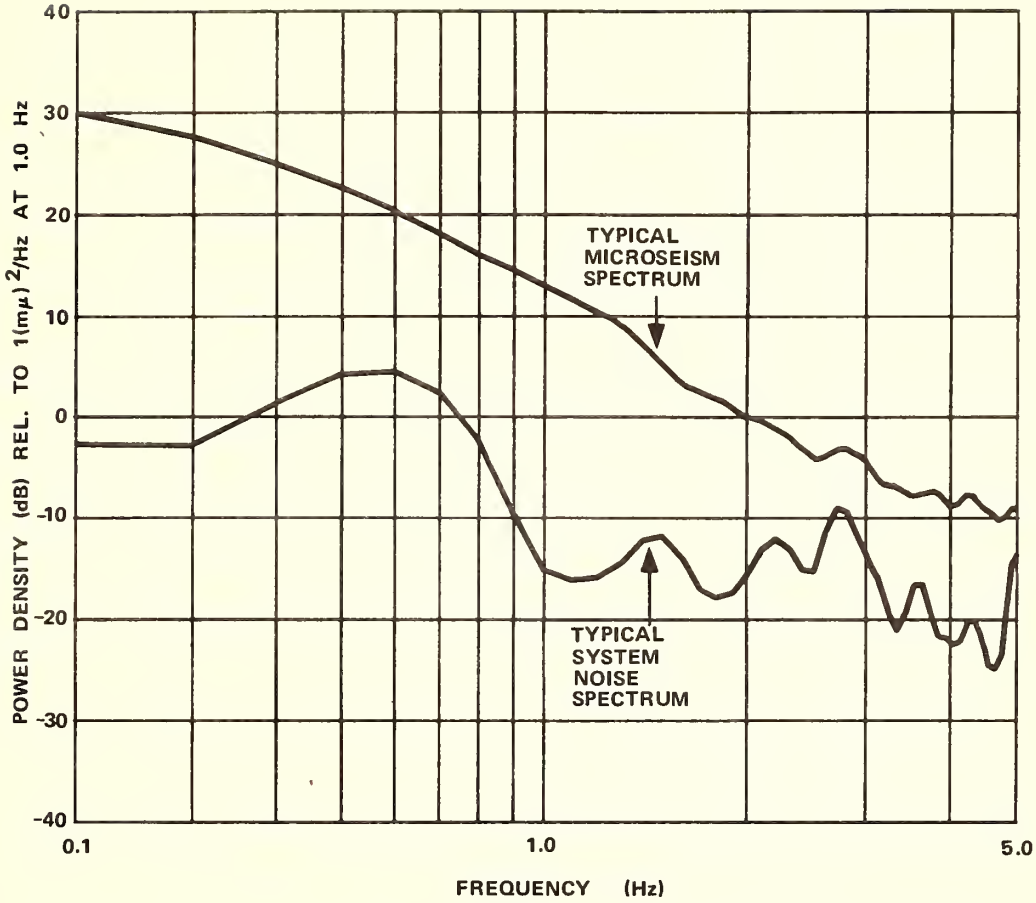

Figure 2.4. Typical spectral density estimate of a microseism sample compared with a spectral density estimate of system noise.

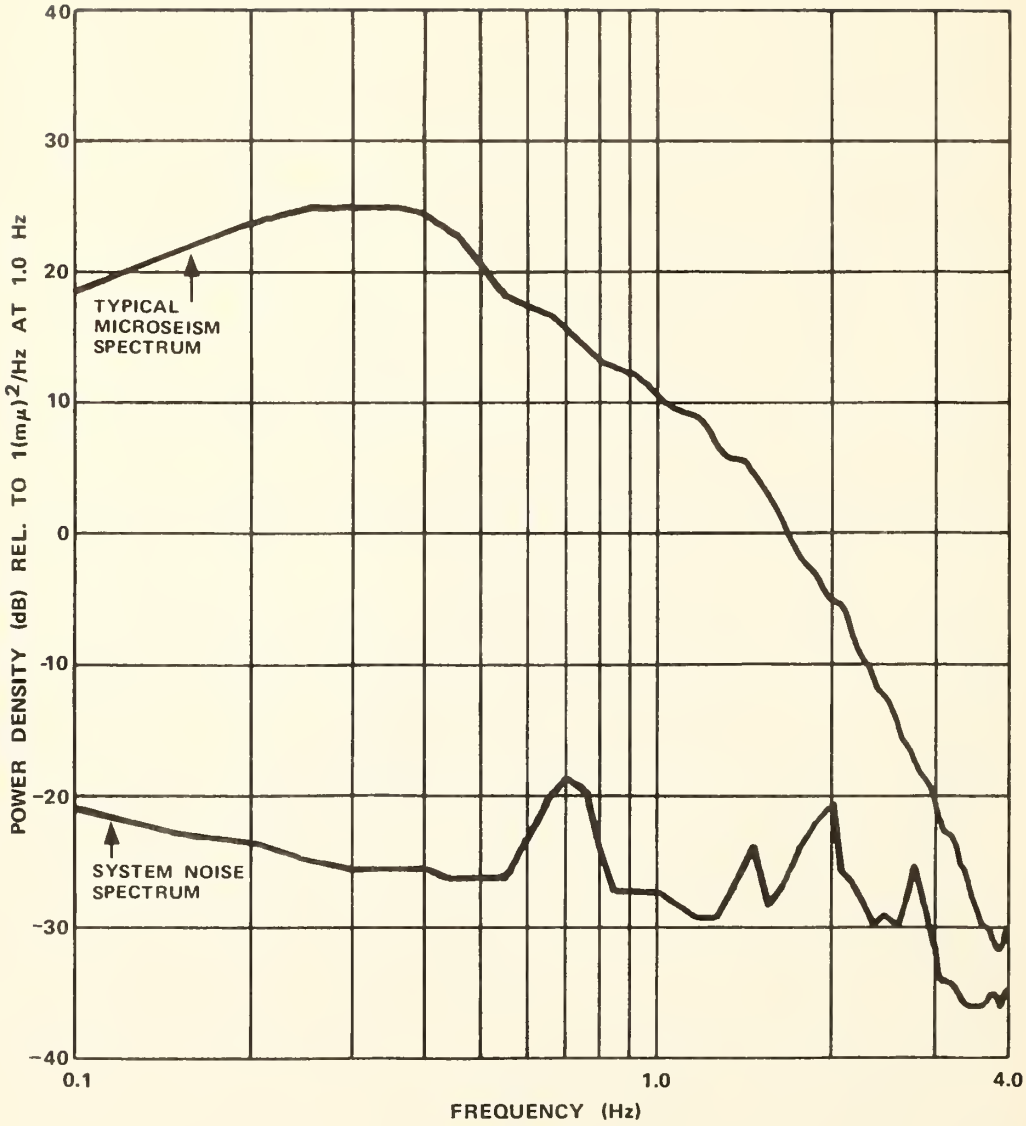

Figure 2.5. Typical spectral density estimate of a microseism sample used for coherence estimates compared with spectral density estimate of system noise.

tape channels. Figure 2.5 shows a signal-to-noise ratio of more than 30 dB for the 0.1- to 1.0-Hz band, and more than 15 dB for the 1.0- to 2.0-Hz band.

Our method of comparing two different time series, described in the appendix, can produce significant bias if large delays exist between the series (see Jenkins and Watts, 1968, p. 399). To estimate the bias in our computations, caused by time delays, we selected a pair of seismograms whose cross-correlation function showed a peak at 1.2 s (representative of the larger offsets observed in our data). One of the time series was translated 1.2 s to make the cross-correlation peak occur at the zero lag position. Coherence estimates for the translated and untranslated sets, compared in figure 2.6, show that the two agree to within 0.1.

2.3 Production of Seismograms in Norway

Professor Markvard Sellevoll, Director of the seismological observatory at the University of Bergen, kindly made playback facilities available for our use at Bergen. At the playback facility (fig. 2.7) we performed the following:

(1) Produced paper seismograms from our field magnetic tape recordings at 7-hour real time intervals (see app. for frequency response of the EML-University of Bergen system).

(2) Monitored the filtered output of a surface seismometer channel with two root-mean-square voltmeters; one meter

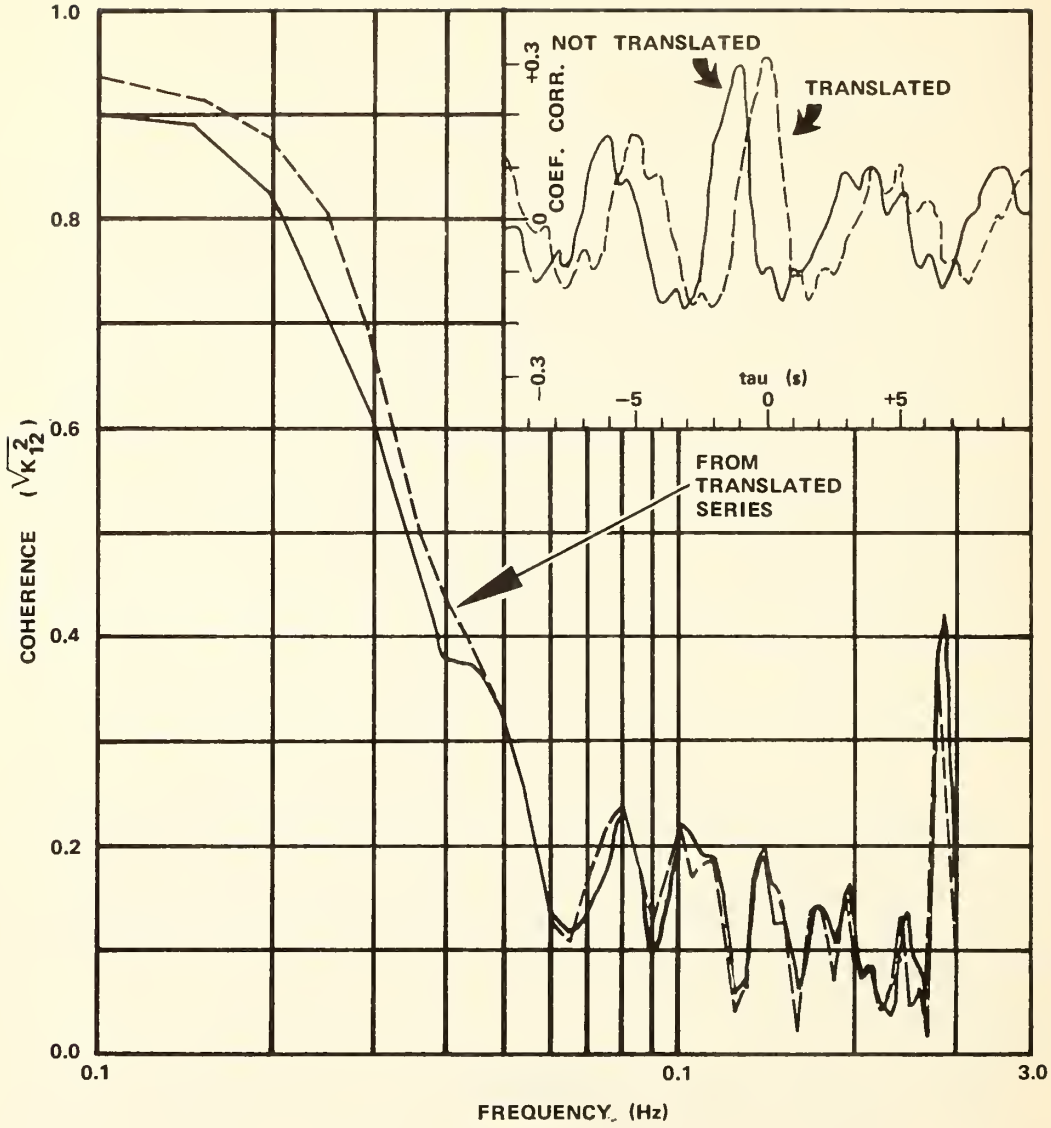

Figure 2.6. Bias in coherence estimates caused by off-centered correlation function. The bias is the difference between estimate of the centered (translated) series and that of the off-centered (not translated) series.

displayed the output bandpass filtered at 1.0 Hz real time; the second, at 0.3 Hz. Logs were made of the meter readings at 7-hour real-time intervals.

(3) Monitored the anemometer channel at 7-hour intervals by using a counter to display the frequency of the anemometer output. The anemometer produces a signal whose frequency was proportional to wind velocity.

Paper seismograms made at the University of Bergen will be referred to in this report as "seismograms having a time base of 3 mm/s" or words to this effect.

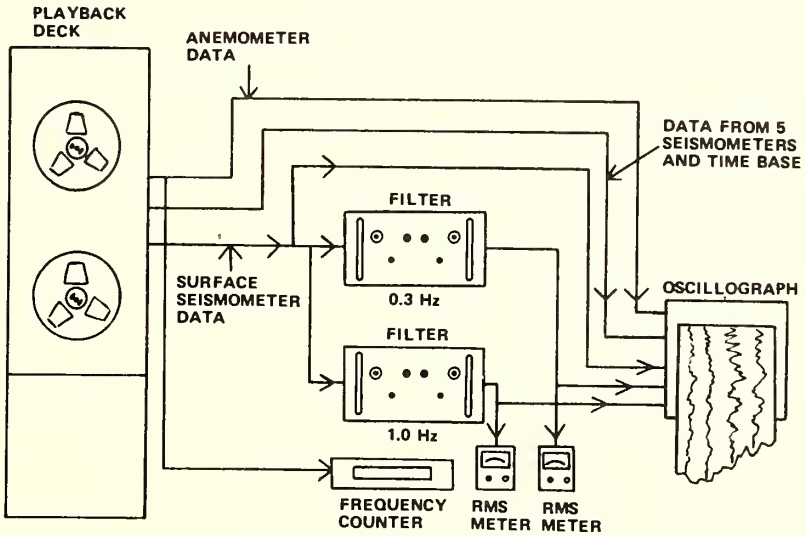

Figure 2.7. Artist's concept of playback operations at the University of Bergen.

3. DIFFERENCES BETWEEN THE SURFACE AND SUBSURFACE SEISMIC FIELDS

3.1 Microseisms

To describe the differences between the surface and subsurface microseismic fields, we computed spectral density estimates from seismic data recorded simultaneously by the subsurface and surface sensors (see fig. 2.2 for their relative positions). Data were chosen for spectral analyses to include samples of (1) recordings made during times of both high and low wind velocity and (2) recordings made during times of both high and low microseismic activity (see fig. 3.1). Techniques for producing the spectral estimates are outlined in the appendix. Also for each subsurface-surface pair, the frequency response and magnification of the subsurface sensor were normalized to those of the surface sensor. All adjustments were made from field-recorded calibrations, and we believe that the precision of the normalizations is within 1 dB.

Plots showing the differences between the spectra, estimated from the simultaneous recordings, are given in figures 3.2 to 3.9. The plots depict the surface power spectral density estimate minus the sub-surface power spectral density estimate, expressed in decibels. Wind velocities, recorded during the time frame used for each spectral estimate, are also indicated. In general, the illustrations demonstrate that there is only a small difference between the surface and subsurface recordings, even during times of high wind velocity. These data, summarized in histograms and graphs of cumulative probability distribution in figures 3.10 and 3.11, show that 97 percent of the 71 estimates produce differences of less than 3 dB. For recordings made during high wind velocities, 88 percent show

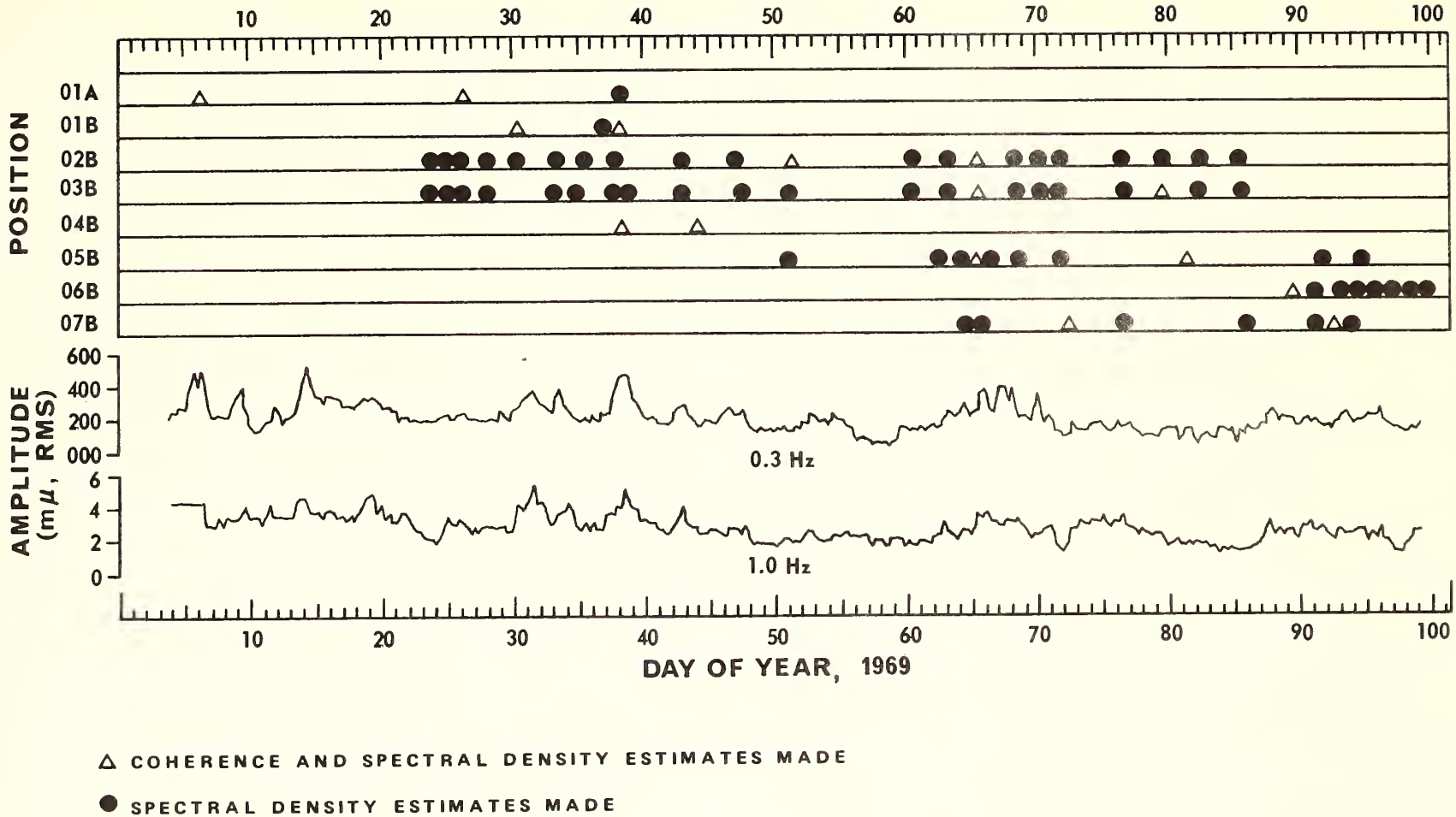

Figure 3.1. Distribution of power spectral density and coherence estimates produced. The time varying traces depict microseism activity, explained in sec. 4.

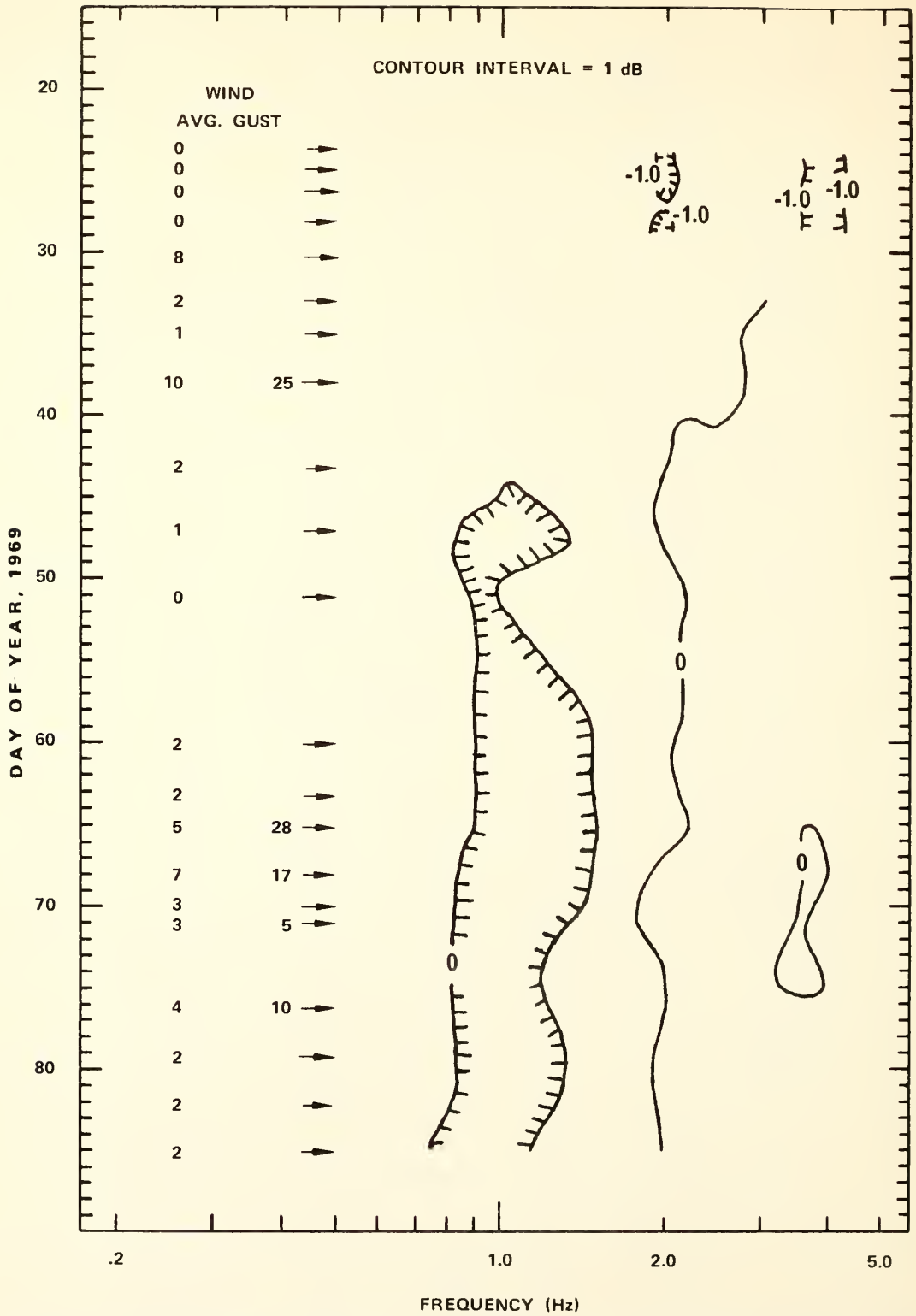

Figure 3.2. The difference between power spectral density estimates made from simultaneous surface and subsurface recordings at position 02B. The differences are for the subsurface. Band displayed is from 0.3 Hz to 5.0 Hz. The discontinuity between days 28 and 30 was probably caused by an adjustment of the EML field amplifier.

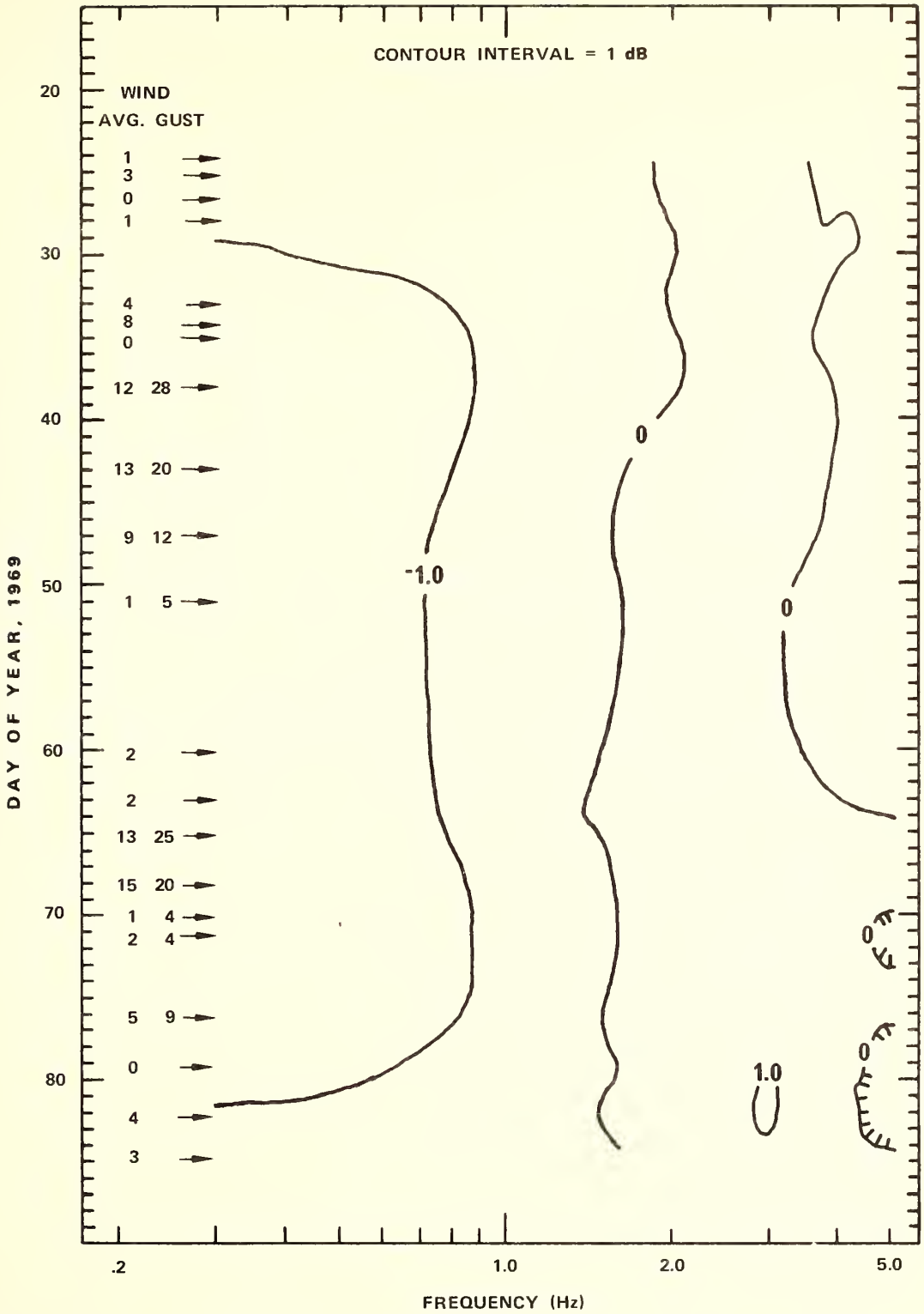

Figure 3.3. The difference between power spectral density estimates made from simultaneous surface and subsurface recordings at position 03B. The difference are for the surface minus the subsurface. Band displayed is from 0.3 Hz to 5.0 Hz.

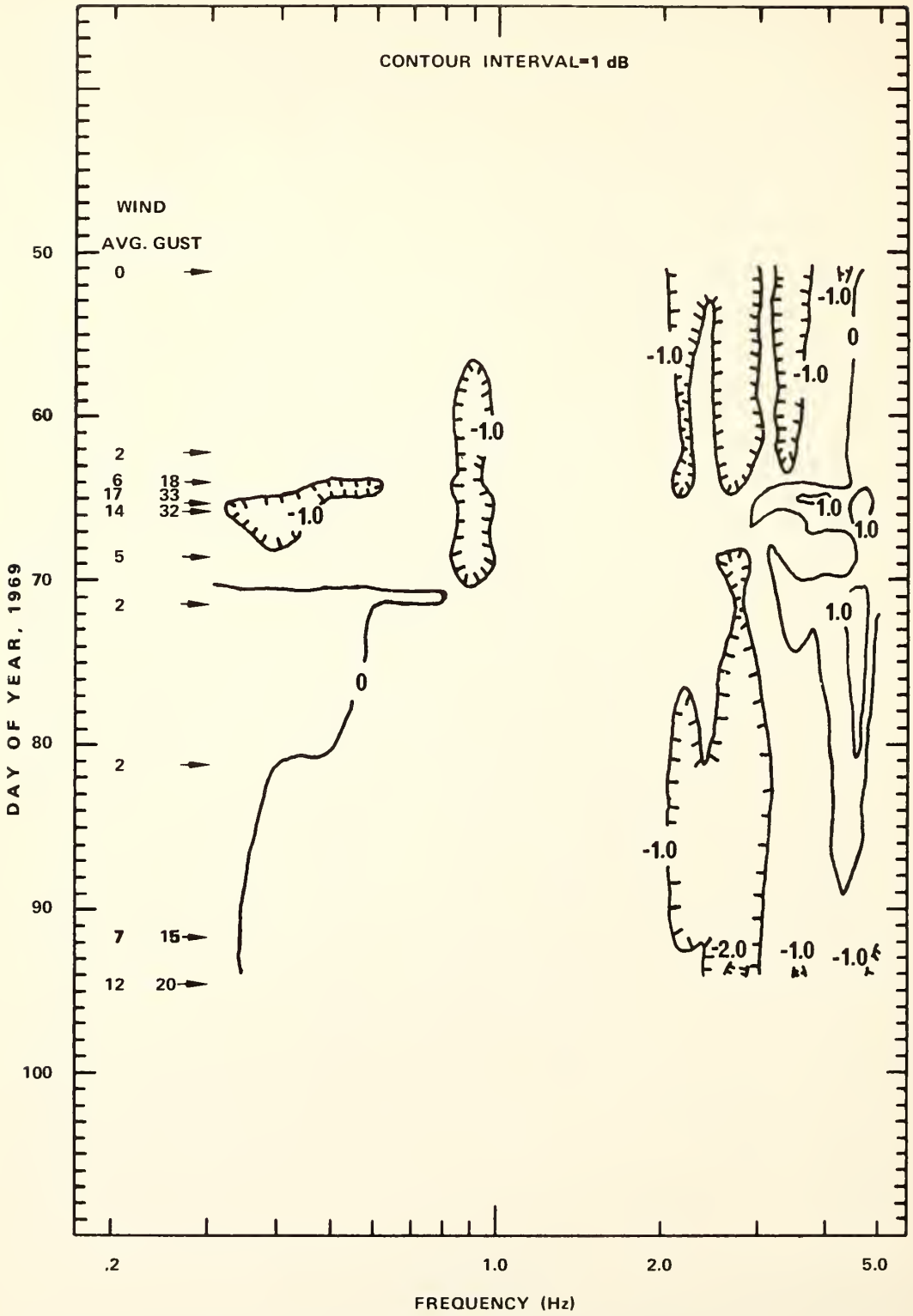

Figure 3.4. The difference between power spectral density estimates made from simultaneous surface and subsurface recordings at position 05B. The differences are for the surface minus the subsurface. Band displayed is from 0.3 Hz to 5.0 Hz.

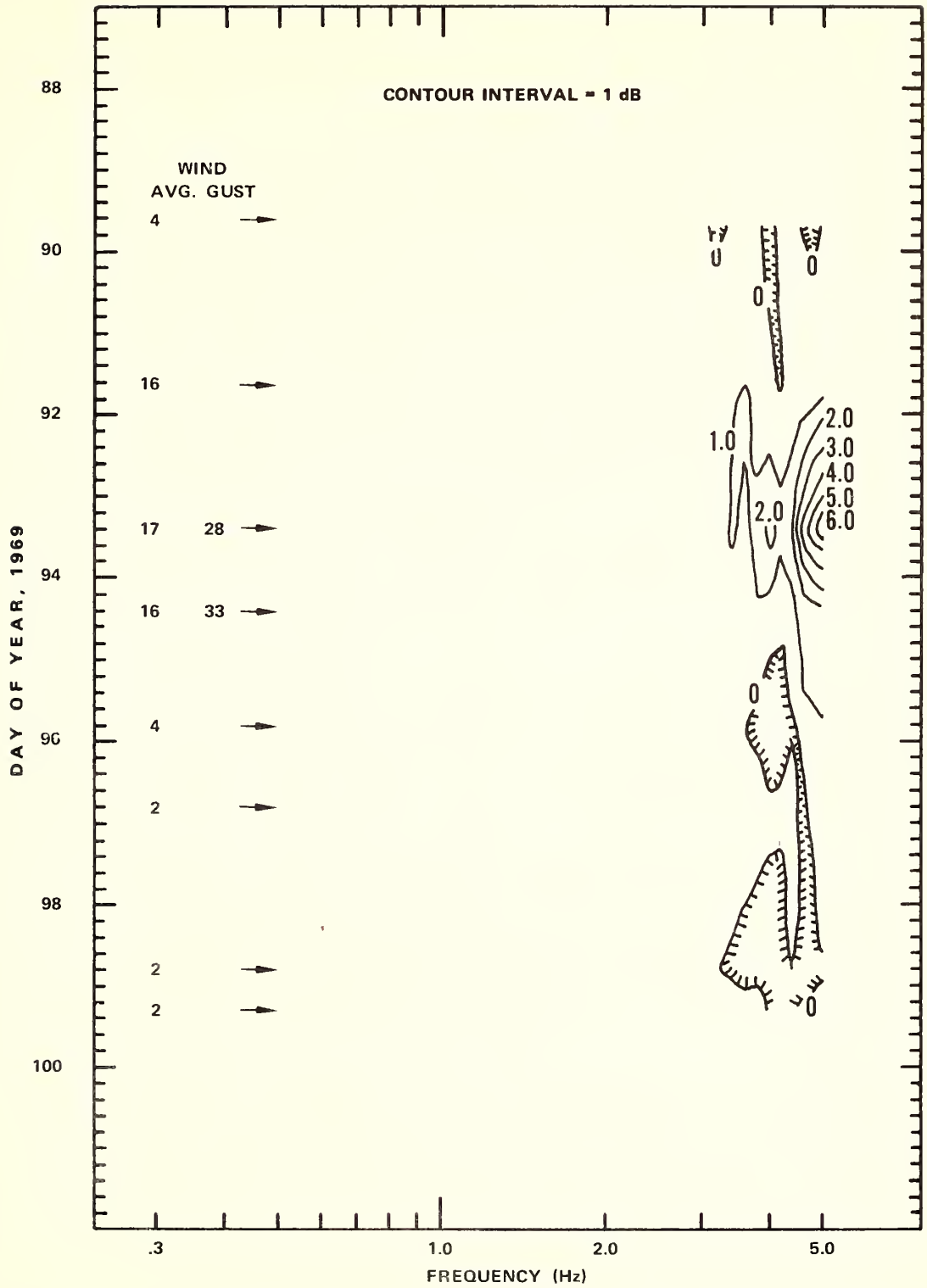

Figure 3.5. The difference between power spectral density estimates made from simultaneous surface and subsurface recordings at position 06B. The difference are for the surface minus the subsurface. Band displayed is from 0.3 Hz to 5.0 Hz.

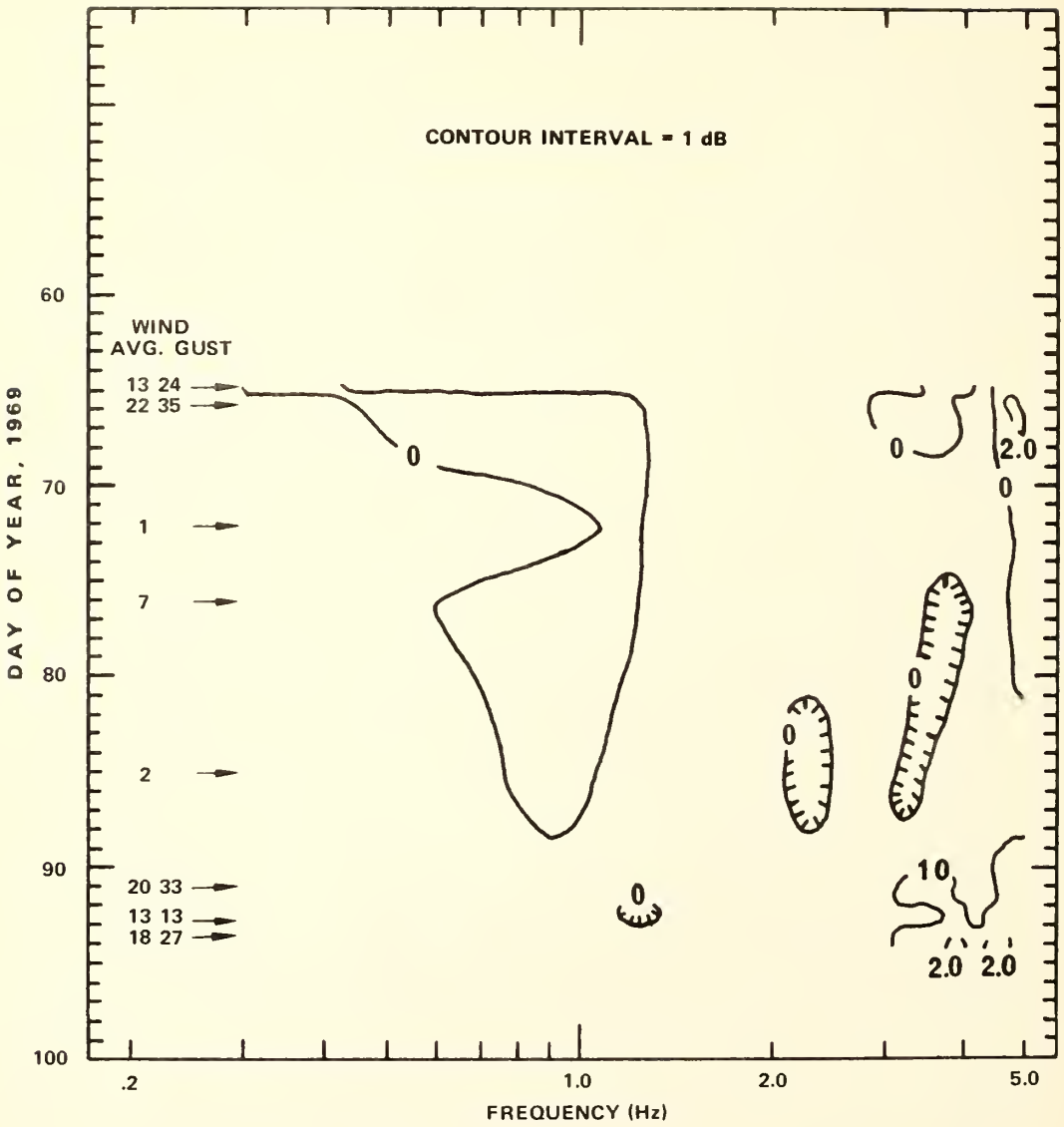

Figure 3.6. The difference between power spectral density estimates made from simultaneous surface and subsurface recordings at position 07B. The differences are for the subsurface. Band displayed is from 0.3 Hz to 5.0 Hz.

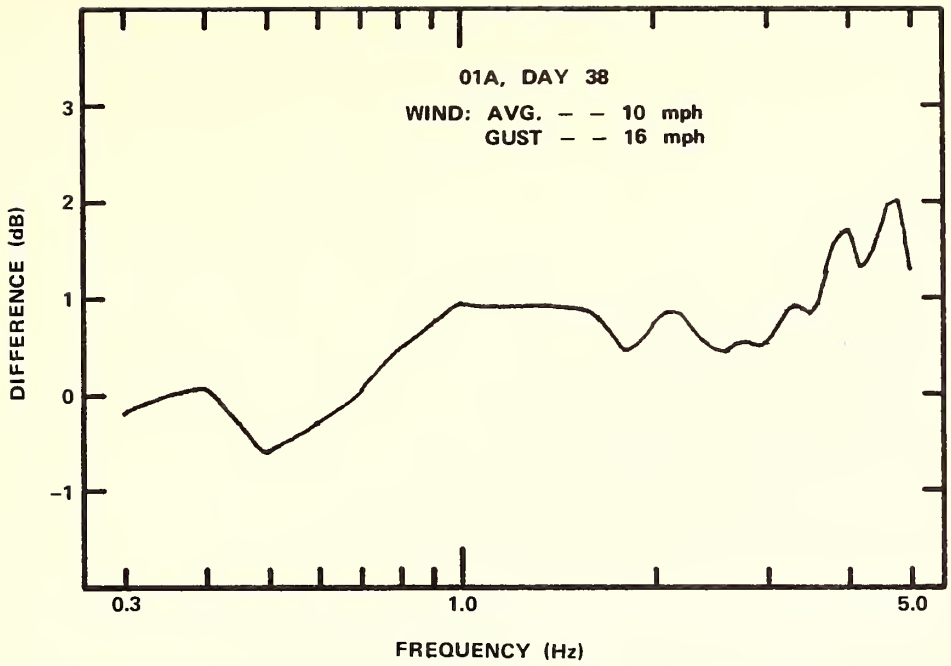

Figure 3.7. The difference between power spectral density estimates made from simultaneous surface and subsurface recordings at position 01A. The differences are for the surface minus the subsurface.

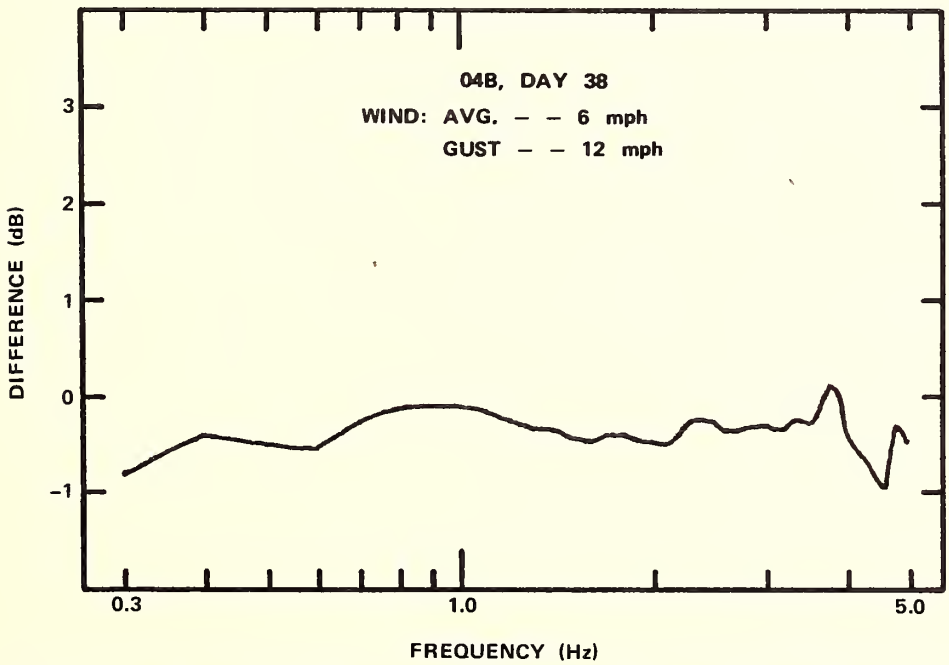

Figure 3.8. The difference between power spectral density estimates made from simultaneous surface and subsurface recordings at position 04B. The differences are for the surface minus the subsurface.

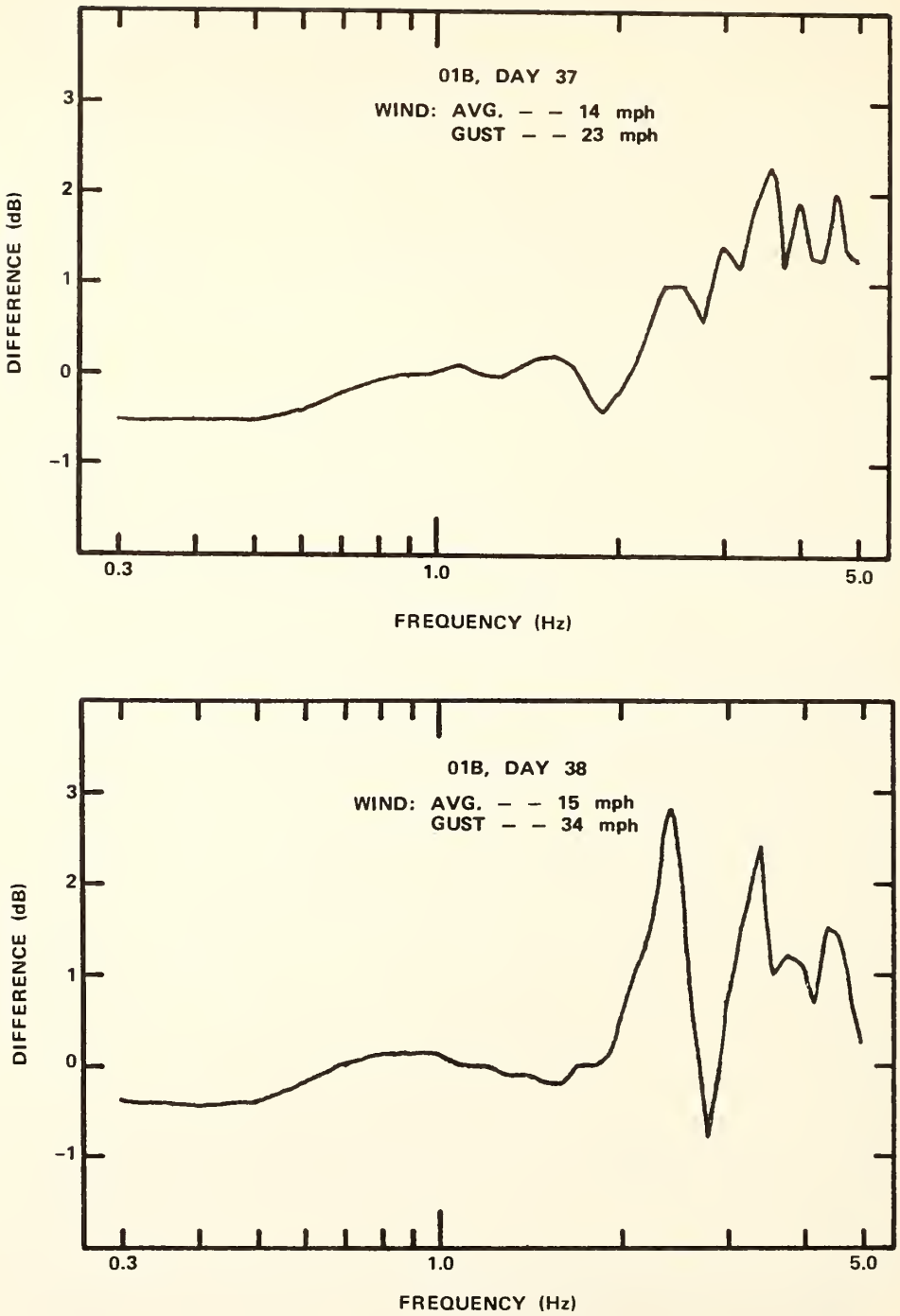

Figure 3.9. The difference between power spectral density estimates made from simultaneous surface and subsurface recordings at position 01B. The differences are for the surface minus the subsurface.

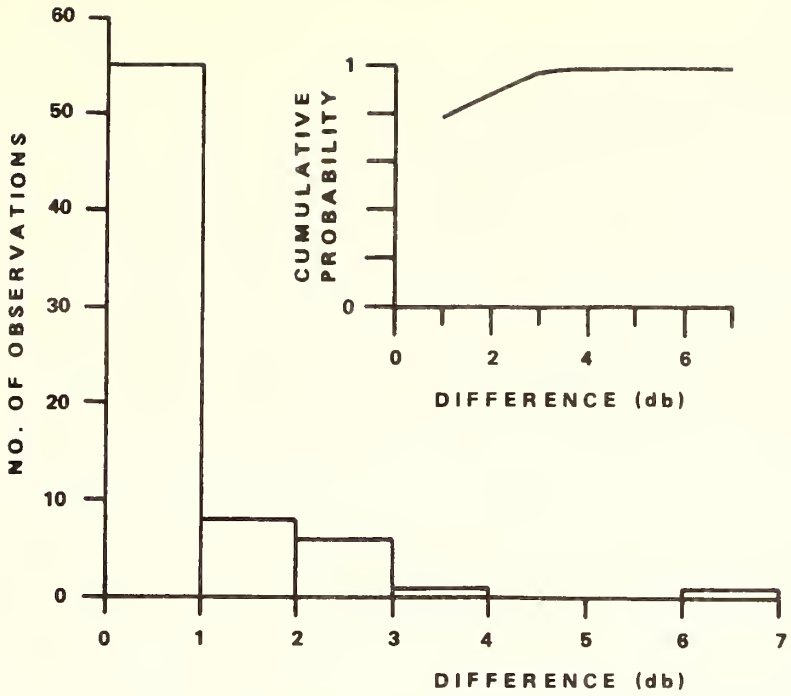

Figure 3.10. Summary of observed differences between the surface and subsurface microseismic fields.

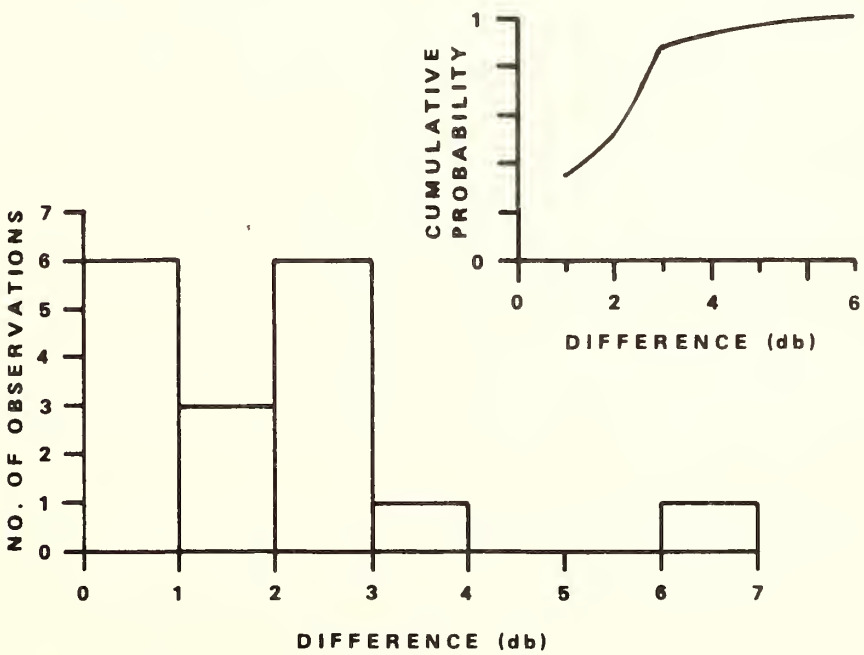

Figure 3.11. Summary of observed differences between the surface and subsurface microseismic fields during times of high winds.

differences of less than 3 dB. In the dominant teleseismic signal band (0.8 to 2.0 Hz), 96 percent of the 71 estimates differ by less than 1 dB, and all differ by less than 3 dB. Examples of seismograms recorded during times of high winds, given in the appendix, also show that the surface and subsurface outputs are almost identical.

3.2 Seismic Signals

Figure 3.12 shows tracings of teleseismic signals recorded by the surface and subsurface sensors of six subarrays. The paired seismograms appear almost identical.

3.3 Other Observations

In addition to the data presented in this section, we and our co-workers at EML have examined more than 1,000 seismograms (having a time base of 3 mm/s, showing microseisms, teleseisms, local quarrying blasts, and cultural noise. From studying simultaneous recordings made by surface and subsurface pairs having equal responses and magnifications, we observed, for each pair the following:

(1) Teleseismic recordings show almost identical wave forms and amplitudes.

(2) Microseismic recordings almost always appear identical, even during times of recorded high wind velocities; at times of recorded high winds, we produced seismograms having a time base of 40 mm/s. Exceptions were found on the 06B seismograms, which sometimes showed the surface approximately 6 dB higher

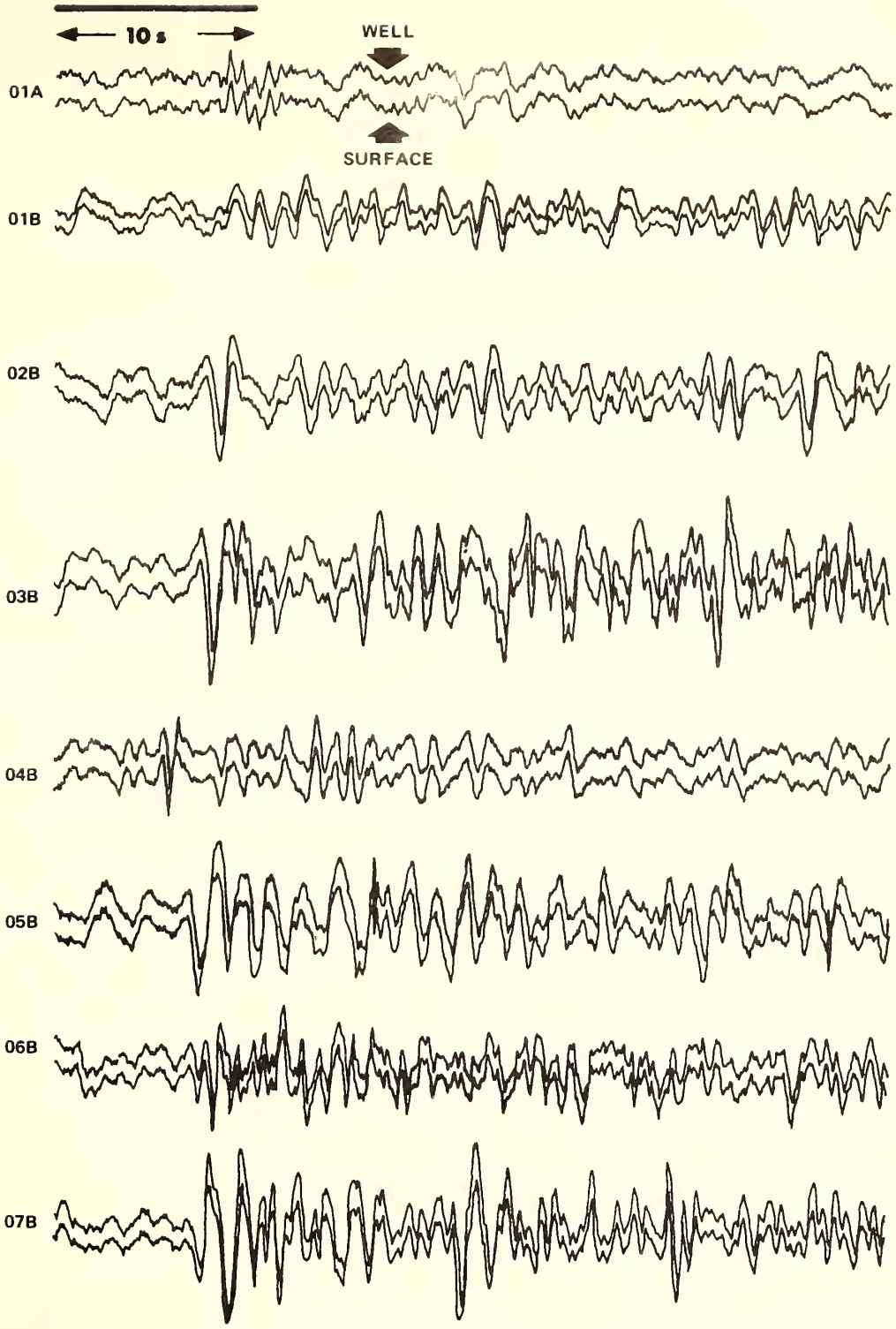

Figure 3.12. Tracings of subsurface- and surface-recorded teleseisms. A seismogram from each subarray is displayed.

than the subsurface in the band near 6 Hz.

(3) Cultural noise (e.g., made by vehicles) generated within several hundred meters of the site sometimes showed amplitudes approximately 6 dB higher on the surface sensors than on the subsurface sensors. Usually, the cultural noise we found, from our audio monitoring procedure, appeared very near the detection threshold. From our data we judge that cultural noise makes a negligible contribution to the overall noise field.

(4) Local quarrying explosions sometimes produce 10 to 15 Hz P signals having amplitudes noticeably higher on the surface seismograms. This is probably an effect of the free surface.

4. PARAMETERS OF THE TIME-VARYING MICROSEISMIC FIELD

4.1 Estimates by Analog Techniques

To reduce the field-recorded data by analog techniques, we:

(1) processed the vertical component microseismic recordings with bandpass filters centered at 0.3 Hz and 1.0 Hz,

(2) made logs of the root-mean square filter outputs at 7-hour intervals (sample length, approximately 10 to 20 min),

(3) applied magnification corrections to the logged meter readings, and

(4) plotted the root-mean square amplitudes versus time.

The meters used for monitoring the filtered outputs were constructed of

a linear law rectifier, designed to detect the absolute average value of a sine wave and convert the absolute average value to the root-mean square value by the meter scale. When a Gaussian signal is applied to the input of this meter type, the values read must be adjusted by a factor of 1.13 (Bendat and Piersol, 1964, p. 2-17). Because the wide-band seismic noise appears to have a Gaussian probability density function (see app.), we assumed Gaussian input to the root-mean square meters for the data used in estimating statistical parameters of the microseism field. For other data, showing relative trends of the time varying microseism field, only magnification corrections were applied (i.e., corrections for Gaussian input were applied to figs. 4.5 through 4.8 only).

Measurements of the root-mean square amplitudes of microseism are presented in figures 4.1 and 4.2, which show the time-varying trends of the 0.3-Hz and 1.0-Hz microseisms. In both illustrations, the trends at the different recording positions are remarkably similar, demonstrating that amplitudes of the monitored microseismic field were approximately space stationary. A comparison between those charts shows that the time-varying trends of the 0.3-Hz and 1.0-Hz microseismic amplitudes are generally similar, although noticeable differences do exist, such as in the 10 to 20 day interval.

4.2 Estimates by Digital Techniques

Spectral density estimates of microseisms recorded in the LPV's at positions 02B and 03B are plotted as a function of time and frequency in

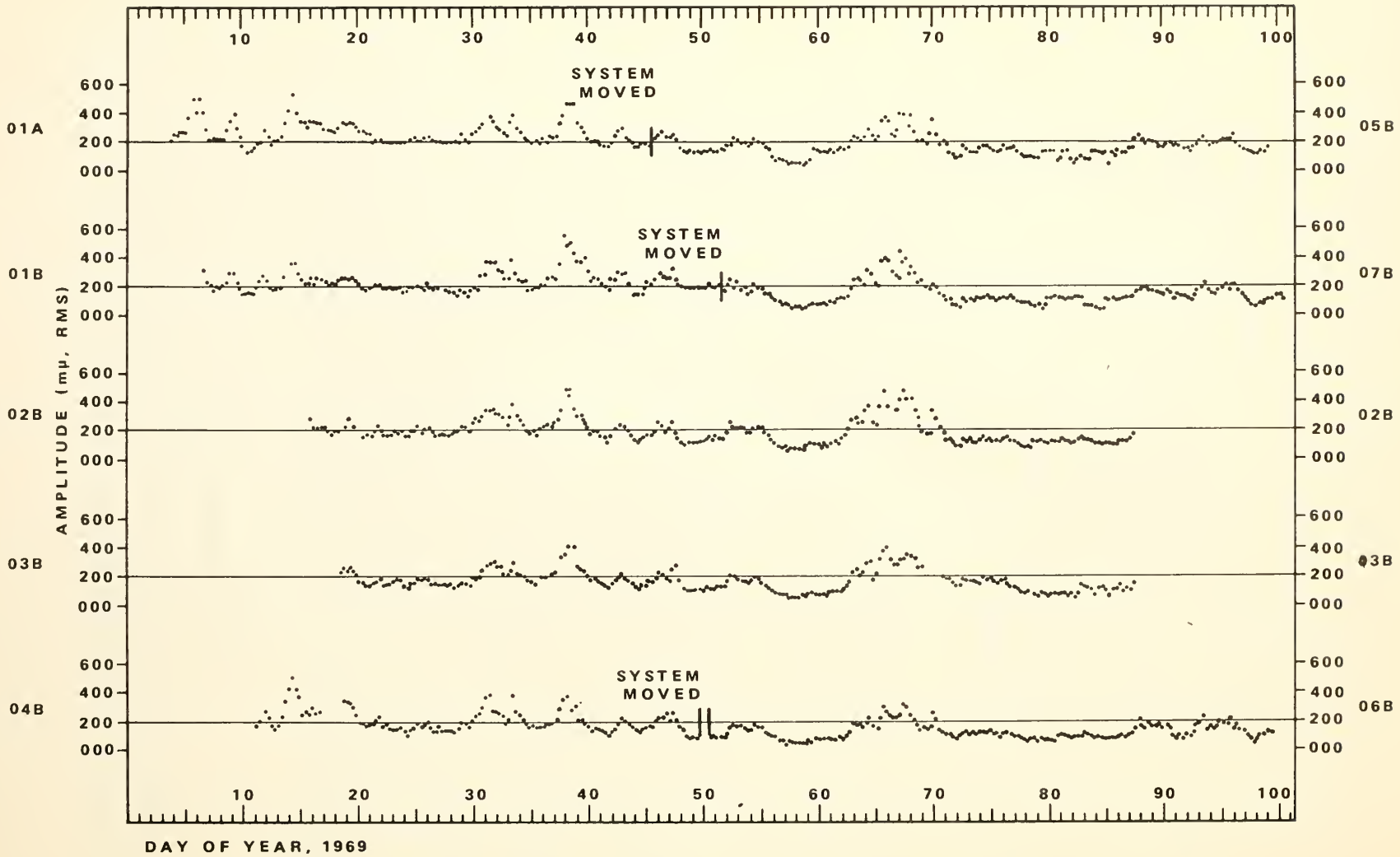

Figure 4.1. Time-varying trends of microseisms in the band near 0.3 Hz (see sec. 4.1).

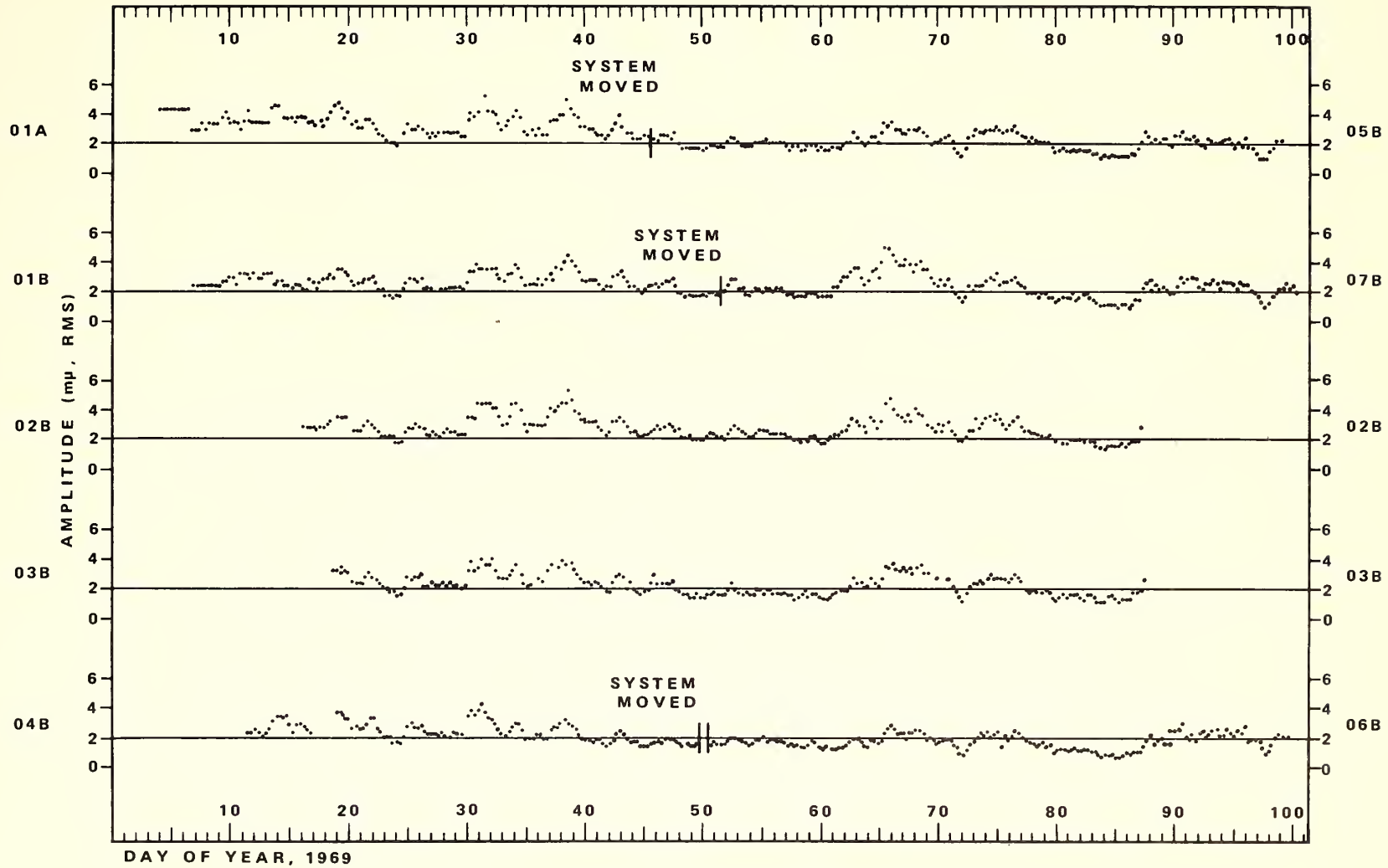

Figure 4.2. Time-varying trends of microseisms in the band near 1.0 Hz (see sec. 4.1).

figures 4.3 and 4.4. Comparison shows that the two charts are quite similar in the 0.2- to 2-Hz band, again demonstrating the space-stationary aspects of the microseismic field. A similarity of time-varying trends at 0.3 Hz and 1.0 Hz is again evident, as for the analog analyses (figs. 4.1 and 4.2). In the 2- to 5-Hz band, the microseismic power displayed are probably affected by system noise (see fig. 2.4). We also suspect that the estimates at 0.6 Hz are biased by as much as 3 dB because of system noise (see sec. 2.2).

4.3 Statistical Properties of the Data

Graphs of probability density and probability distribution, depicting amplitude and power of the 0.3-Hz and 1.0-Hz microseisms recorded at position 02B, are displayed in figures 4.5 through 4.8. These graphs were prepared from analog data given in figures 4.1 and 4.2 by:

(1) adjusting the values by a factor of 1.13 to compensate for Gaussian input to the root-mean square meters (sec. 4.1), and

(2) normalizing the adjusted values to a 1.0 Hz bandwidth; adjusted values were divided by the filter bandwidth; the bandwidth is the center frequency setting of the filter multiplied by 0.53.

The 50 percent probability values of the data are: 1.3×10^3 mμ/Hz or 2.4×10^5 $(m\mu)^2$/Hz at 0.3 Hz; and 5.6×10^0 mμ/Hz or 1.6×10^1 $(m\mu)^2$/Hz at 1.0 Hz. Medians of corresponding values given in figure 4.3 (digital estimates) agree with the analog estimates to within 2 dB. Average values of amplitude and power are approximately those of the medians.

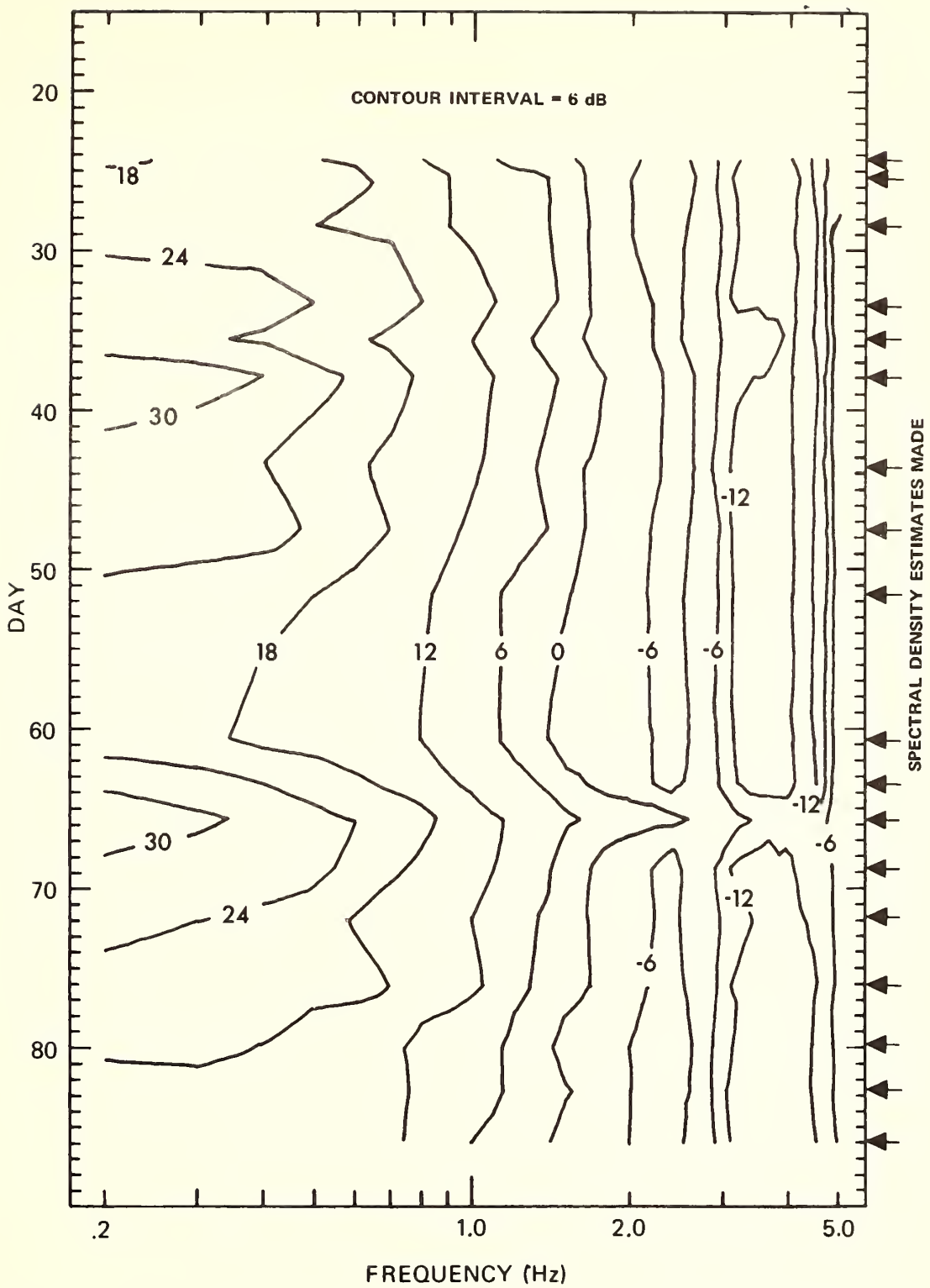

Figure 4.3. Power spectral density estimates depicting time-varying trends at position 02B. The 0 dB contour is 1 (mμ)2/Hz at 1.0 Hz (see app. for system response).

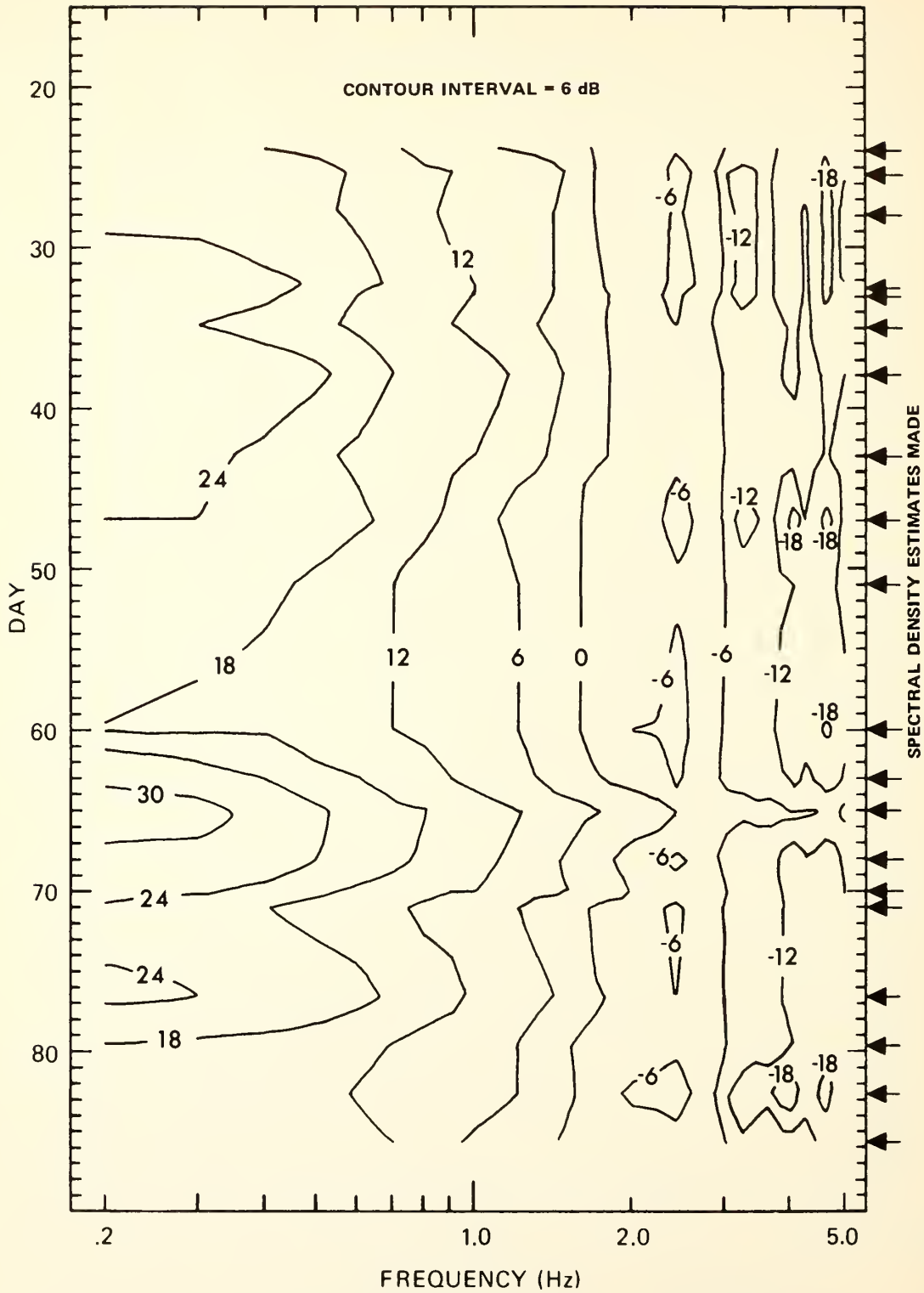

Figure 4.4. Power spectral density estimates depicting time-varying trends at position 03B. The 0 dB contour is 1 (mμ)2/Hz at 1 Hz (see app. for system response).

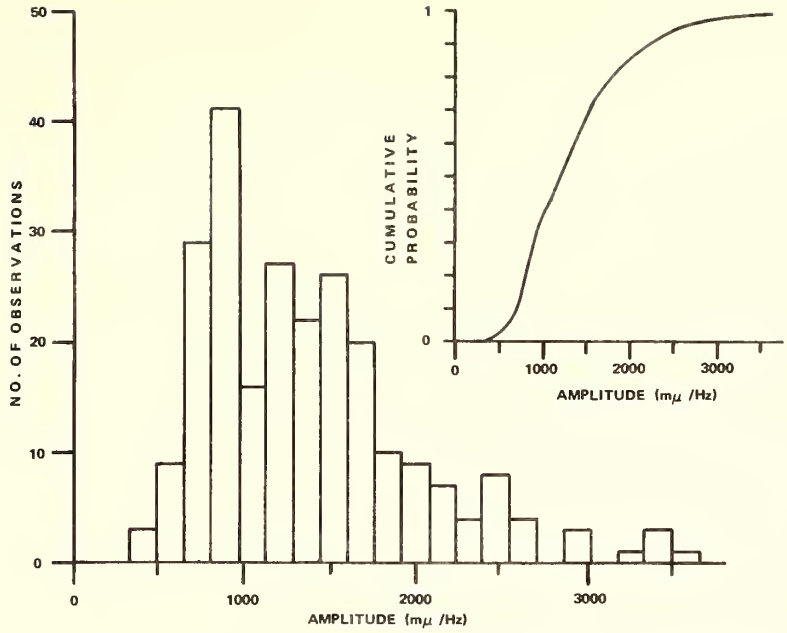

Figure 4.5. Density and distribution of microseism amplitudes in the band near 0.3 Hz.

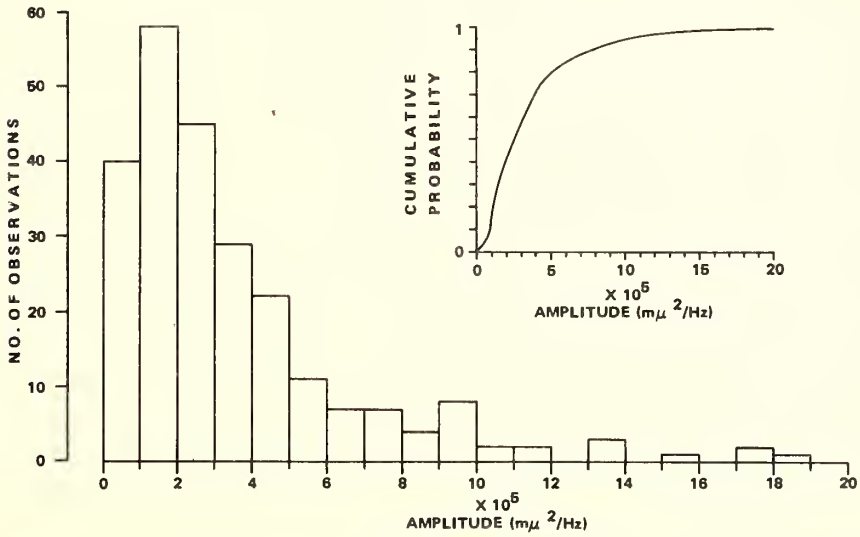

Figure 4.6. Density and distribution of microseism power in the band near 0.3 Hz.

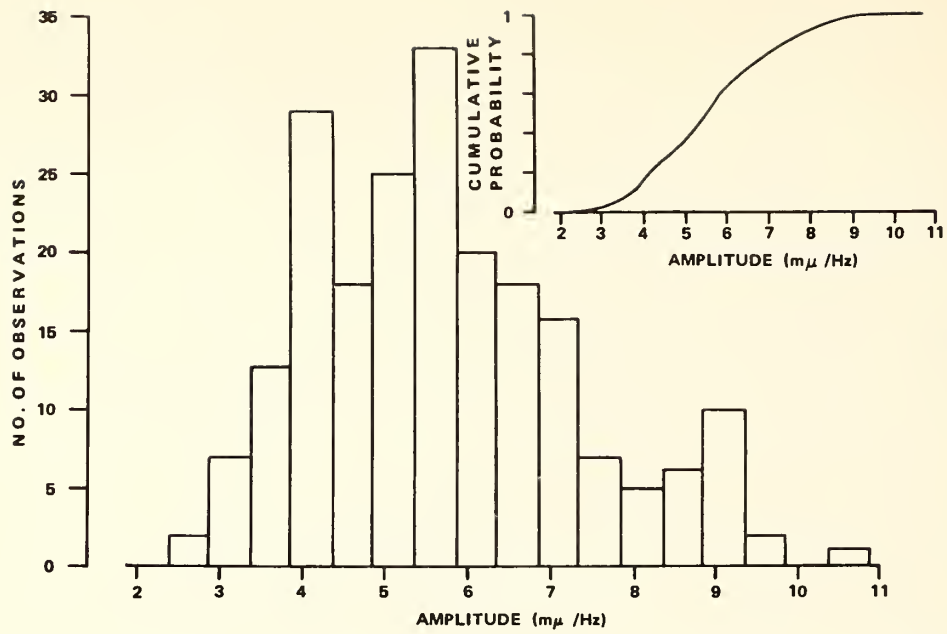

Figure 4.7. Density and distribution of microseism amplitudes in the band near 1.0 Hz.

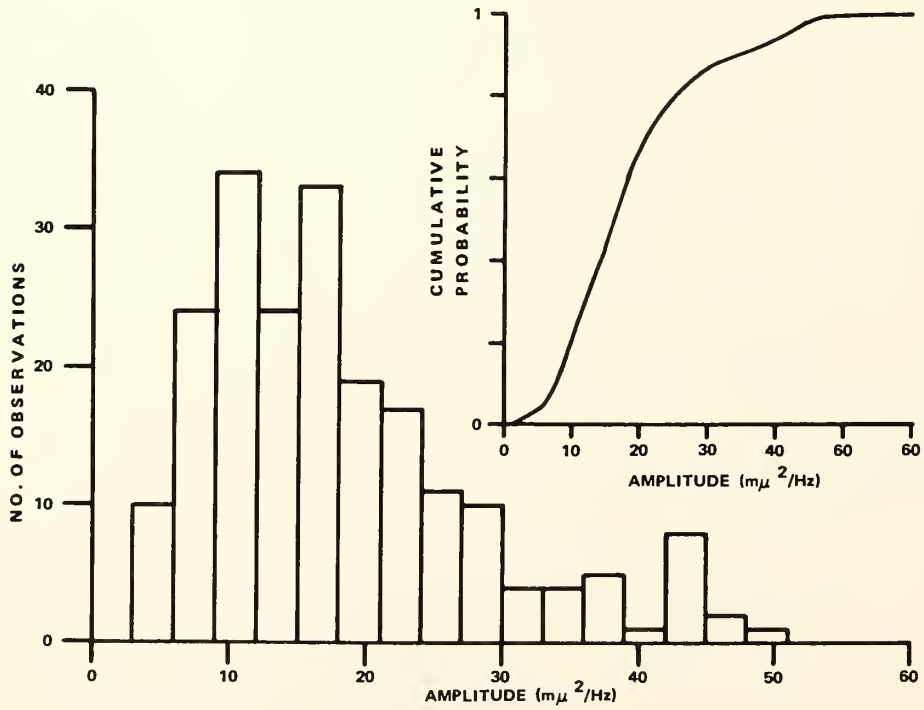

Figure 4.8. Density and distribution of microseism power in the band near 1.0 Hz.

5. COHERENCE OF MICROSEISMS

5.1 Data Reduction and Construction of Displays

Digital data reduction techniques for coherence estimates are outlined in the appendix. By coherence, we mean an estimate of the positive square root of the function

$$\kappa_{12}^2(f) = \frac{|\Gamma_{12}(f)|^2}{\Gamma_{11}(f)\cdot\Gamma_{22}(f)} \qquad (5.1)$$

defined by Jenkins and Watts (1969 p. 356). The symbols used in this section are defined as follows:

$H(f)$	transfer function
$h(t)$	impulse response function
t_i	time shift
u	lag
V	wave propagation velocity
$X(f)$	output spectrum
$X(t)$	output time series
x	seismometer separation
$Z(f)$	input spectrum
$Z(t)$	input time series
$\Gamma(f)$	power spectrum, theoretical
$\gamma(u)$	covariance function, theoretical
$\theta(f)$	phase spectrum, theoretical
$\kappa^2(f)$	squared coherence spectrum, theoretical
σ^2	variance

Hereafter, we will call the function $\kappa_{12}^2(f)$ squared coherence.

To depict the coherence of the vertical component of microseisms recorded at adjacent sensors of a subarray, we use two different types of displays:

(1) Coherence is plotted as a function of frequency and of distance between pairs of sensors recording seismic data. The plotted values are contoured to depict approximate coherence trends.

(2) Coherence is displayed as a function of distance and azimuth. An example is shown in figure 5.1. The polygon is a spatial plot of a specific value of coherence for a specific frequency (e.g., 0.7 for 0.3 Hz). The length of a line represents the distance between two sensors; the azimuth, their relative direction. The computed coherence between a sensor pair is assigned to the end of a line, unity coherence is assigned to the origin, and the specific value (e.g., 0.7) is determined by linear interpolation. This procedure is repeated for the other sensor pairs, radial symmetry is assumed, and the interpolated values are contoured. This method of displaying the data was originated by Rygg, Bungum, and Bruland of the University of Bergen.

5.2 Observed Sample Coherence

Figures 5.2 to 5.9 show the sample coherence for sets of data taken at adjacent subarray sensors of the A and B ring of subarrays; the polygons shown on the figures describe coherence of 0.7 at 0.3 Hz. Each illustration shows the apparent propagation direction for the 0.3-Hz microseisms, determined from time parameters of the cross spectra. The following are some features shown by the illustrations:

(1) For the band 0.8 to 2.0 Hz, the coherence approaches values we estimate for unrelated samples (see fig. 5.10).

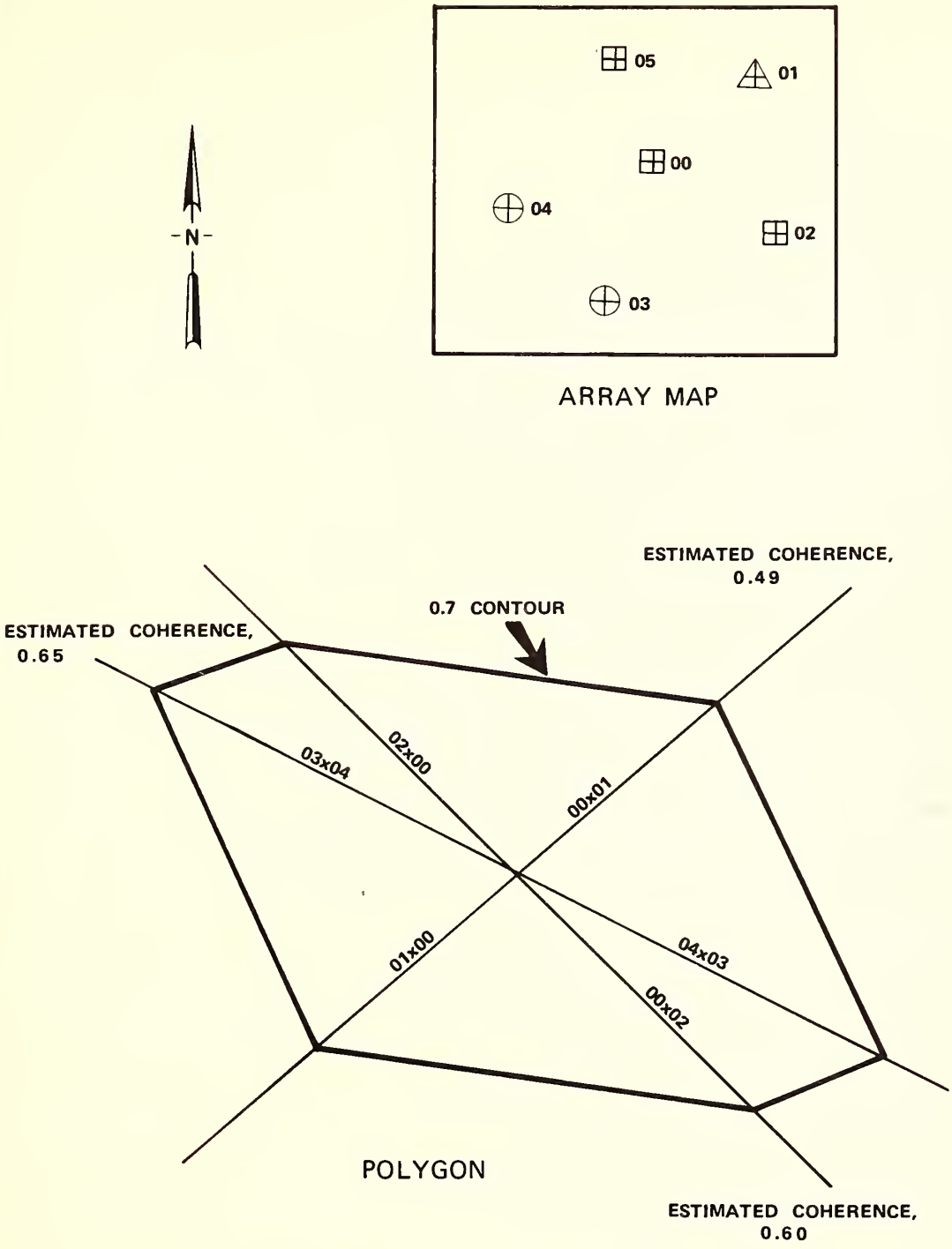

Figure 5.1. Construction of coherence polygons.

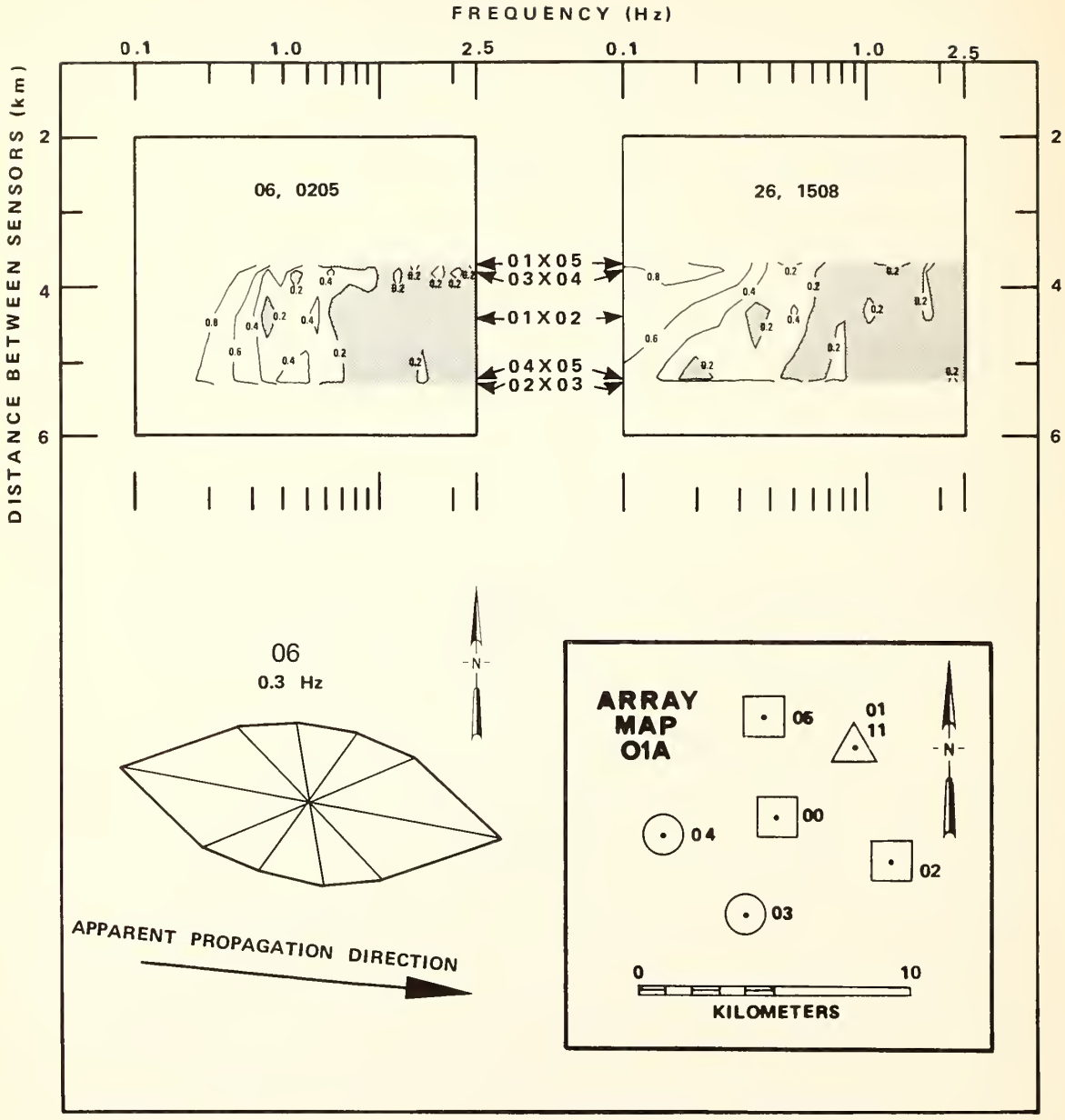

Figure 5.2. Coherence charts and coherence polygon for subarray 01A. Areas of the charts having values less than 0.2 are shaded.

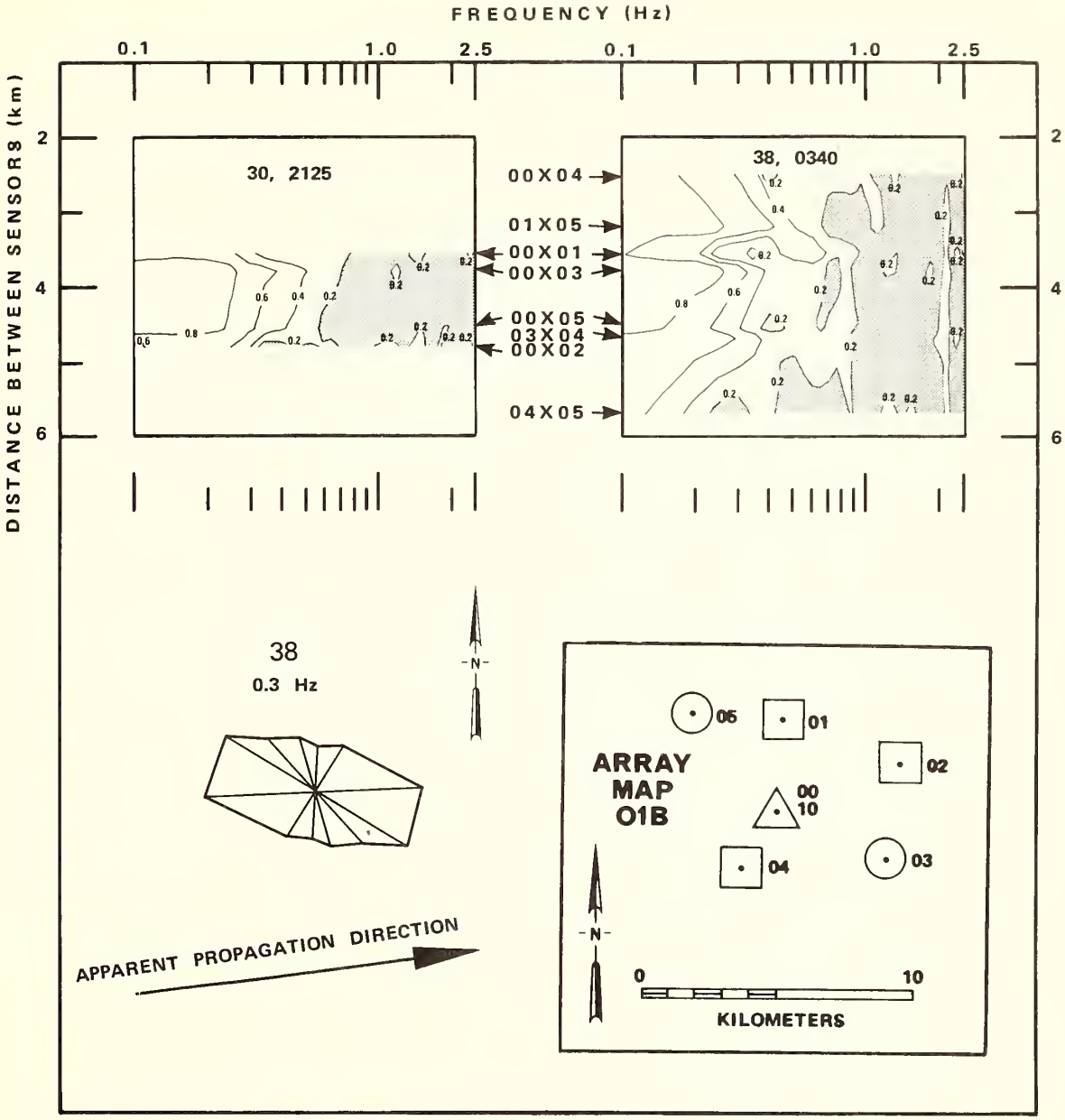

Figure 5.3. Coherence charts and coherence polygon for subarray 01B.

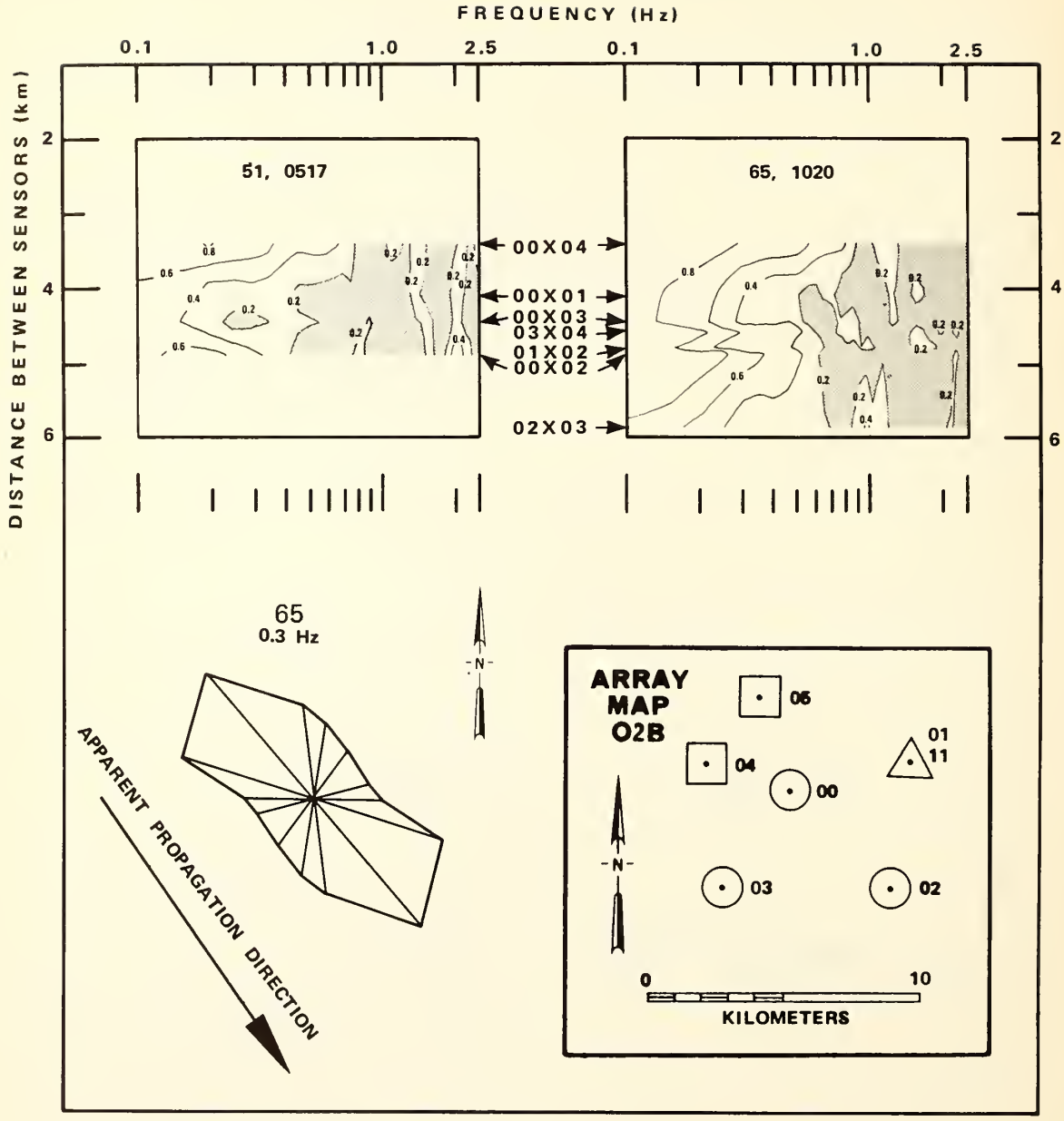

Figure 5.4. Coherence charts and coherence polygon for sub-array 02B.

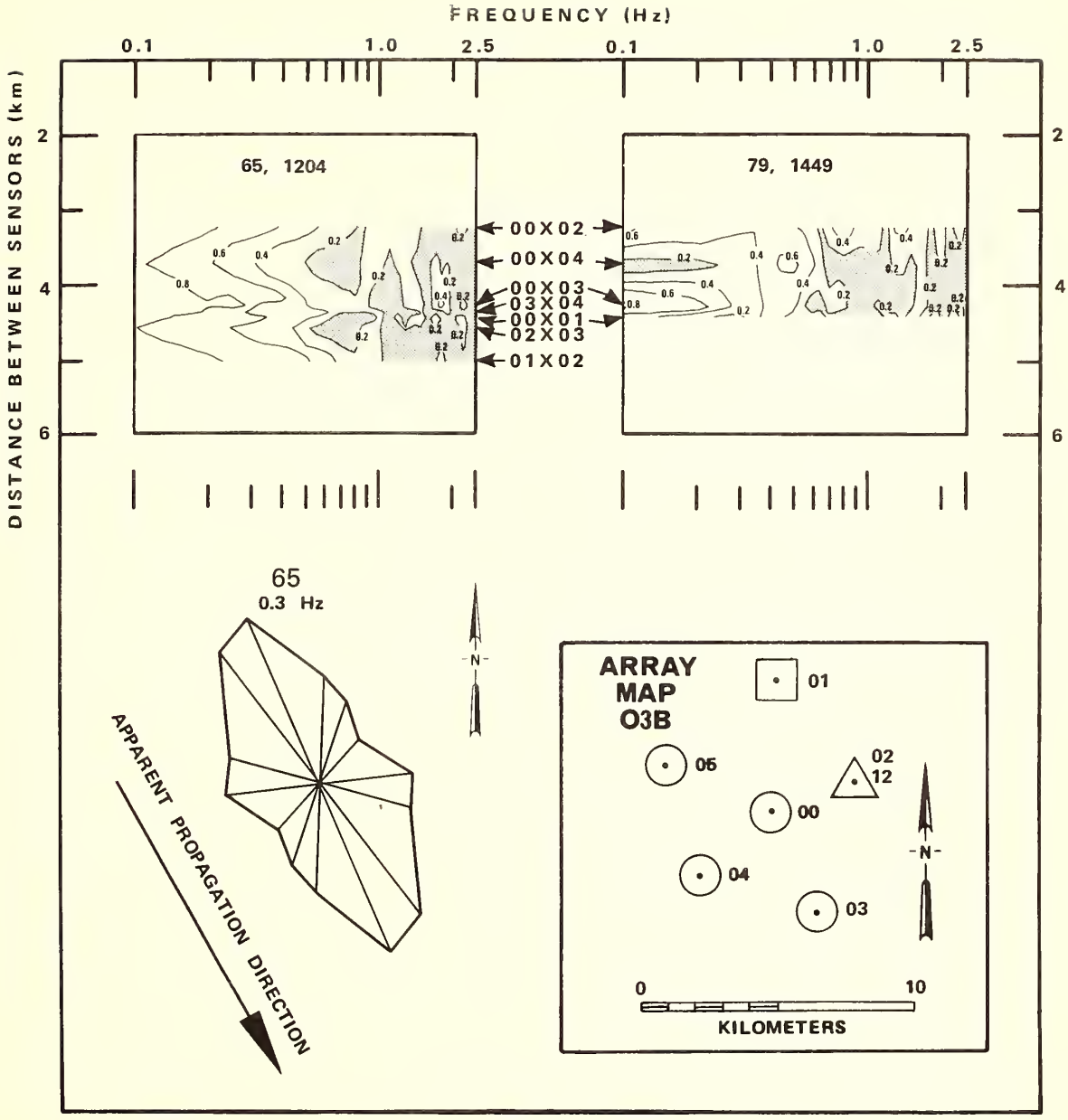

Figure 5.5. Coherence charts and coherence polygon for sub-array 03B.

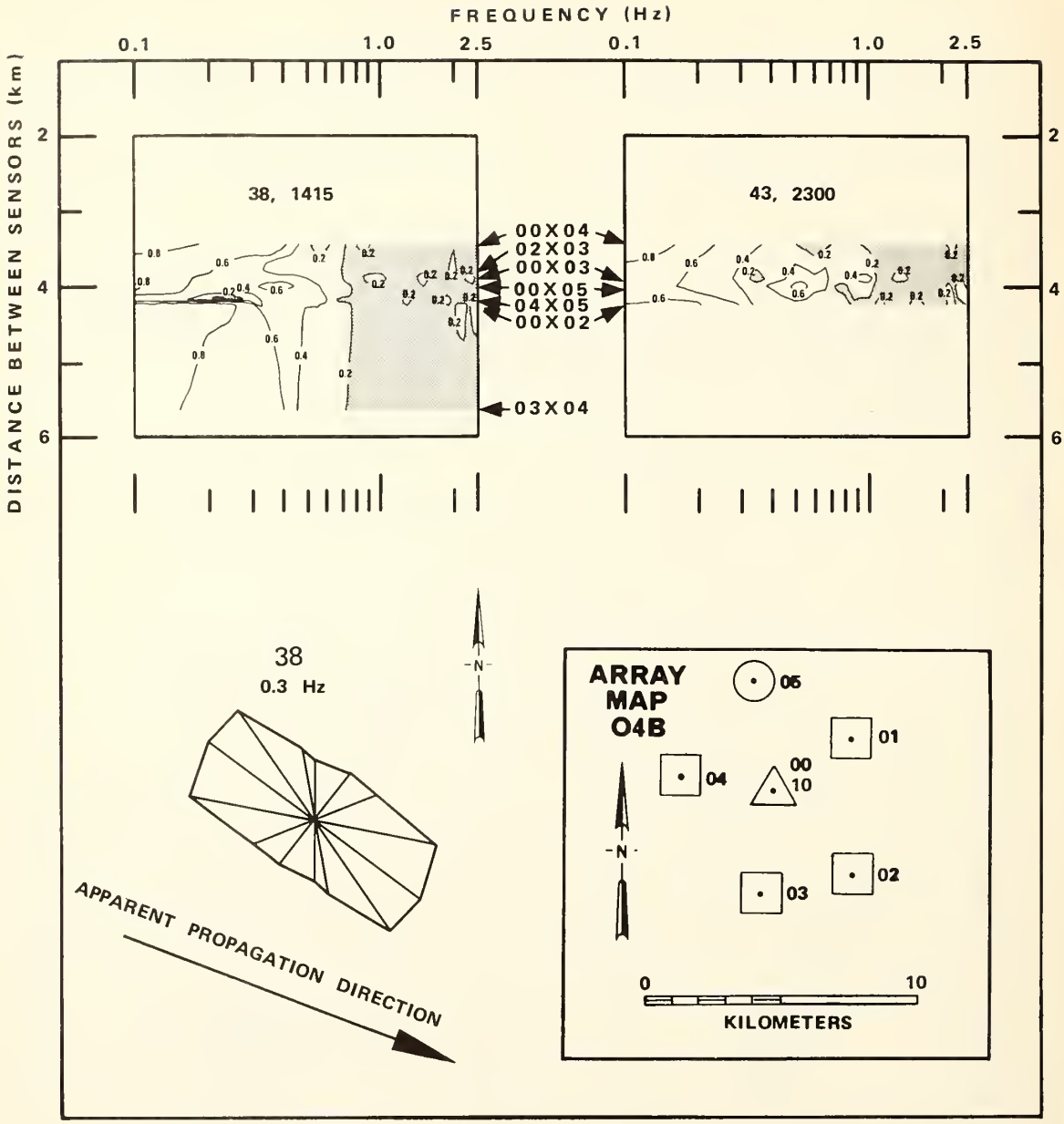

Figure 5.6. Coherence charts and coherence polygon for sub-array 04B.

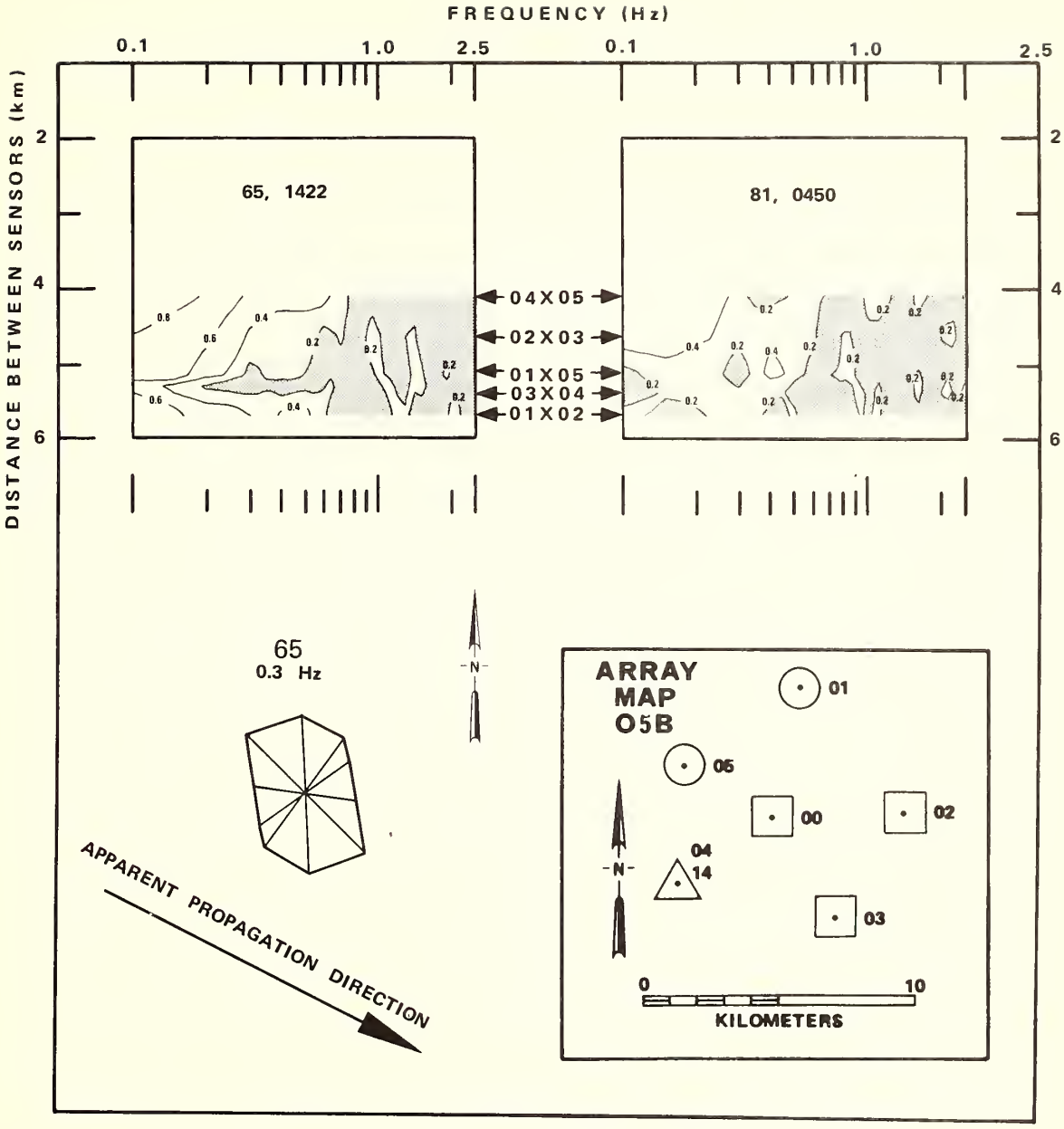

Figure 5.7. Coherence charts and coherence polygon for subarray 05B.

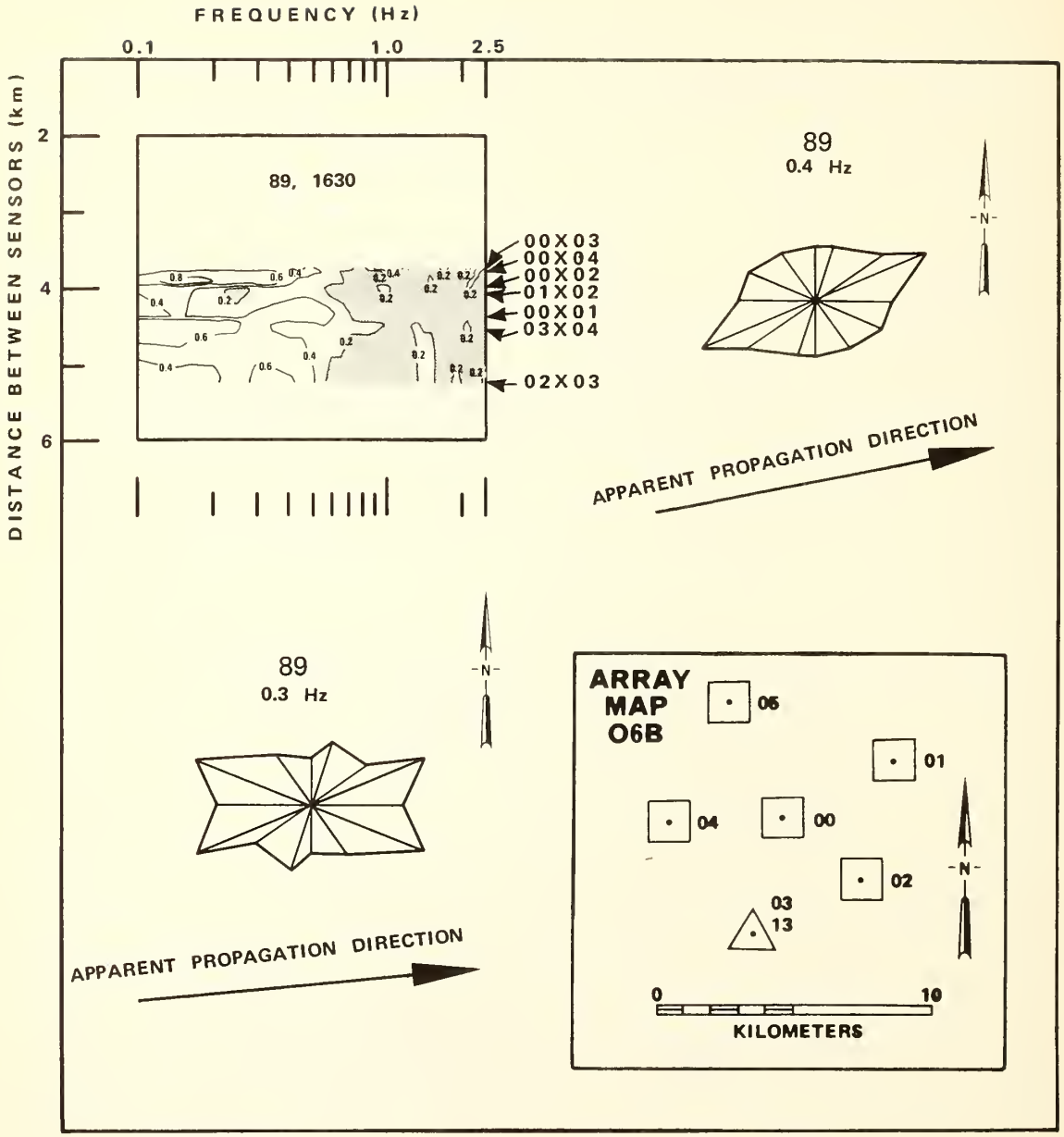

Figure 5.8. Coherence chart and coherence polygons for subarray 06B. Shown are polygons for 0.3 Hz and 0.4 Hz; both show the 0.7 coherence contour.

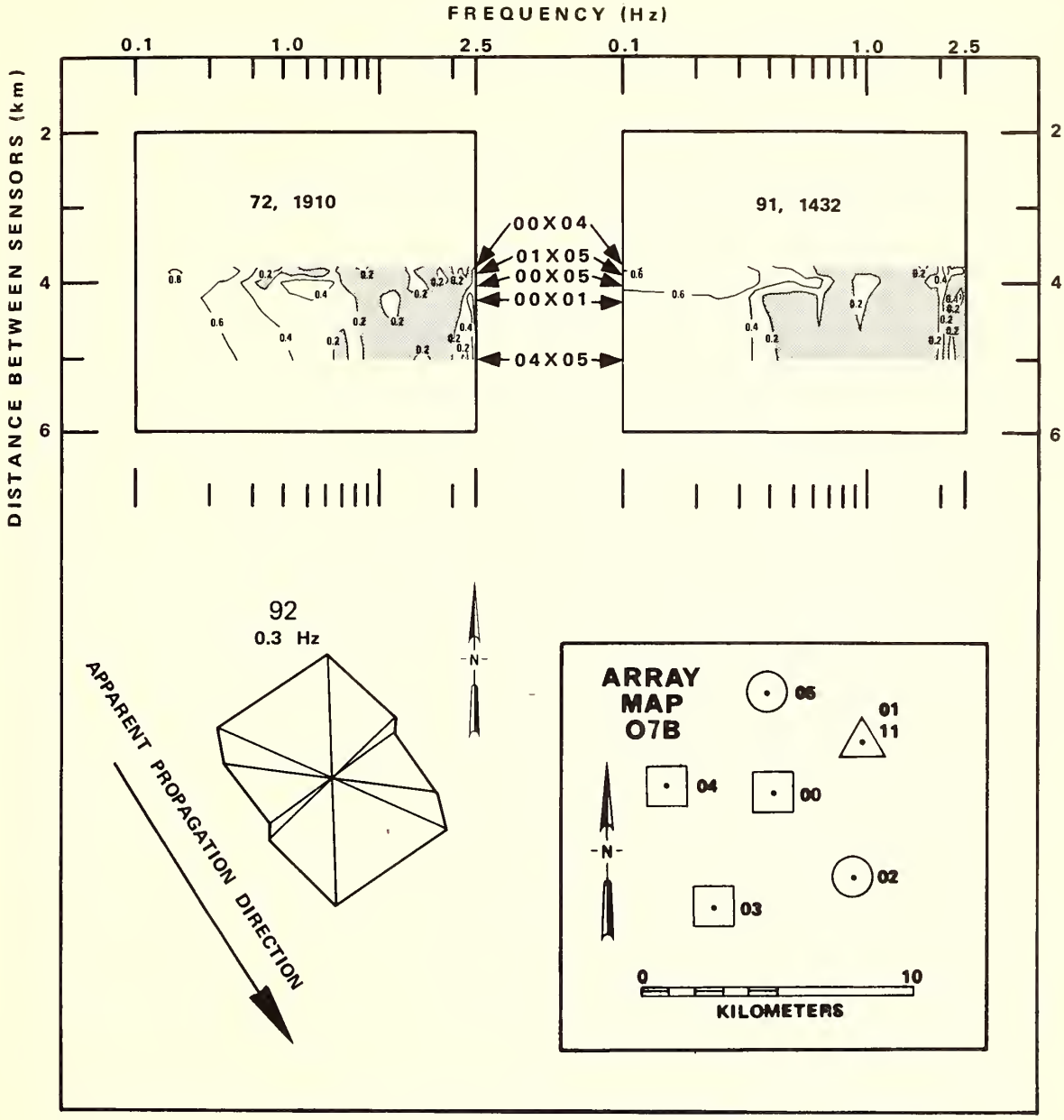

Figure 5.9. Coherence charts and coherence polygon for subarray 07B.

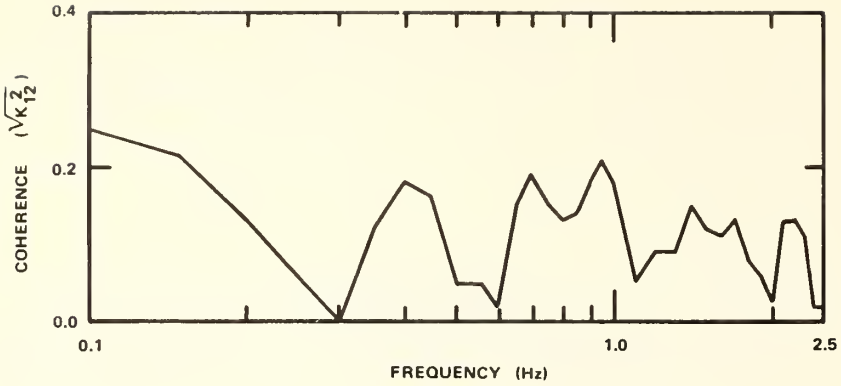

Figure 5.10. Coherence estimated from two unrelated samples.

(2) Normally, the coherence displays a strong azimuthal dependence, especially at lower frequencies. This dependence is particularly well exemplified by the elongate shapes of the polygons, which indicate that, at the lower frequencies, the highest coherence normally is in the direction of apparent microseism propagation--as observed previously by Bungum et al. (1969).

(3) The coherence trends, shown by the contours on the frequency versus distance charts, are time variant, i.e., at a given subarray, the charts constructed for different times are somewhat dissimilar (in particular, see fig. 5.5).

(4) The distance-frequency plots of coherence often display distinct secondary maxima and minima. Figure 5.11 shows coherence, plotted as a function of frequency only, of selected

sample pairs used in constructing figure 5.2. From a comparison of figure 5.11 with 5.10 we see that the secondary maxima are well above the level of randomness. Secondary maxima also appear in coherence estimates made by Rygg, Bungum, and Bruland (1969).

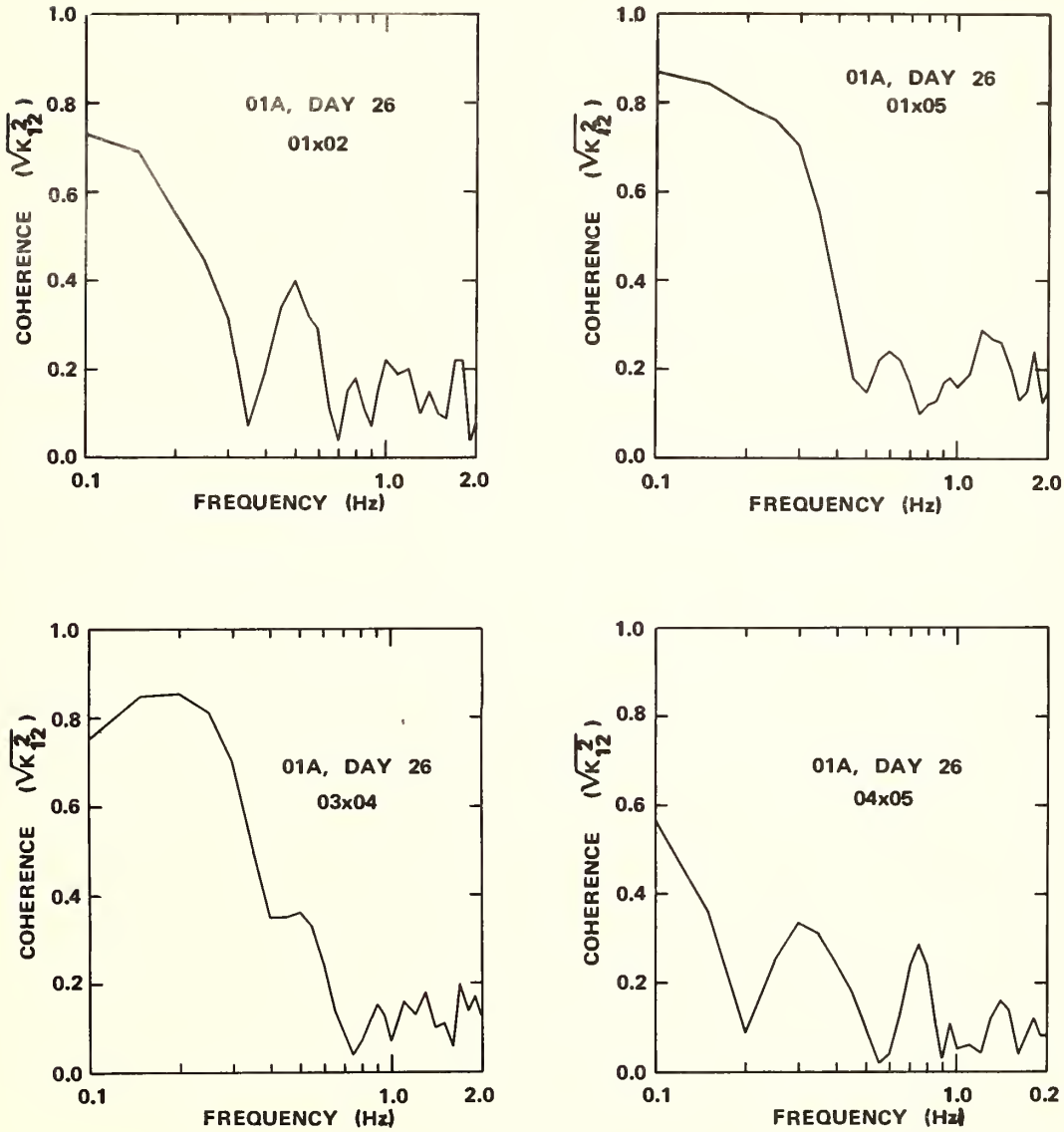

Figure 5.11. Estimated coherence between sensors of subarray 01A. The sensor pairs are indicated on each graph. Map of 01A is shown in figure 5.2.

Our studies suggest to us that an interference process produces the azimuthal dependence and secondary maxima observed. The following section presents a model giving a physical interpretation of these observations.

5.3 Model of the Coherence Variations

An interference pattern of two uncorrelated seismic wave trains crossing a pair of sensors is depicted in figure 5.12. Respective wave fronts of the two trains reach sensor 2 t_1 and t_2 seconds after having crossed sensor 1. The sensors are separated by distance x, and the waves propagate at a constant velocity. The wave trains are assumed to propagate undispersed and unattenuated between the sensors and ground displacements along wave fronts remain constant with respect to lateral distance from the ray trace. Following the reasoning of Jenkins and Watts (1968 p.329), one can think of wave trains as passing through a network of linear systems as shown in figure 5.13; two propagating wave trains enter the network on the left, are combined as indicated, and emerge as the signals $X_1(t)$ and $X_2(t)$ detected by two sensors. The outputs are then expressed as:

$$X_1(t) = \int_0^\infty h_{11}(u)\cdot Z_1(t-u)du + \int_0^\infty h_{12}(u)\cdot Z_2(t-u)du, \qquad (5.2)$$

and

$$X_2(t) = \int_0^\infty h_{21}(u)\cdot Z_1(t-u)du + \int_0^\infty h_{22}(u)\cdot Z_2(t-u)du. \qquad (5.2)$$

For the model, the impulse response functions h(u) are the dirac delta functions shown in the network diagram. The above equations then become

$$X_1(t) = Z_1(t) + Z_2(t), \qquad (5.3)$$

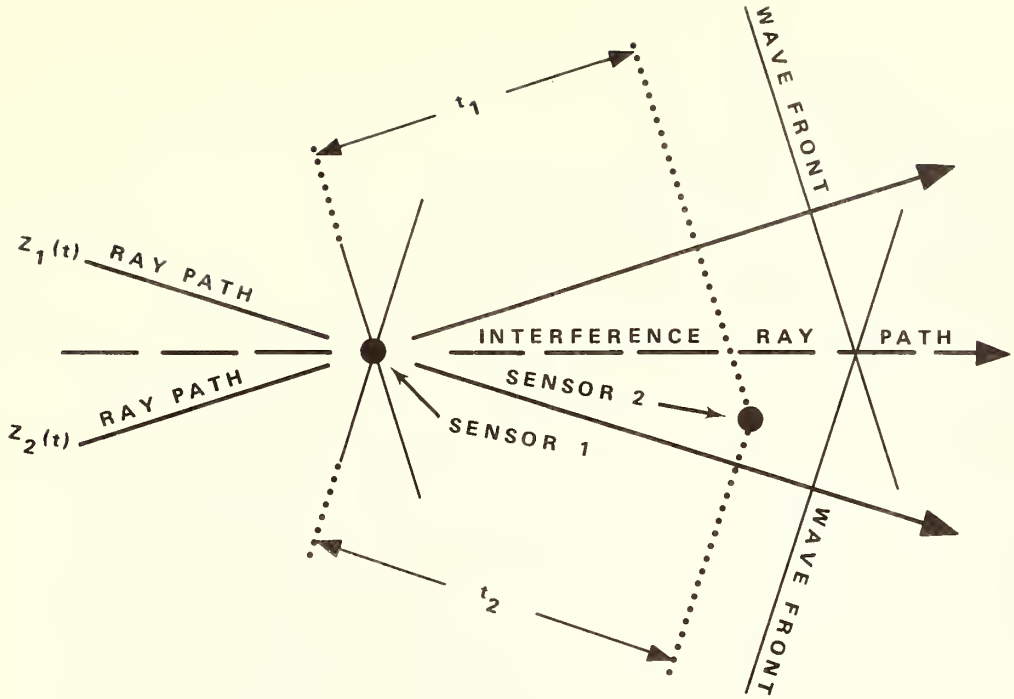

Figure 5.12. An interference process produced by two sources.

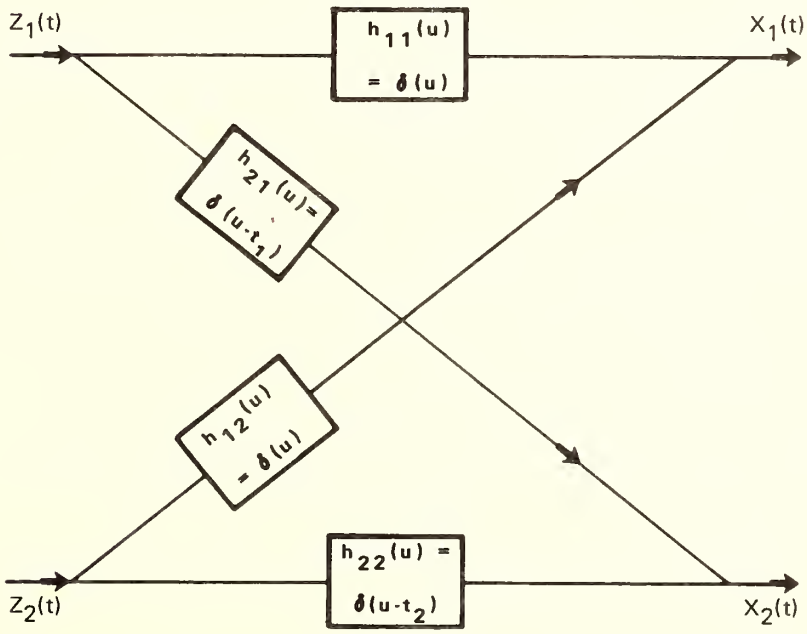

Figure 5.13. Representation of two interfering wave trains passing through a network of linear systems.

and

$$X_2(t) = Z_1(t-t_1) + Z_2(t-t_2). \tag{5.3}$$

By taking the Fourrier transforms of the above, we obtain

$$X_1(f) = Z_1(f) + Z_2(f), \tag{5.4}$$

and

$$X_2(f) = Z_1(f)\cdot e^{-j2\pi f t_1} + Z_2(f)\cdot e^{-j2\pi f t_2}, \tag{5.4}$$

and hence the transfer functions corresponding to the network elements shown in figure 5.13 are

$$H_{11}(f) = 1 \qquad H_{12}(f) = 1, \tag{5.5}$$

and

$$H_{21}(f) = e^{-j2\pi f t_1} \qquad H_{22}(f) = e^{-j2\pi f t_2}. \tag{5.5}$$

This model can easily be expanded to any number of uncorrelated input wave trains $Z_i(t)$ passing through network elements

$$h_{1i}(u) = \delta(u), \tag{5.6}$$

and

$$h_{2i}(u) = \delta(u-t_i), \tag{5.6}$$

and then combining together at the two sensors. Then the two output traces may be expressed as

$$X_1(t) = \sum \int_0^\infty h_{1i}(u)\cdot Z_i(t-u)du, \tag{5.7}$$

and

$$X_2(t) = \sum \int_0^\infty h_{2i}(u)\cdot Z_i(t-u)du. \tag{5.7}$$

where the summations are taken from i=1 to i=q, q being the total number of input wave trains. Upon substituting for $h_{1i}(u)$ and $h_{2i}(u)$ these become

$$X_1(t) = \sum Z_i(t), \tag{5.8}$$

and

$$X_2(t) = \sum Z_i(t-t_i), \tag{5.8}$$

from which we obtain the transfer functions

$$H_{1i}(f) = 1, \tag{5.9}$$

and

$$H_{2i}(f) = e^{-j2\pi f t_i}, \tag{5.9}$$

where t_i is the time required for the wave train $Z_i(t)$ to pass from sensor 1 to sensor 2.

Assume $Z_i(t)$ to be uncorrelated white-noise sources having zero mean, so that the covariances

$$\begin{aligned} E[Z_i(t)\cdot Z_k(t+t_k)] &= \sigma_i^2 \quad \text{for } t_k=0 \text{ and } i=k \\ &= 0 \quad \text{otherwise,} \end{aligned}$$

where $E[\phi]$ is the expectation operator. By taking $E[X_i(t)\cdot X_k(t)]$, we obtain the covariance functions

$$\gamma_{11}(u) = \sum \sigma_i^2 \cdot \int_0^\infty h_{1i}(v)\cdot h_{1i}(v+u)\,dv, \tag{5.10}$$

$$\gamma_{12}(u) = \sum \sigma_i^2 \cdot \int_0^\infty h_{1i}(v)\cdot h_{2i}(v+u)\,dv, \tag{5.10}$$

$$\gamma_{21}(u) = \sum \sigma_i^2 \cdot \int_0^\infty h_{2i}(v) \cdot h_{1i}(v+u)\,dv, \tag{5.10}$$

and

$$\gamma_{22}(u) = \sum \sigma_i^2 \cdot \int_0^\infty h_{2i}(v) \cdot h_{2i}(v+u)\,dv. \tag{5.10}$$

The covariance functions $\gamma_{12}(u)$ and $\gamma_{21}(u)$ are zero for negative values of the time parameter v, thus allowing us to write them in the form

$$\gamma_{12}(u) = \sum \sigma_i^2 \int_{-\infty}^{\infty} h_{1i}(v) \cdot h_{2i}(v+u)\,dv, \tag{5.11}$$

and

$$\gamma_{21}(u) = \sum \sigma_i^2 \int_{-\infty}^{\infty} h_{2i}(v) \cdot h_{1i}(v+u)\,dv. \tag{5.11}$$

Upon taking the transforms of (5.10) and (5.11) we obtain expressions for the power spectra and cross-spectra of the wave trains $X_1(t)$ and $X_2(t)$ in terms of the transfer functions $H_{1i}(f)$ and $H_{2i}(f)$. Hence,

$$\Gamma_{11}(f) = \sum \sigma_i^2 \cdot |H_{1i}(f)|^2, \tag{5.12}$$

$$\Gamma_{22}(f) = \sum \sigma_i^2 \cdot |H_{2i}(f)|^2, \tag{5.12}$$

$$\Gamma_{12}(f) = \sum \sigma_i^2 \cdot H_{1i}^*(f) \cdot H_{2i}(f), \tag{5.12}$$

and

$$\Gamma_{21}(f) = \sum \sigma_i^2 \cdot H_{2i}^*(f) \cdot H_{1i}(f). \tag{5.12}$$

Then, substituting (5.9) into (5.12) we obtain the power spectra and cross-spectra as functions of the variances σ_i^2 and the travel times t_i of the respective wave trains $Z_i(t)$ crossing the two sensors:

$$\Gamma_{11}(f) = \sum \sigma_i^{\,2}, \tag{5.13}$$

$$\Gamma_{22}(f) = \sum \sigma_i^{\,2}, \tag{5.13}$$

$$\Gamma_{12}(f) = \sum \sigma_i^{\,2} \cdot e^{-j2\pi f t_i}, \tag{5.13}$$

and

$$\Gamma_{21}(f) = \sum \sigma_i^{\,2} \cdot e^{j2\pi f t_i}. \tag{5.13}$$

With the above expressions we now determine the coherence function for the output waves $X_1(t), X_2(t)$ to be

$$\kappa_{12}^{\,2}(f) = \frac{\Gamma_{12}(f) \cdot \Gamma_{21}(f)}{\Gamma_{11}(f) \cdot \Gamma_{22}(f)}, \tag{5.14}$$

or since

$$\Gamma_{21}(f) = \Gamma_{12}^{*}(f), \tag{5.15}$$

$$\kappa_{12}^{\,2}(f) = \frac{|\Gamma_{12}(f)|^2}{\Gamma_{11}(f) \cdot \Gamma_{22}(f)}, \tag{5.16}$$

which, when substituting from above, becomes

$$= \frac{\sum \sum \sigma_i^{\,2} \cdot \sigma_k^{\,2} \cdot \cos[2\pi f(t_i - t_k)]}{\sum \sum \sigma_i^{\,2} \cdot \sigma_k^{\,2}}. \tag{5.16}$$

Backus et al. (1964) found that the absolute value of a zero order Bessel function describes the coherence of isotropic noise; for this special case, equation 5.16 approximates the square of a zero order Bessel function with argument $2\pi fx/V$.

The spectral phase difference between $X_1(t)$ and $X_2(t)$ is

$$\theta_{12}(f) = \tan^{-1}\left\{\frac{-\mathrm{Im}(\Gamma_{12}(f))}{\mathrm{Re}(\Gamma_{12}(f))}\right\},$$

$$= \tan^{-1}\left\{\frac{\sum \sigma_i^2 \cdot \sin(2\pi f t_i)}{\sum \sigma_i^2 \cdot \cos(2\pi f t_i)}\right\}, \tag{5.17}$$

and

$$\Theta_{21}(f) = -\Theta_{12}(f). \tag{5.18}$$

5.4 Comparison of Models With Observations

In this section, we compute the model coherence, described by the positive square root of (5.16) for an array of six sensors positioned as shown in figure 5.14; all computations are for the center sensor, plus one of the others. The model velocity is 3.5 km/s.

As a first example, we take a noise field produced by two equal output white sources arranged as shown in figure 5.14a. The model coherence for this example, figure 5.15, shows a strong azimuthal dependency, as well as secondary maxima occurring at integral multiples of $\frac{1}{|t_1-t_2|}$. The amplitude of the secondary maxima, however, are larger than those observed from the real data (compare fig. 5.15 with fig. 5.11). For a more realistic example, we take equally spaced, equal output white-noise sources (fig. 5.14b) modeling a broad source area. The model coherence for this example (fig. 5.16) shows features, including azimuthal dependency and secondary maxima, similar to those of the real coherence estimates (compare fig. 5.16 with fig. 5.11). Furthermore, the coherence

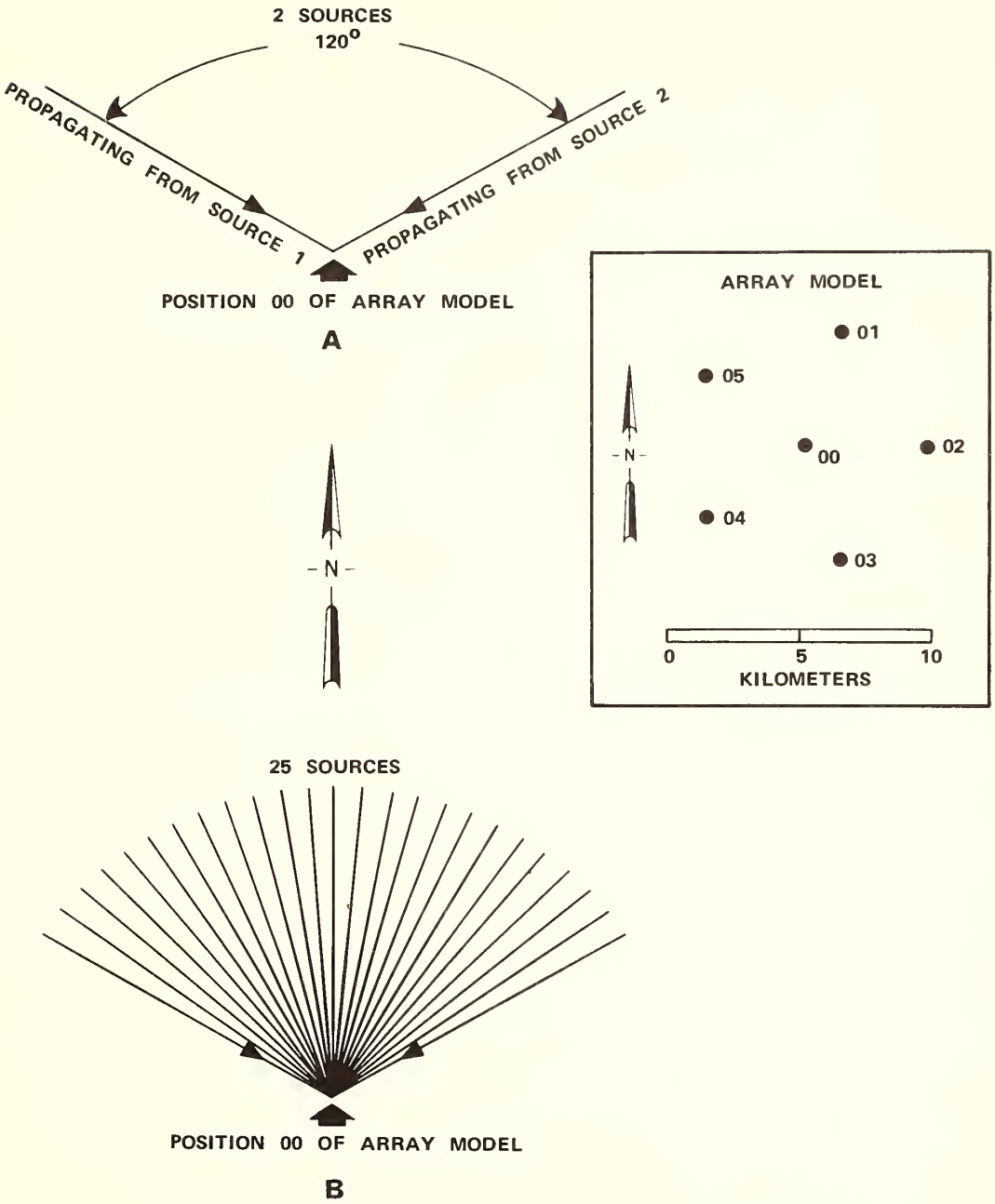

Figure 5.14. Model of two and 25 sources.

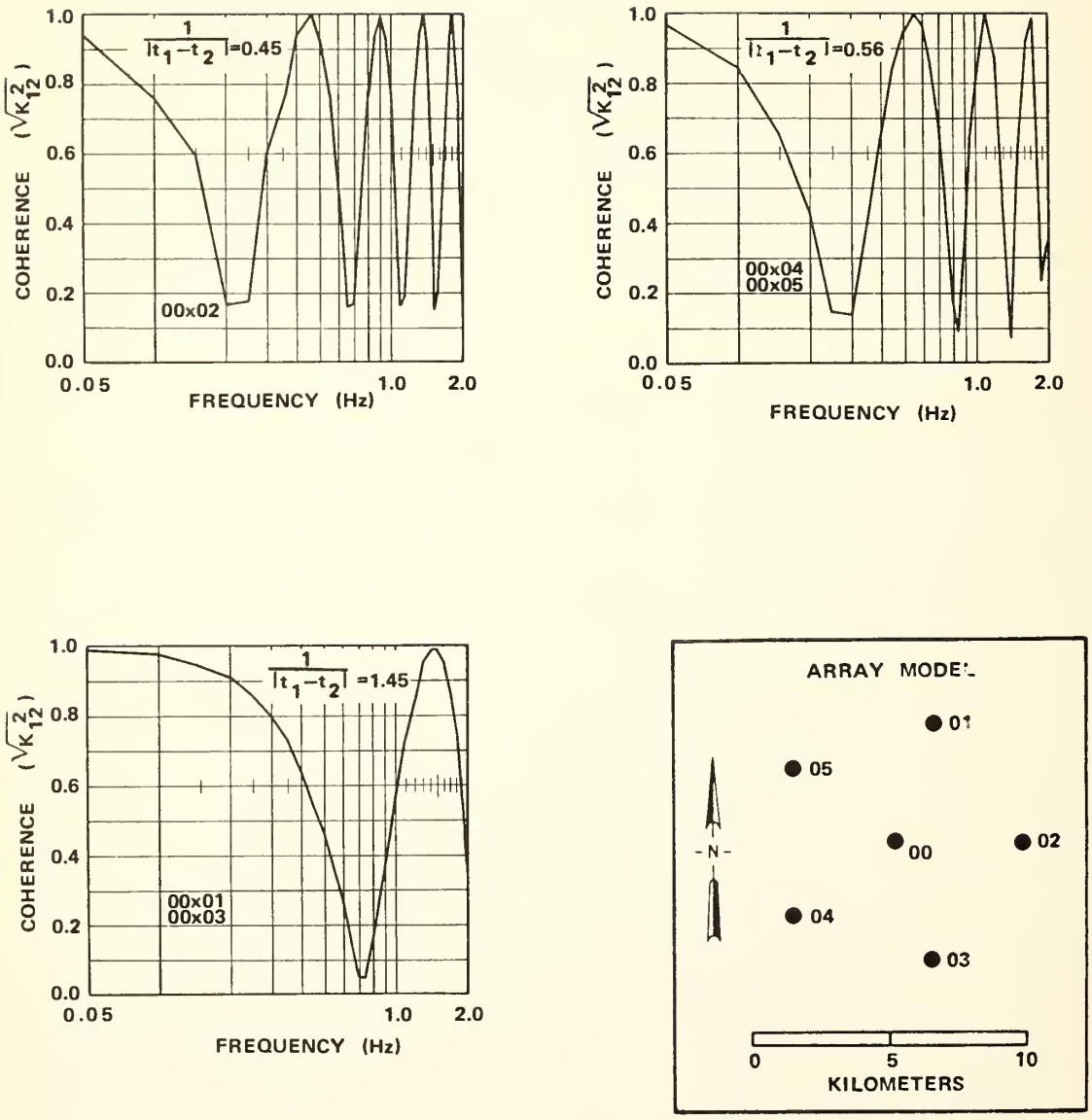

Figure 5.15. Model coherence for the two sources displayed in figure 5.14. The model pairs are indicated on each graph.

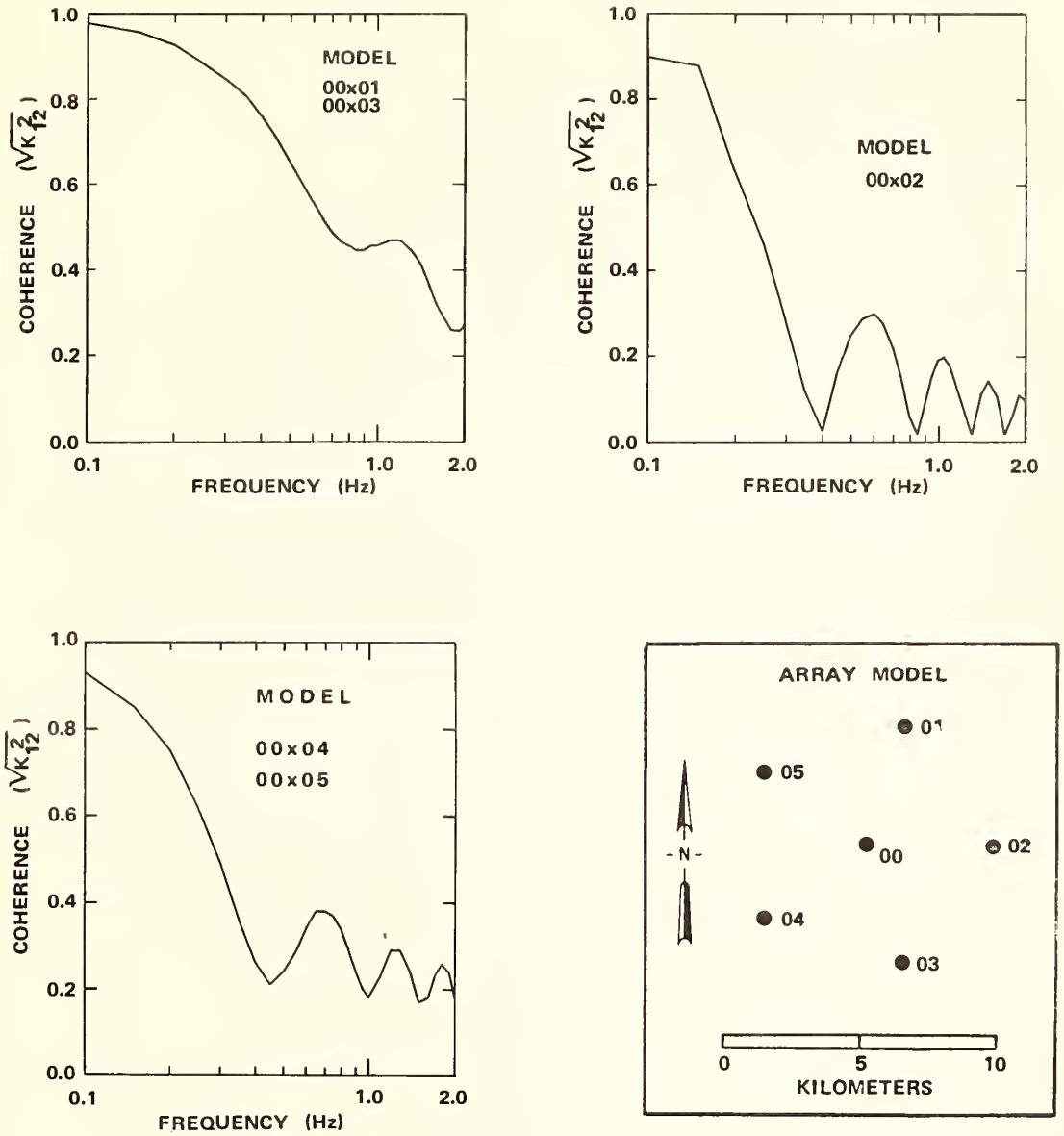

Figure 5.16. Model coherence for the 25 sources displayed in figure 5.14. The model pairs are indicated on each graph.

polygons of the model (fig. 5.17) have shapes similar to those constructed for the real data. Dissimilarities, such as amplitude differences between the modeled and the real data, probably result from the simplifying assumptions made for the model--in particular, the model contains no operation decreasing the coherence as a function of distance between sensors. In the real earth we expect a distance-dependent function to exist.

An interference process, modeling the noise field, permits time-varying coherence as measured by the simple cross-spectral method. The change in computed coherence can be caused by

(1) change in position of the sources, i.e., t_i of (5.6) changes, and

(2) differential change in the output of the sources.

We, in section 5.2, and Bungum, Bruland, and Rygg (1969) observed time varying coherence at NORSAR, as well as time varying orientations of the polygons--observations suggesting that the source is both broad and mobile. Bungum and his co-workers make similar conclusions, enhancing our confidence that the model is realistic.

5.5 Time Parameters of the Model

In the development of the coherence model, no attempt was made to fit the resulting model phase spectra to the NORSAR data. A valid comparison requires both phase estimates with minimum bias (especially at the lower frequencies) and surface-wave dispersion functions for the NORSAR area; neither are available. Even though the model phase spectra may be a poor fit to the real data, some features of the model are noteworthy.

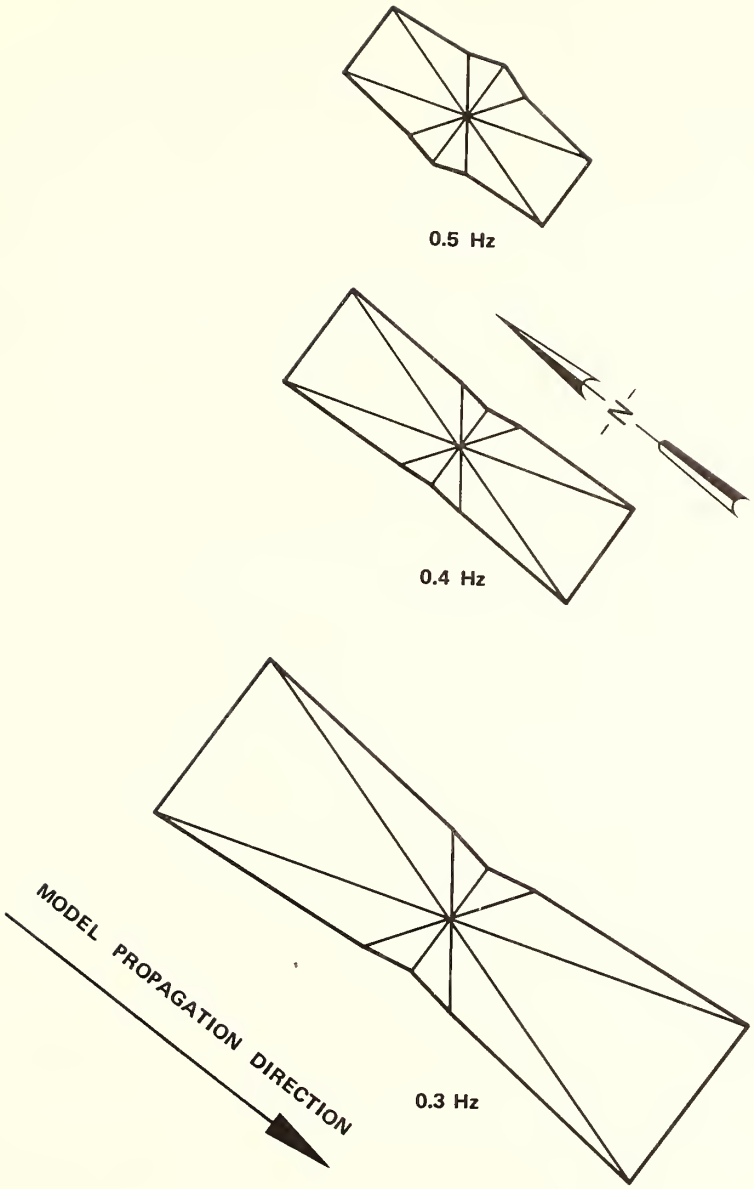

Figure 5.17. Coherence polygons made from the model coherence for 25 sources. The propagation direction of the central ray is shown.

The phase spectra for the 25-source model (fig. 5.14) is shown in figure 5.18. The sensor pair (00x02) aligned perpendicular to the center ray produces approximately zero time delay at the lower frequencies, an observation we intuitively expect from the symmetry of the source. At frequencies higher than that corresponding to the first minimum in the coherence (see fig. 5.16), the 00x02 phase angle fluctuates between 0 and

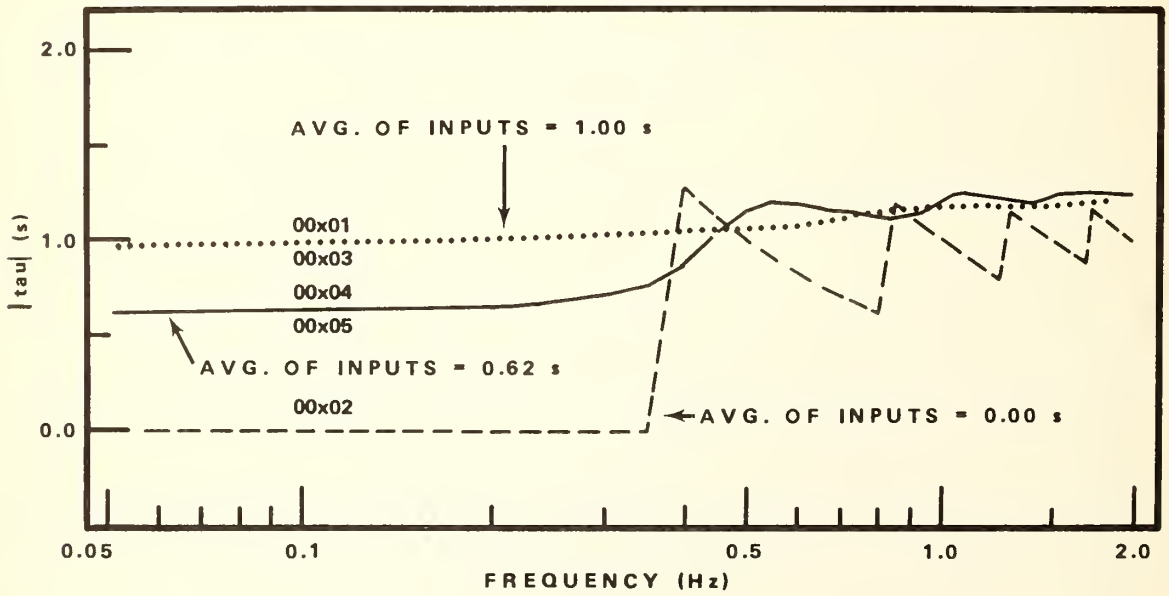

Figure 5.18. Interpreted tau of the 25-source model shown in figure 5.14.

π, making the time delay difficult to interpret--we assumed increasing phase to plot the time delay. For the other sensor pairs, the conversion from phase to time delay was more straightforward. At the lower frequencies, the pairs also produce time delays that are approximately those of the averages of the respective suites of rays (see fig. 5.18). At the higher frequencies, however, fluctuations in the time delays are less pronounced than are those of 00x02.

The model velocity was a constant 3.5 km/s, but the time delays (fig. 5.18) vary as a function of frequency. The set of time delays produce the illusions of a dispersive medium and of a frequency dependent azimuth of approach.

6. MICROSEISM AND METEOROLOGICAL CONDITIONS

6.1 Correlation of Meteorological Activity With Time-Varying Microseismic Trends

To search for correlating trends at NORSAR, we compared gross features shown on surface meteorological maps, obtained from the Norwegian Weather Bureau in Bergen, with microseism amplitudes measured at times corresponding to those of the maps (as described in sec. 4.1, microseisms were sampled at 7-hour intervals; each map comparison was made to the amplitude of the nearest sample). Selected maps are compared with time-correlating microseism amplitudes, at 0.3 Hz and 1.0 Hz, in figures 6.1 and 6.2. To facilitate referencing specific examples, each map is given an alphabetic designation. The map designations are chronologically ordered in figure 6.3, which also shows chronologically ordered microseism trends.

Because of popular concepts of microseism generation by atmospheric-induced marine conditions (Longuet-Higgins, 1950, 1952; Hasselmann, 1963), and because of previous correlations we (Murdock et al., 1968) found from studying a microseism field in Australia (fig. 6.4), we searched for correlations of variations in microseismic amplitudes with variations of meteorological conditions over the oceanic and Scandinavian coastal areas. We found that a large band of amplitudes--representative of the entire range--existed for a given meteorological condition; in particular,

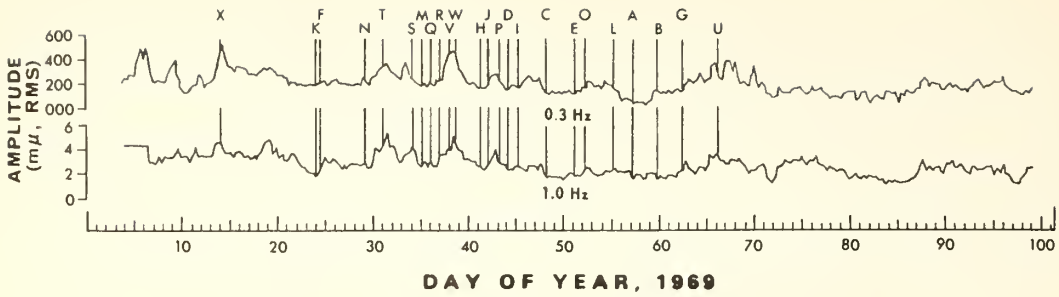

Figure 6.3. Microseisms trends and times described by meteorological maps. The alphabetic designation corresponds to figures 6.1 and 6.2.

representative values of the entire microseism amplitude range exist when

(1) low pressure zones are over the east Atlantic Ocean (see map set B, C, F, G, K, N, Q, T, X),

(2) high pressure zones are over the east Atlantic Ocean (see map set D, H, I, J, M, V),

(3) steep barometric gradients are at Scandinavian coast lines (see map set A, E, P, R, S, T, U, W, X).

Although variations in meteorological conditions in the coastal and oceanic areas appear to show no correlation with variations in the 0.3-Hz and 1.0-Hz microseisms recorded at NORSAR, variations in the barometric gradient on the peninsula near NORSAR do seem to correlate with microseismic variations--low gradients occurring at times when the microseismic amplitudes are small and high gradients occurring at times when the amplitudes are large (see map set B, E, F, H, I, L, R, T, U, V, W, X). Similar correlations (fig. 6.5) were found by us (Murdock et al., 1968) from data recorded in Australia--in addition to the correlation shown in fig. 6.4.

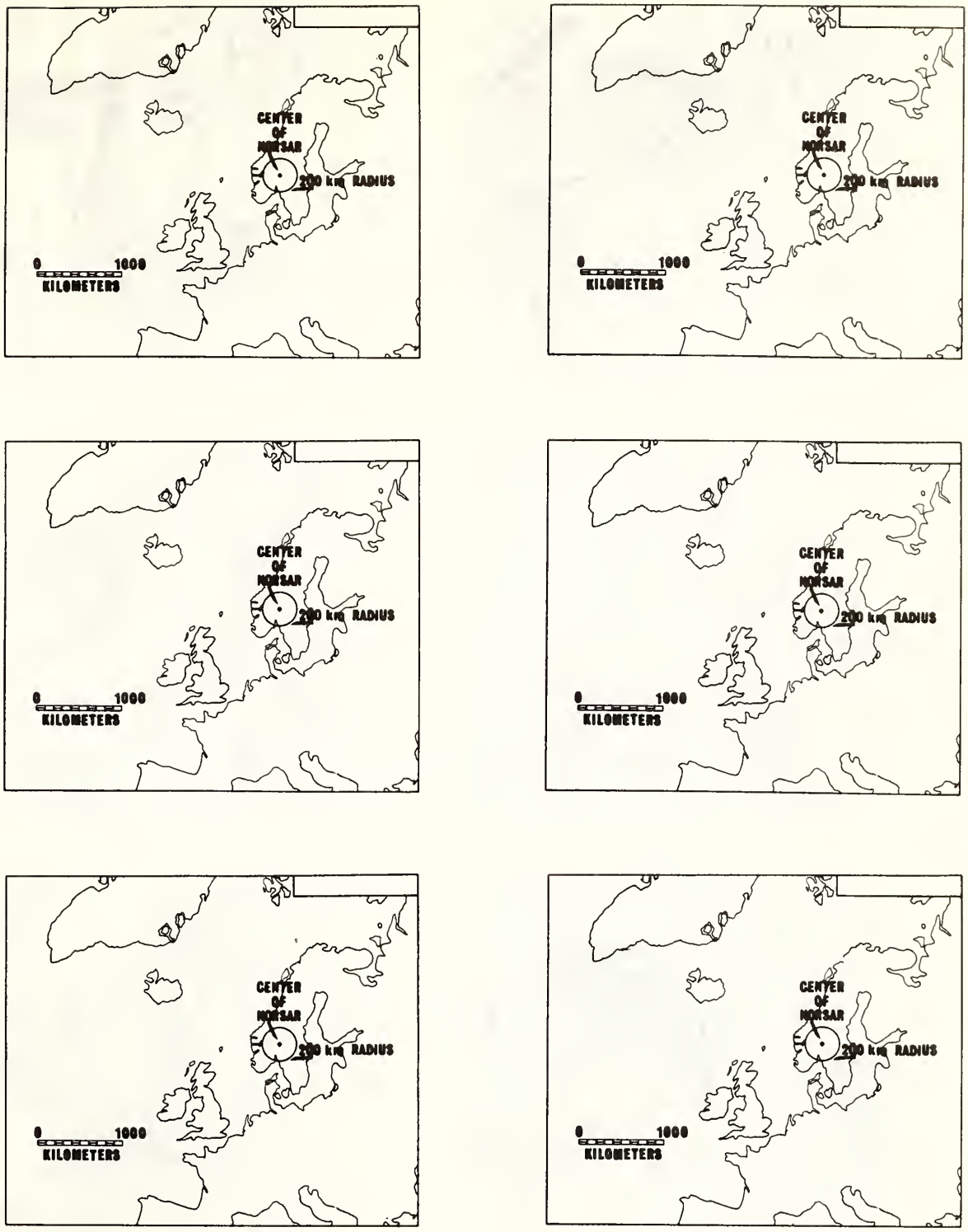

OVERLAY TO FIGURES 6.1. AND 6.2.

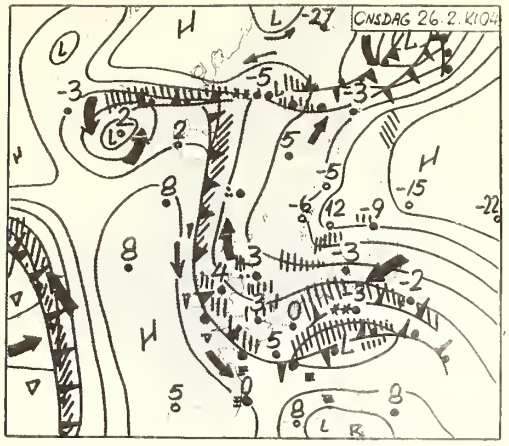

A 90 mμ

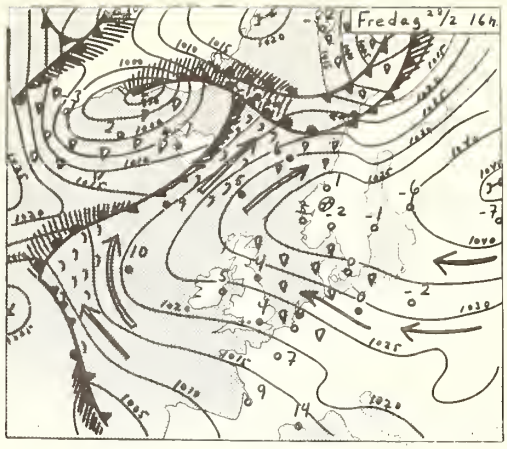

B 113 mμ

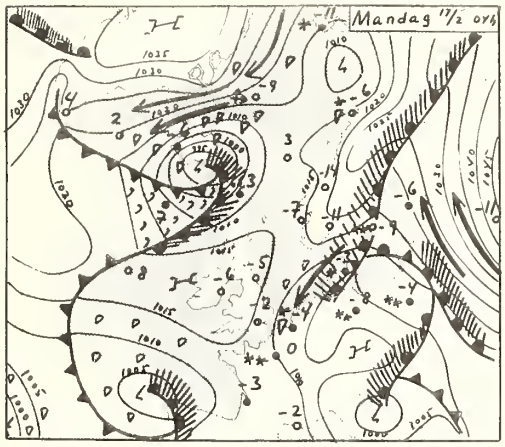

C 124 mμ

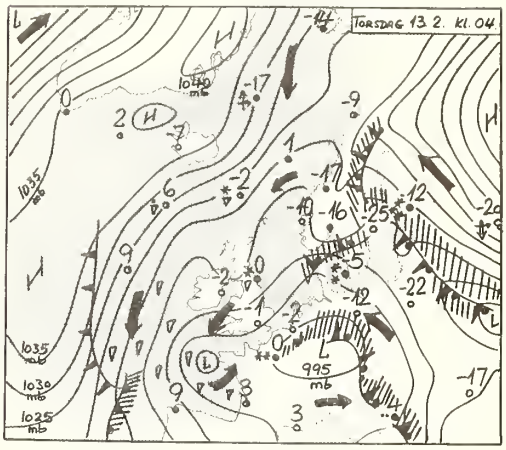

D 147 mμ

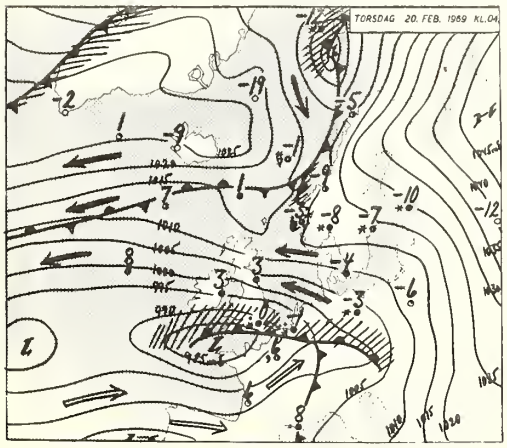

E 164 mμ

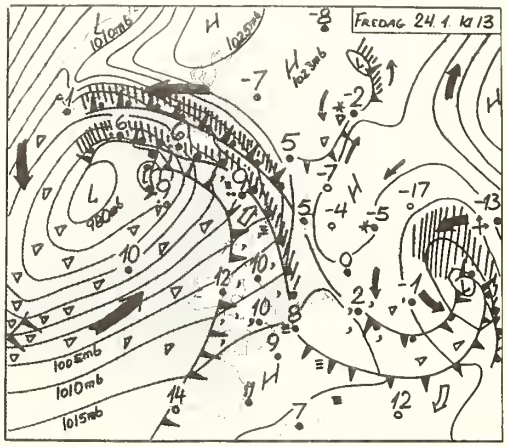

F 181 mμ

Figure 6.1. Selected meteorological maps Compared with root-mean-square trends of microseisms in the band near 0.3 Hz. The maps are arranged in order of increasing microseism amplitudes.

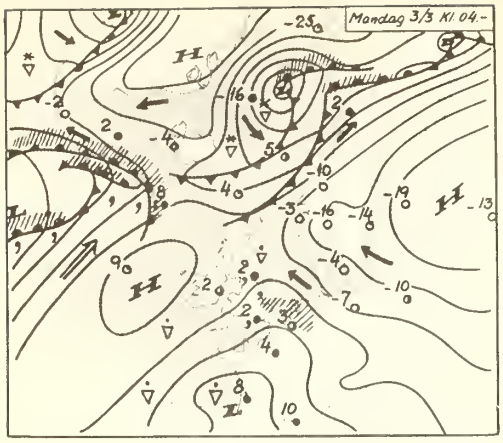

G 181 mμ

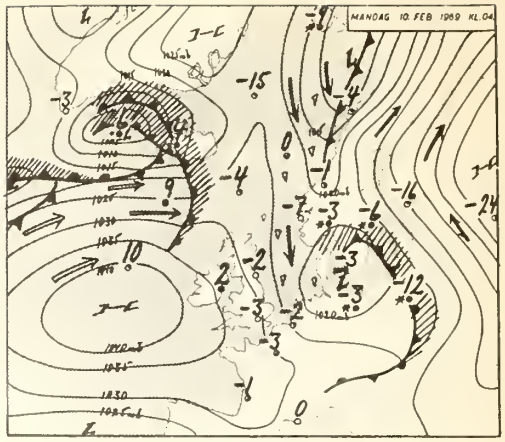

H 192 mμ

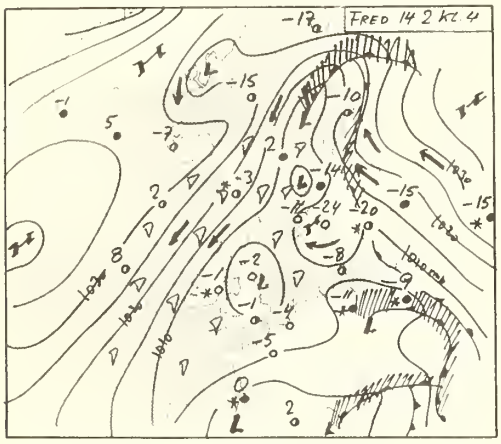

I 192 mμ

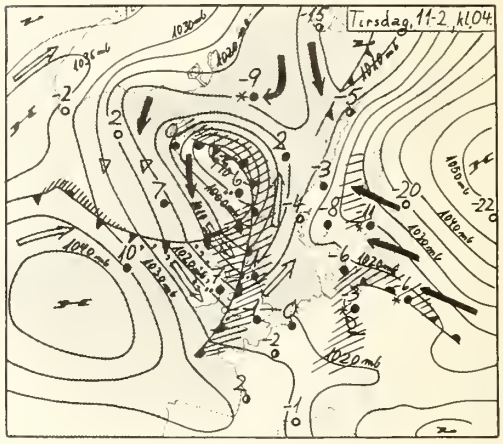

J 201 mμ

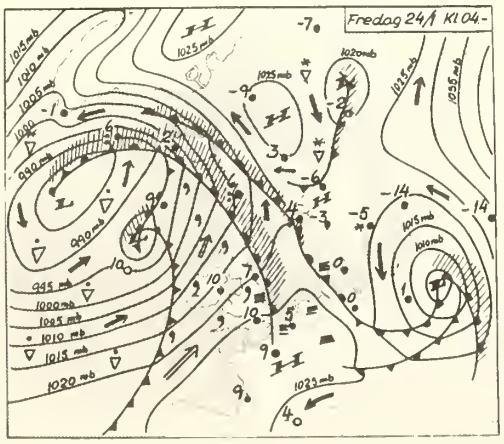

K 203 mμ

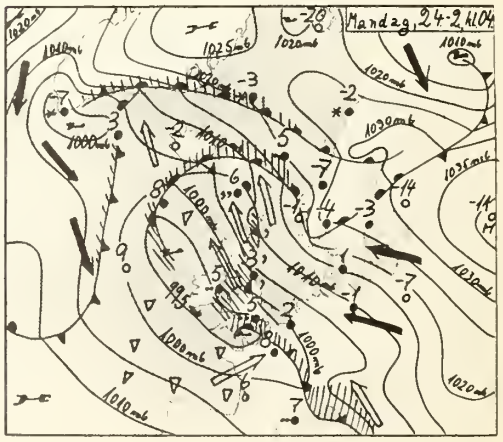

L 209 mμ

Figure 6.1. (continued).

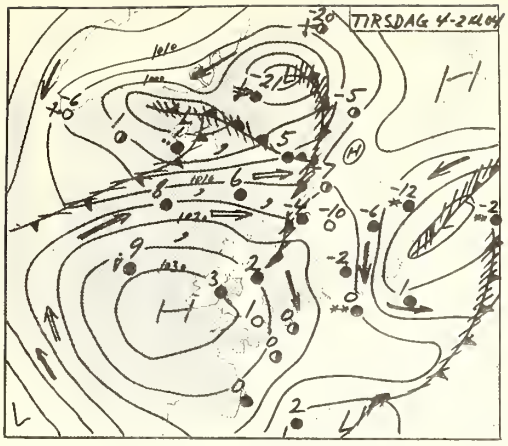

M 215 mμ

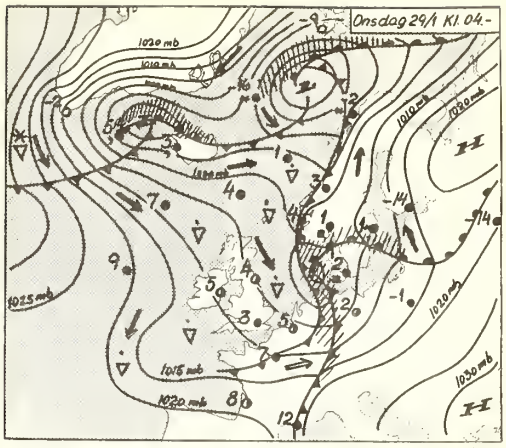

N 247 mμ

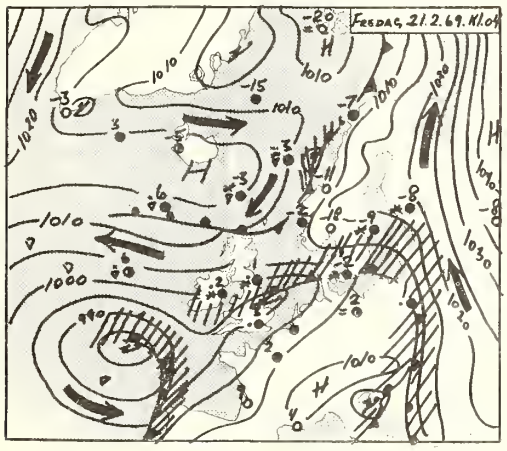

O 249 mμ

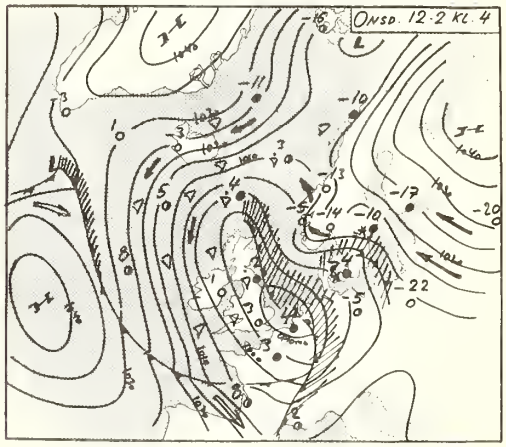

P 249 mμ

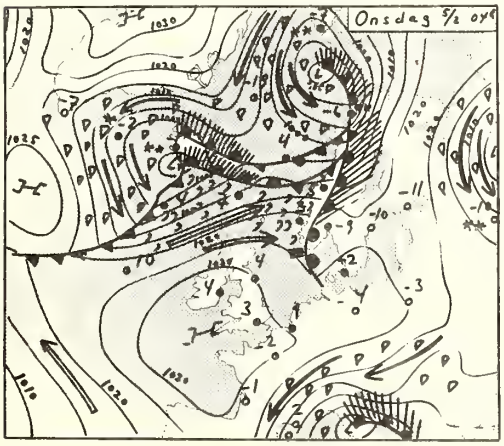

Q 254 mμ

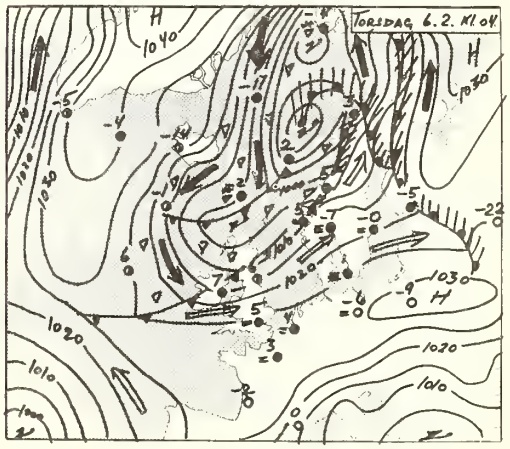

R 283 mμ

Figure 6.1. (continued)

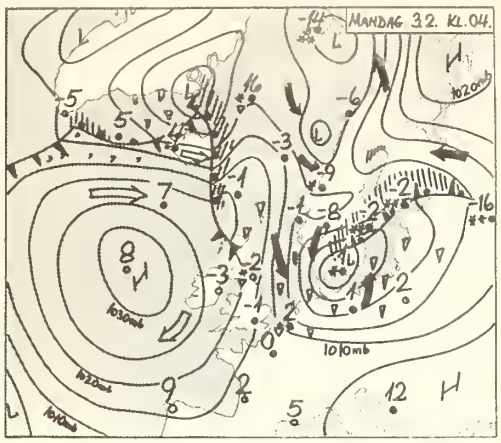

S 305 mμ

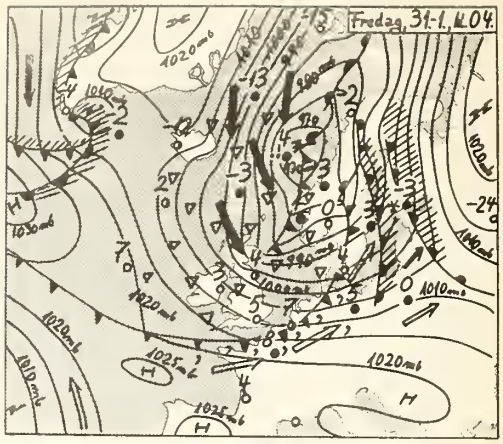

T 373 mμ

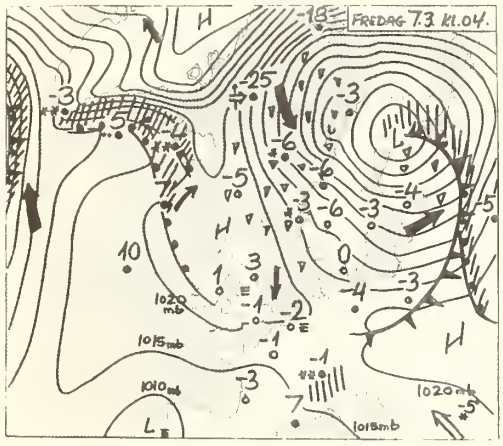

U 452 mμ

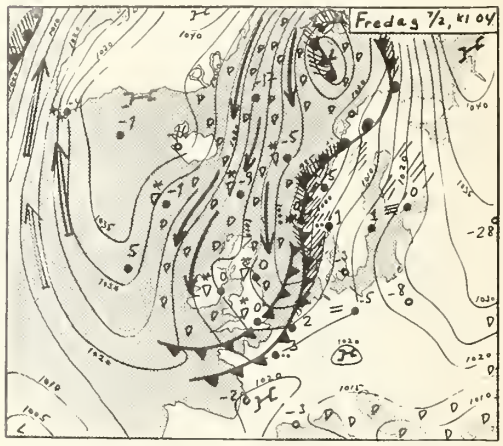

V 537 mμ

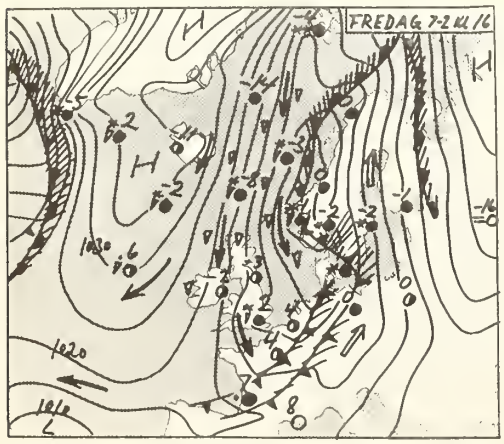

W 542 mμ

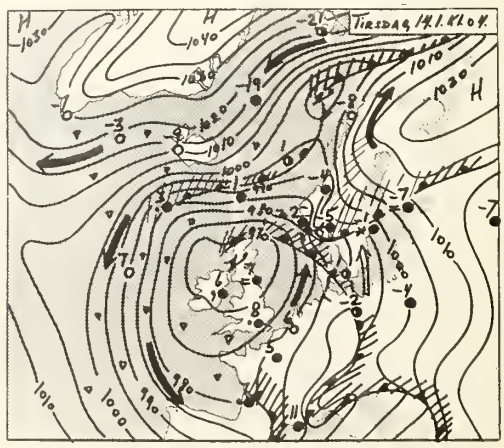

X 610 mμ

Figure 6.1. (continued)

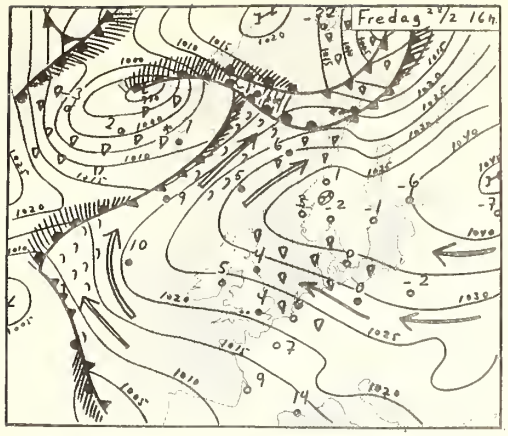

B 2.1 mμ

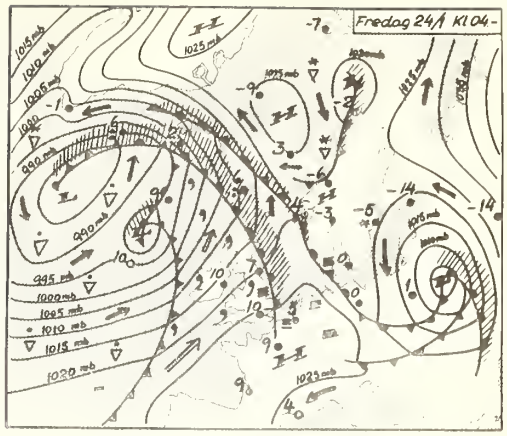

K 2.3 mμ

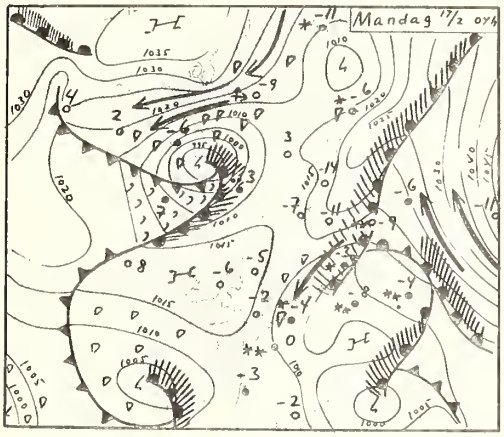

C 2.3 mμ

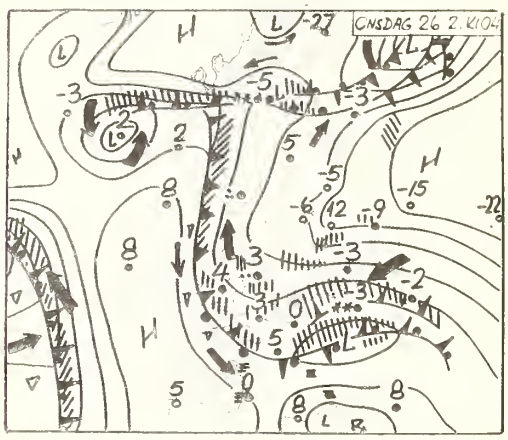

A 2.4 mμ

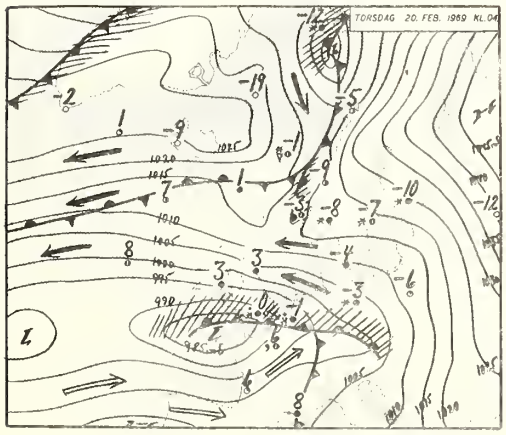

E 2.4 mμ

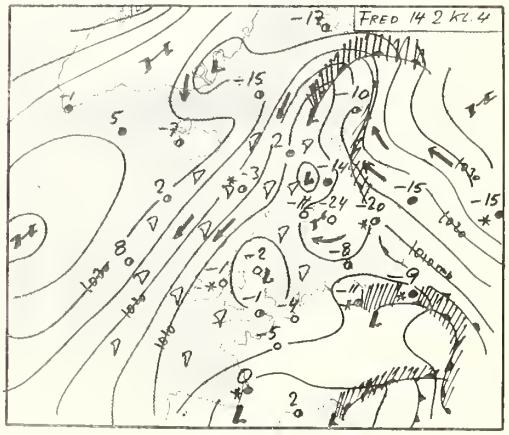

I 2.5 mμ

Figure 6.2. Selected meteorological maps compared with root-mean-square trends of microseisms in the band near 1.0 Hz. Map designation is that of figure 6.1.

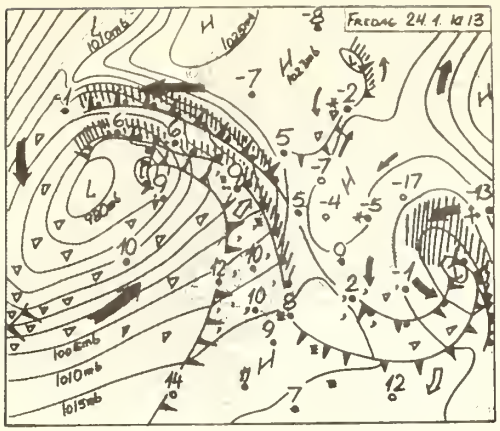

F 2.6 mμ

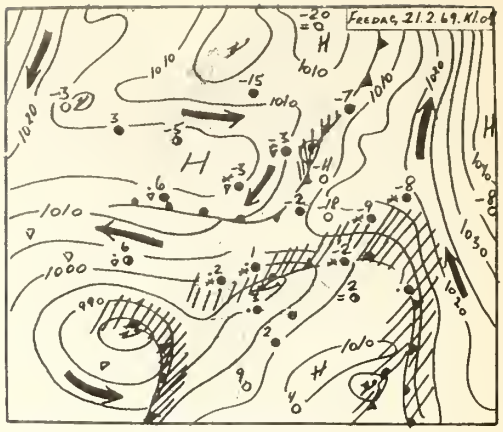

O 2.6 mμ

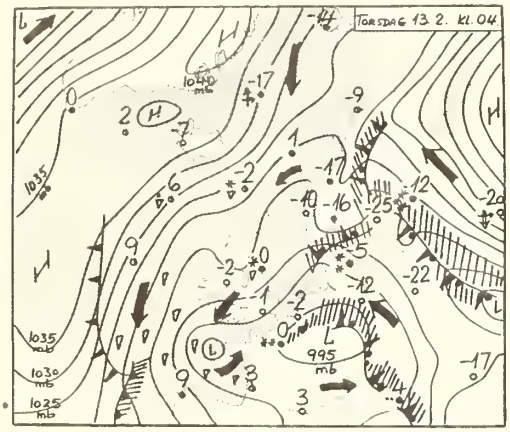

D 2.7 mμ

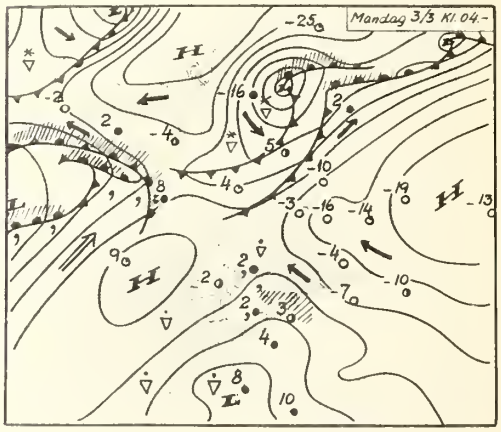

G 2.8 mμ

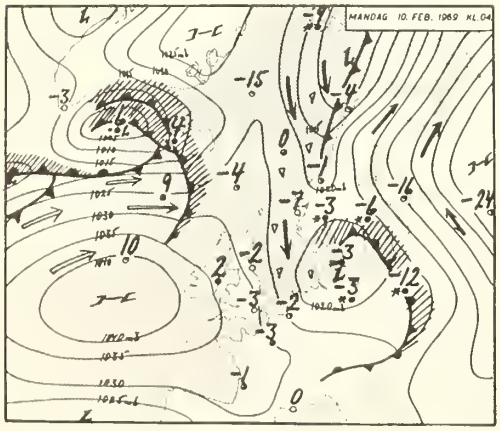

H 2.8 mμ

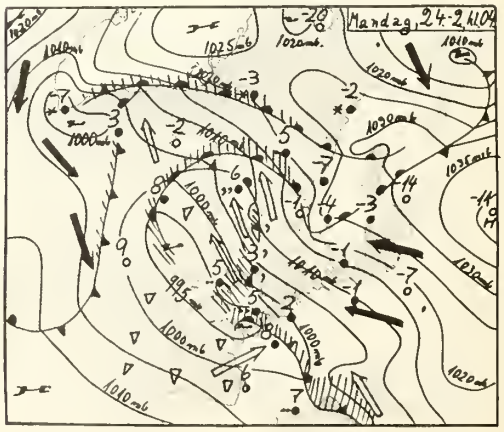

L 2.8 mμ

Figure 6.2. (continued).

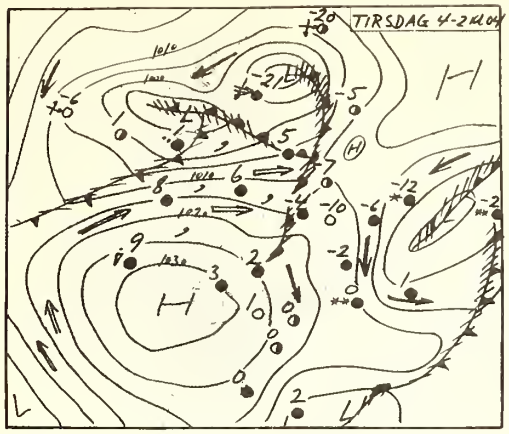

M 2.9 mμ

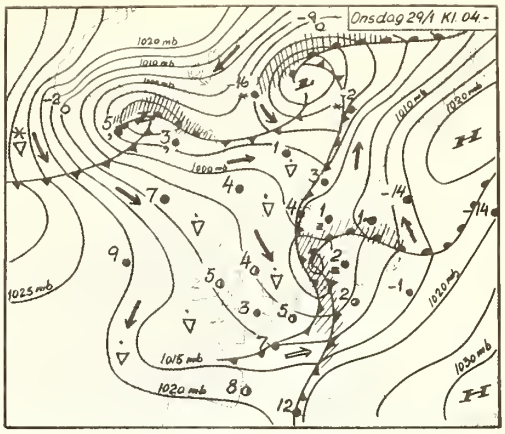

N 3.1 mμ

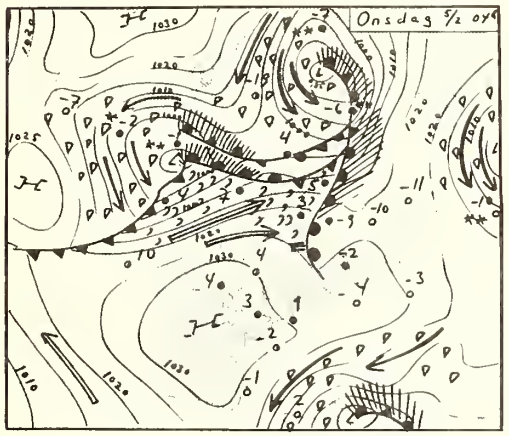

Q 3.1 mμ

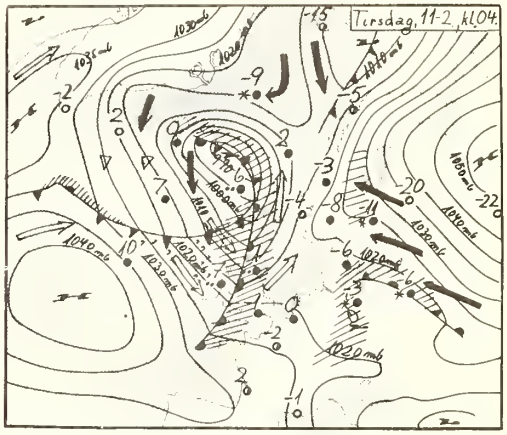

J 3.2 mμ

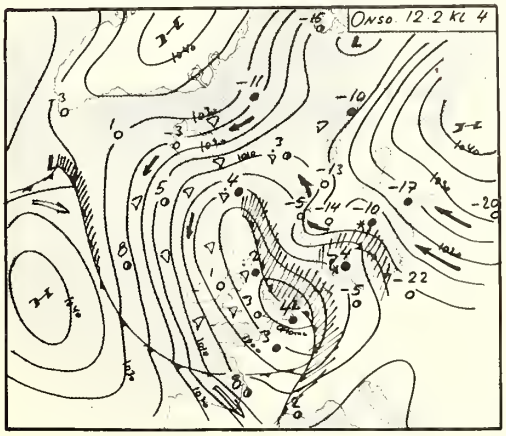

P 3.5 mμ

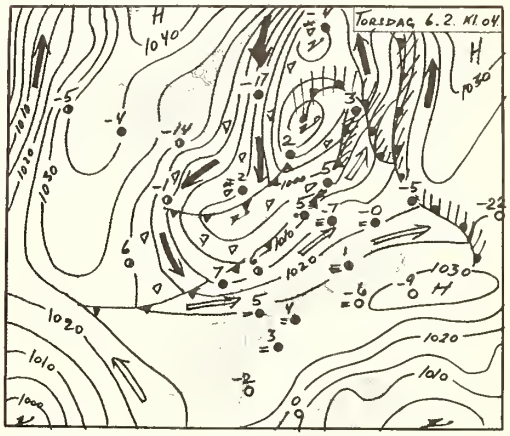

R 3.8 mμ

Figure 6.2. (continued).

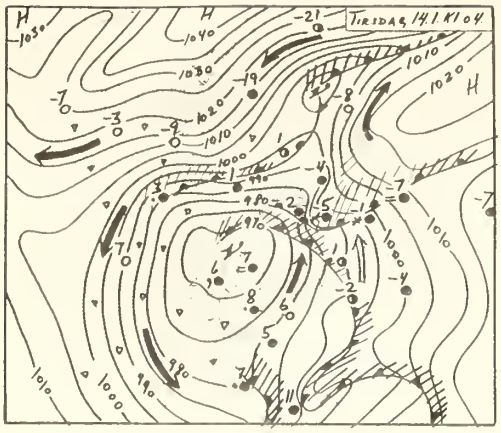

X 4.2 mμ

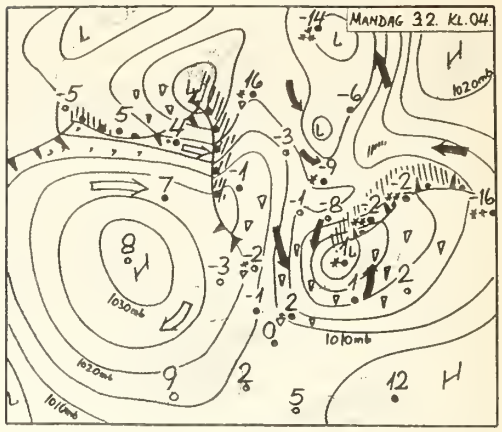

S 4.5 mμ

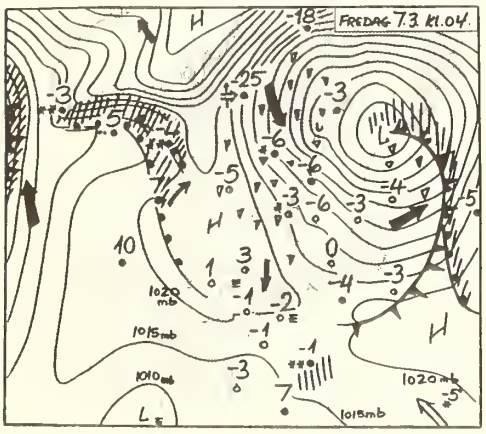

U 4.6 mμ

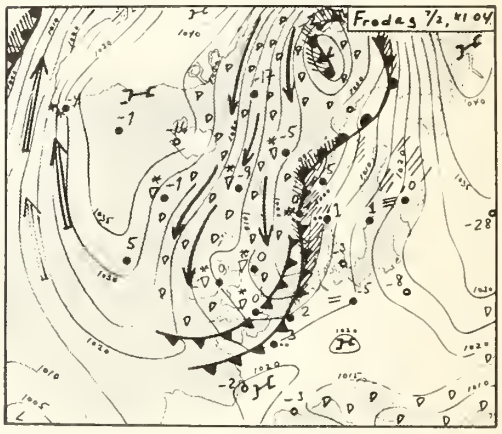

V 4.7 mμ

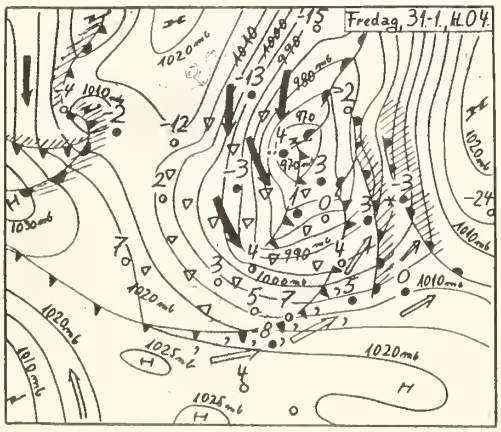

T 5.3 mμ

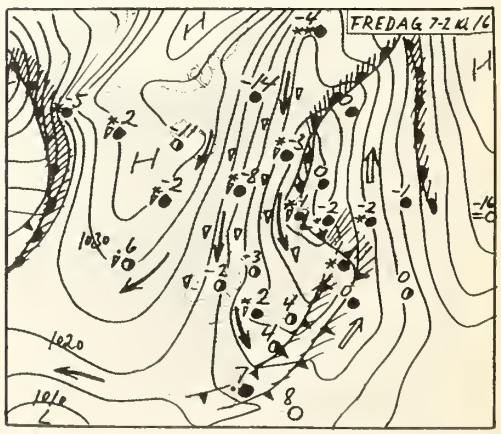

W 5.4 mμ

Figure 6.2. (continued).

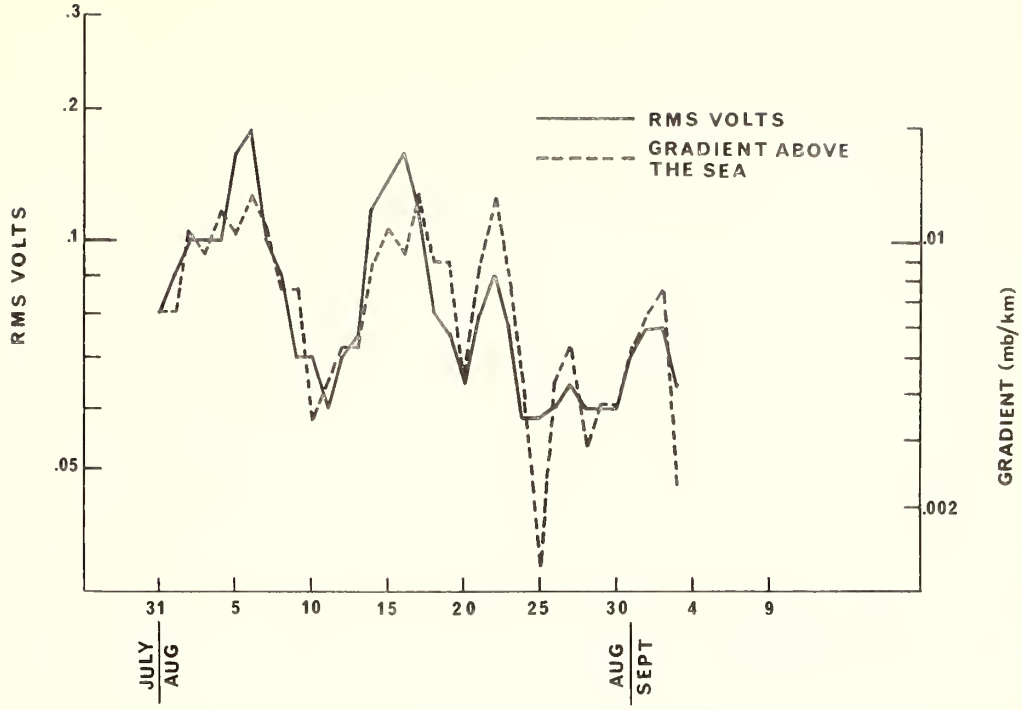

Figure 6.4. Comparison between barometric pressure gradient occuring over the Gulf of Carpentaria and root-mean-square amplitudes at 1.0 Hz recorded at Daly Waters, Northern Territory.

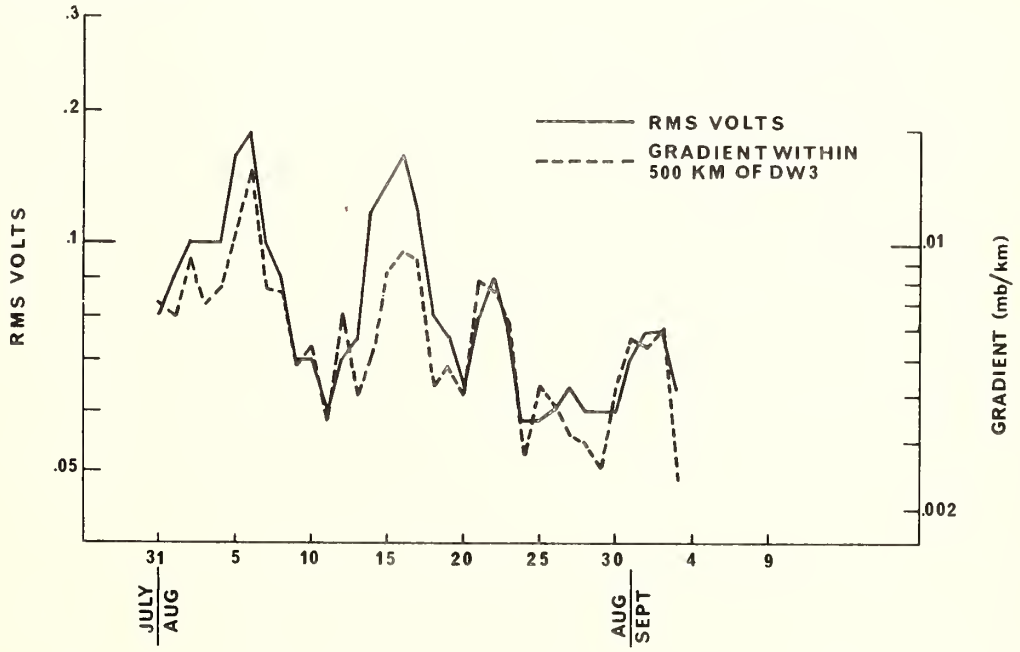

Figure 6.5. Comparison between barometric pressure gradient in the Daly Waters area and root-mean-square amplitudes at 1.0 Hz recorded at Daly Waters.

For further correlations between barometric gradients and microseismic activity, we obtained detailed meteorological maps, compiled at 12-hour intervals, from the Norwegian Meteorological Institute in Oslo. Pilot studies performed (figs. 6.6 to 6.8) included comparisons of the microseism trends with the following estimates of barometric trends:

Maximum gradient: $\frac{Px - Pc}{R}$,

where Px minus Pc is the maximum difference between the pressure at the center of NORSAR (Pc) and that (Px) on a circle of radius R from the center of NORSAR.

Maximum-opposite gradient: $\frac{Px - Pc + Py - Pc}{2R}$

where Py is measured on the circle 180° from Px.

Average gradient: $\frac{Pn - Pc + Pe - Pc + Ps - Pc + Pw - Pc}{4R}$

where Pn, Pe, Ps, and Pw are measured on a circle of radius R at the four compass directions from the center of NORSAR.

N-S gradient: $\frac{Pn - Pc + Ps - Pc}{2R}$

The maximum gradient, determined from measurements made 200 km from the center of NORSAR (fig. 6.8) seems to show one of the better correlations with the microseism amplitudes displayed; the weighted average of the microseisms displayed is $(100 \times A_{1.0} + A_{0.3})/2$ sampled at 12-hour intervals. Data for days 30 to 100 seem to correlate better than data for days 10 to 30. In some instances, such as between days 35 and 40, the gradient trend seems to lead the microseism trend by 12 to 24 hours.

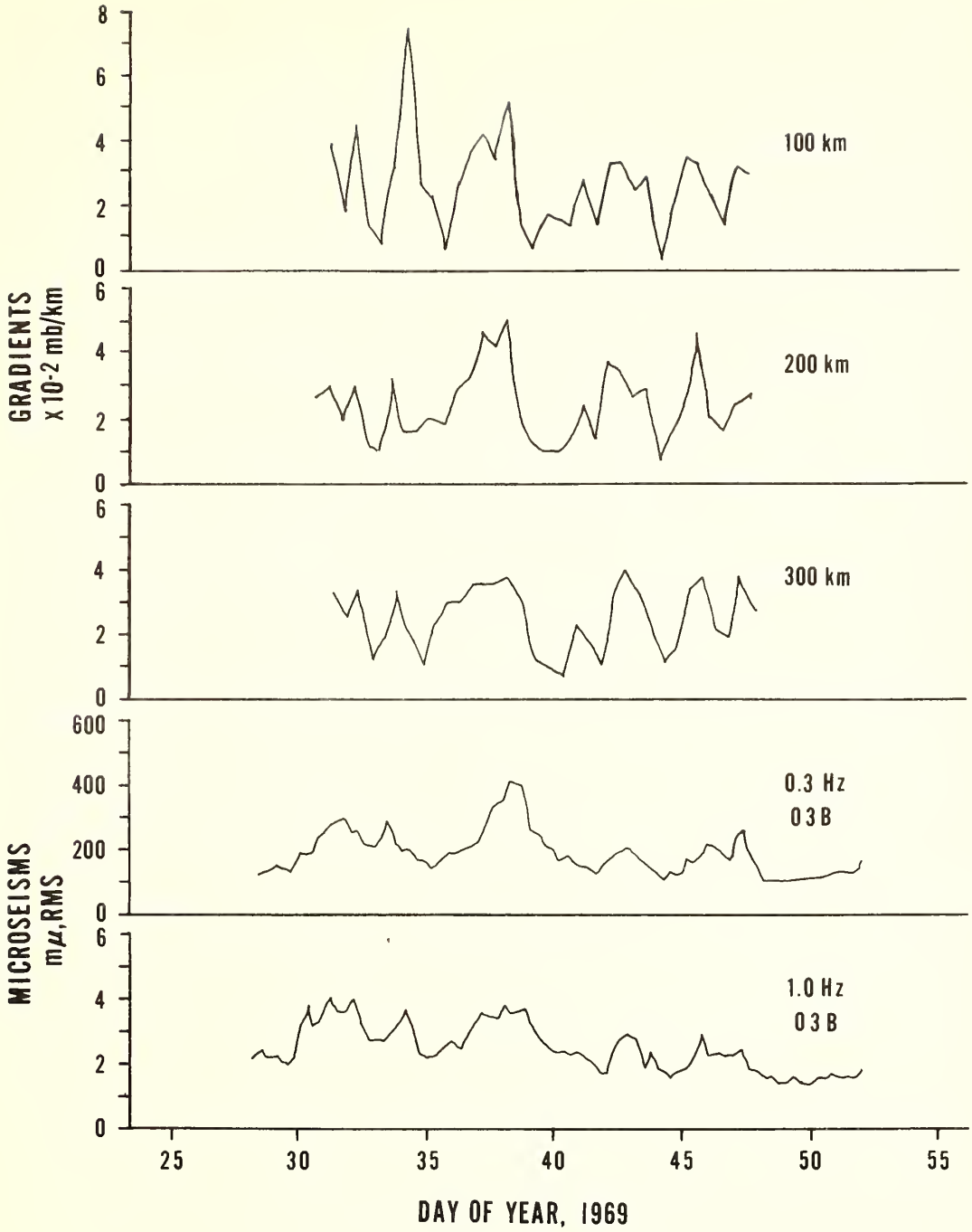

Figure 6.6. Pilot studies performed to find a correlation between barometric gradients and root-mean-square trends. The maximum gradients observed for 100 km, 200 km, and 300 km (R) from the center of NORSAR are shown.

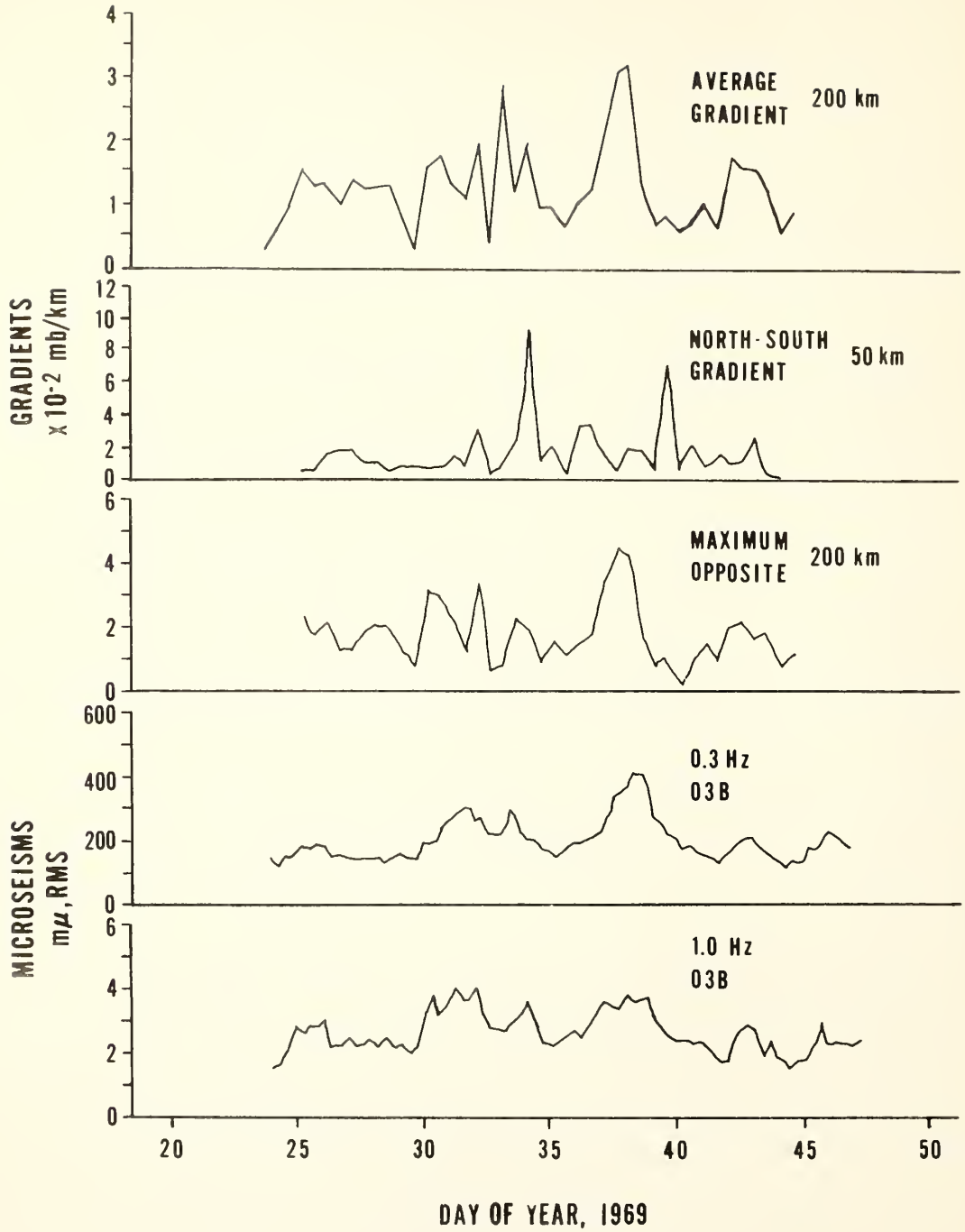

Figure 6.7. Pilot studies performed to find a correlation between barometric gradients and root-mean square trends of microseisms. The radi (R) from the center of NORSAR are indicated on the trends.

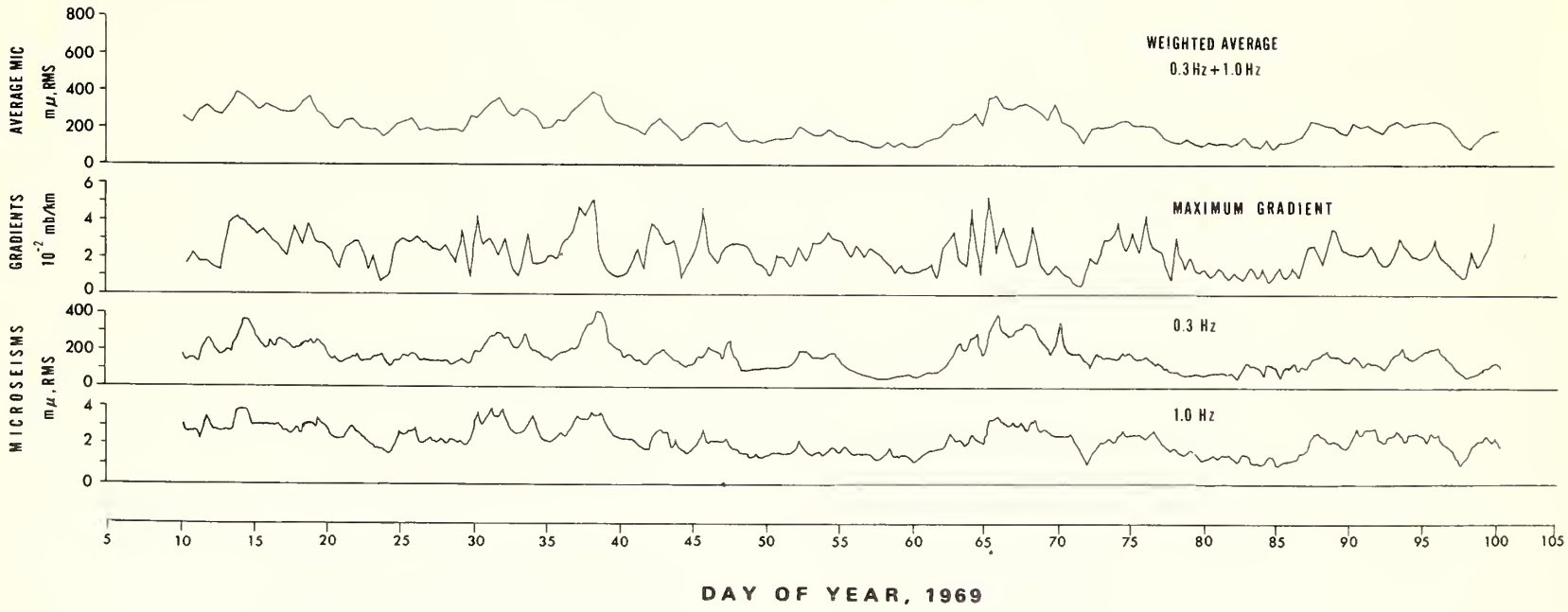

Figure 6.8. Comparison of microseism trends and the maximum barometric gradients for a distance (R) of 200 km from the center of NORSAR.

6.2 Discussion

If the correlation we show is meaningful, then it seems to be in conflict with the popular concept of microseism generation by atmospheric-induced marine conditions. Although his conclusions support the popular concept, Santô (1962), by studying microseisms recorded in Sweden, reported the following that we believe are consistent with local sources of microseisms:

> An example showing the poor transmission of microseismic waves, especially of short period, is the following. On march 31st, 1962, a cyclone (p_c = 980 mb) arrived just at the southernmost edge of Sweden. This produced a remarkable short-period (around 2.5 seconds) microseism storm at Karlskrona, quite near the cyclonic center. But there was almost nothing at Uppsala which is only about 350 km apart.
>
> The same results are clearly observed in Japan. When a cyclone runs over the Pacific Ocean from south to north, the microseismic storm shifts gradually from southwestern stations to northeastern, as if it runs after the cyclone. In other words, microseism storms in Japan occur quite independently at many places located near each other.
>
> Passages of energy sources across the Baltic Sea hardly increase microseismic amplitudes even at Uppsala, as far as those with periods of more than 4 or 5 seconds are concerned. However, a small amplitude increase is observed at Uppsala for microseisms of shorter periods...(p. 371)
>
> As to the remarkable storm (microseismic storm) which occurred only at Kiruna about 26 d 12 h, the general explanation from the intensity or the movement of a cyclone only is impossible. The only indication the writer could find from the meteorological data was a small cyclone (1005 mb) very near Kiruna at 26 d 06 h, and that the greatest wind velocity was measured at the northernmost coast of Norway just at that time...(p. 361)

His observations above also suggest to us the possibility that microseisms

may be generated over land, as does the correlation we show (fig. 6.8).

As an alternate interpretation of the data in figure 6.8, there may be a large time lag between the atmospheric driving force and the marine generation of microseisms (essentially Santô's hypothesis). The barometric gradient near NORSAR, therefore, may be indicative only of past or future marine atmospheric conditions that actually cause the microseismic activity--an interpretation supported by the observed westerly approach of the 0.3-Hz microseisms (sec. 5), suggestive of their marine origin. Regardless of the microseisms' source, however, the observed correlation may prove a valuable tool in the short-term prediction of impending microseismic levels.

7. OBSERVED EARTHQUAKE SIGNALS

7.1 Data Reduction Techniques

For the 20 to 88 day interval, 1969, one seismic channel of each magnetic tape was monitored by an interpreter who listened to the playback output by using an audio band speaker (playback speed was 80 times real time). Paper seismograms, with magnifications in the range of 2×10^5 to 4×10^5 were produced to show recordings of all sounds interpreted to be seismic signals. Arrival times of signals seen on the paper seismograms were compared with expected earthquake arrival times, estimated from information provided by the National Center for Earthquake Information in their Preliminary Determination of Epicenters bulletins (PDE cards). A list was made containing the following information:

(1) earthquakes that produced time-correlating signals at NORSAR,

(2) earthquakes that did not produce time-correlating signals at

NORSAR,

(3) magnitude (m_b) of each earthquake, obtained from the PDE cards,

(4) epicentral distances from the center of NORSAR for each earthquake location given on the PDE cards, and

(5) the focal depth of each earthquake given on the PDE cards.

From each paper seismogram showing a clearly recorded earthquake signal, we measured the dominant signal frequency occurring within approximately 2 s after signal onset. An average signal frequency was then computed for each earthquake.

7.2 NORSAR Detection Threshold for Teleseisms

From the earthquake list described above, we constructed figure 7.1, which shows the detection threshold of a single NORSAR seismometer for shallow ($h \leq 50$ km) teleseisms, and figure 7.2, which shows the detection threshold for deep ($h > 50$ km) teleseisms. In these illustrations, trend lines describe both the upper magnitude limits of teleseisms not recorded and the lower magnitude limits of teleseisms recorded. In figure 7.1, the trend lines show the following three approximate linear trends: (1) the threshold increases from 4.6 at 20° to 4.8 at 68°, (2) the threshold increases from 4.9 at 80° to 5.7 at 100°, and (3) though poorly defined, the threshold decreases from approximately 5.8 at 137° to 4.8 at 150°. In the interval between 68° to 80°, the linear trends are interrupted by a decrease of approximately 0.5 unit, followed by an increase of approximately 0.5 unit. (These features are also shown in fig. 7.2, detection threshold of deep earthquakes). No shallow events were recorded in the range 110° to 136°. The detection threshold graph for deep events (fig. 7.2)

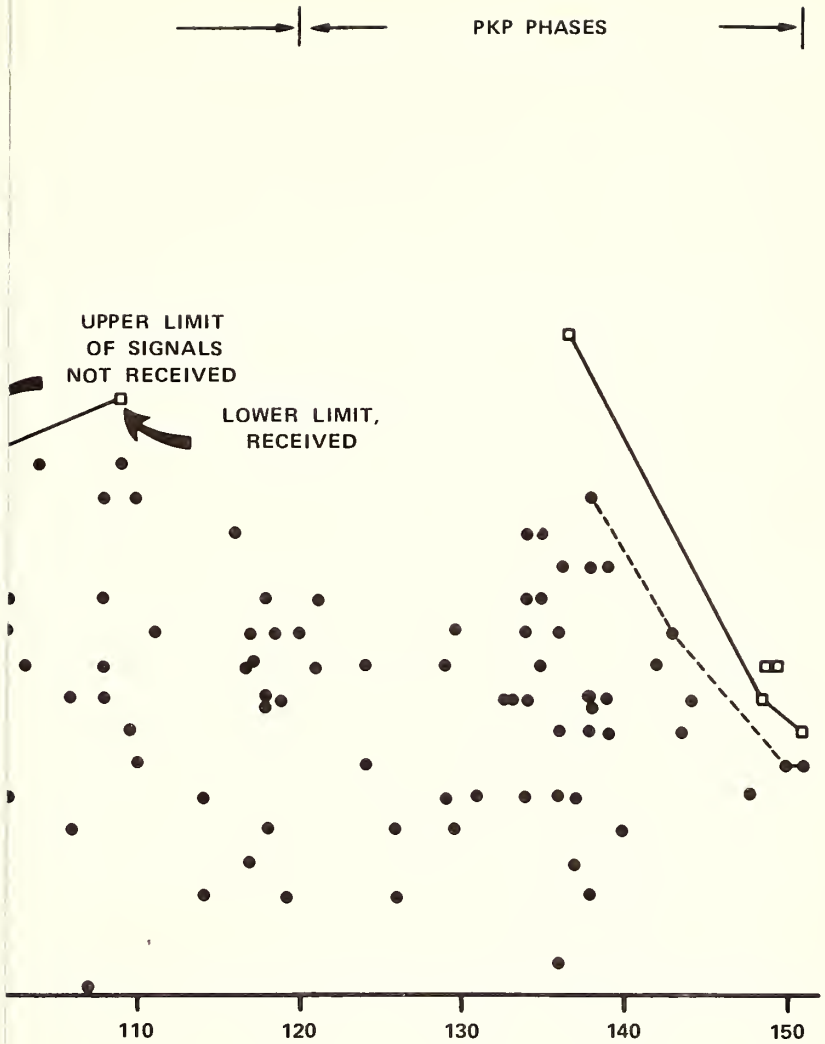

a single NORSAR seismometer for shallow trends are circled.

NORSAR,

(3) magnitude (m_b) of each earthquake, obtained from the PDE cards,

(4) epicentral distances from the center of NORSAR for each earthquake location given on the PDE cards, and

(5) the focal depth of each earthquake given on the PDE cards.

From each paper seismogram showing a clearly recorded earthquake signal, we measured the dominant signal frequency occurring within approximately 2 s after signal onset. An average signal frequency was then computed for each earthquake.

7.2 NORSAR Detection Threshold for Teleseisms

From the earthquake list described above, we constructed figure 7.1, which shows the detection threshold of a single NORSAR seismometer for shallow ($h \leq 50$ km) teleseisms, and figure 7.2, which shows the detection threshold for deep ($h > 50$ km) teleseisms. In these illustrations, trend lines describe both the upper magnitude limits of teleseisms not recorded and the lower magnitude limits of teleseisms recorded. In figure 7.1, the trend lines show the following three approximate linear trends: (1) the threshold increases from 4.6 at 20° to 4.8 at 68°, (2) the threshold increases from 4.9 at 80° to 5.7 at 100°, and (3) though poorly defined, the threshold decreases from approximately 5.8 at 137° to 4.8 at 150°. In the interval between 68° to 80°, the linear trends are interrupted by a decrease of approximately 0.5 unit, followed by an increase of approximately 0.5 unit. (These features are also shown in fig. 7.2, detection threshold of deep earthquakes). No shallow events were recorded in the range 110° to 136°. The detection threshold graph for deep events (fig. 7.2)

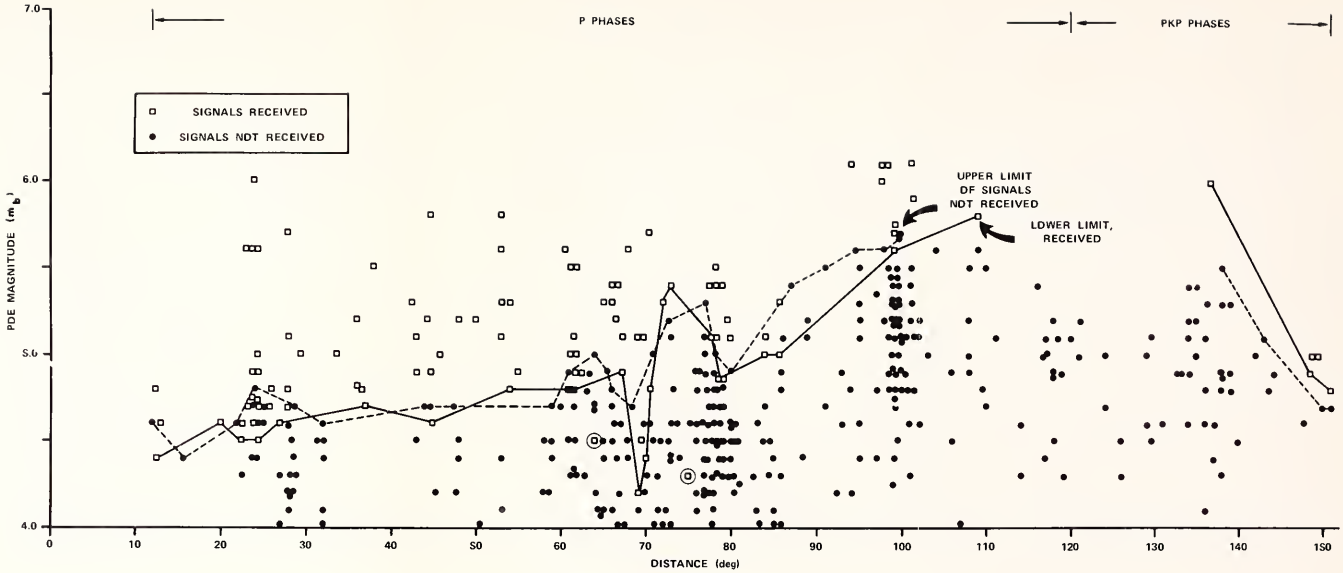

Figure 7.1. Detection threshold of a single NORSAR seismometer for shallow teleseisms. Deviations from the trends are circled.

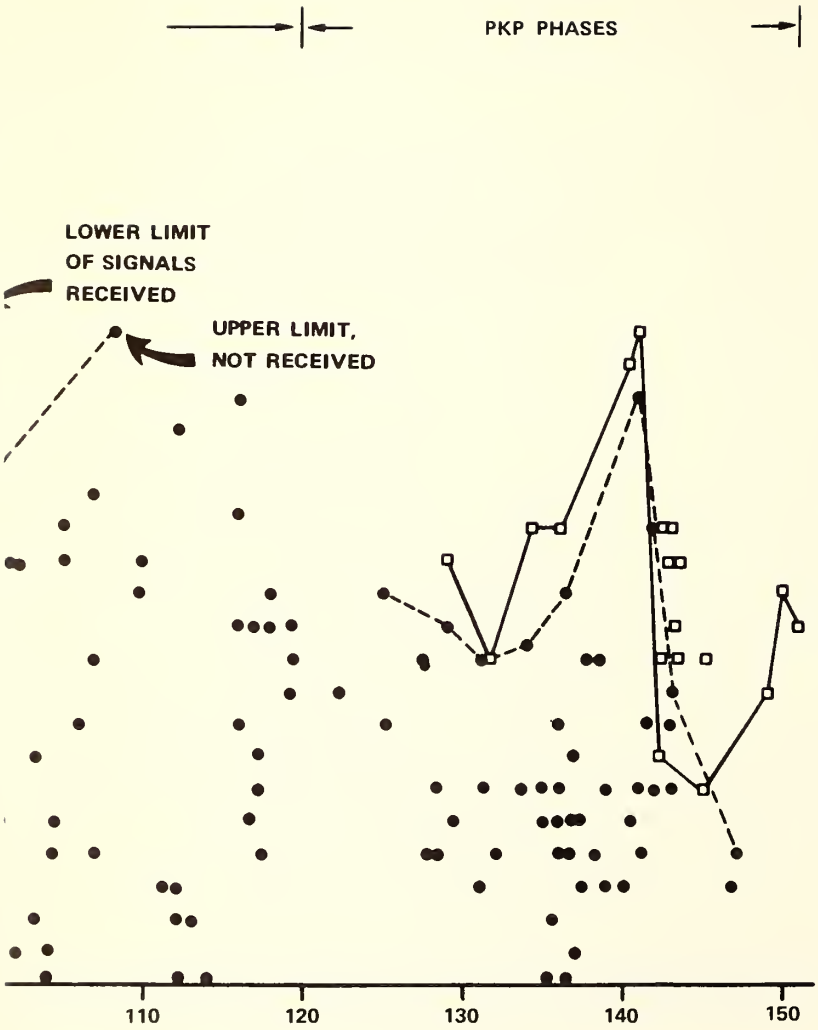
PKP PHASES
LOWER LIMIT
OF SIGNALS
RECEIVED
UPPER LIMIT,
NOT RECEIVED
110
120
130
140
150

shows trend lines somewhat similar to those in figure 7.1; in general, however, the trend lines are approximately 0.3 unit lower than those drawn for shallow events.

7.3 Average Signal Frequencies of Teleseisms

The density and distribution of the observed shallow teleseismic signal frequencies are displayed in figure 7.3. As depicted there, 90 percent of the average frequencies are in the band above 0.8 Hz; 85 percent are in the 0.8- to 2.0-Hz band; none are in the band above 2.4 Hz. Displays for signals received from deep earthquakes are given in figure 7.4. Here, 95 percent of the average frequencies are in the band above 0.8 Hz, and none are observed in the band above 3.2 Hz.

Figure 7.5 shows the average frequencies of shallow earthquake signals plotted as a function of their corresponding PDE-listed magnitudes for earthquakes having epicentral distances less than 90° from NORSAR. For earthquakes having magnitudes less than 5.0, approximately 80 percent show average frequencies in the 1- to 2-Hz band, with a range of 0.8 to 2.4 Hz. A similar display for deep earthquakes is given in figure 7.6, showing that they have signals mainly in the 1- to 3-Hz band, with a range of 0.9 to 3.2 Hz.

7.4 Discussion

By studying seismograms produced by a single sensor positioned in a 60-m well, Kelly (1966) investigated the detection threshold at the Large Aperture Seismic Array (LASA) site located in eastern Montana. From his study, made for the distance range 40° to 90° from LASA, he

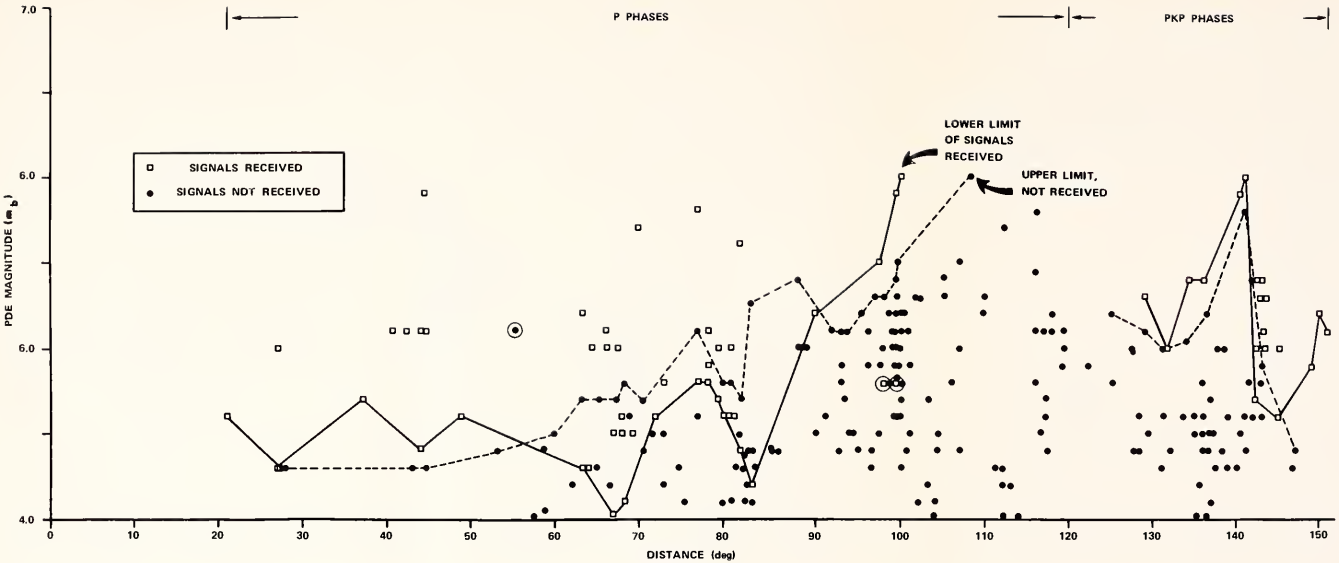

Figure 7.2. Detection threshold of a single NORSAR seismometer for deep teleseisms. Deviations from the trends are circled.

shows trend lines somewhat similar to those in figure 7.1; in general, however, the trend lines are approximately 0.3 unit lower than those drawn for shallow events.

7.3 Average Signal Frequencies of Teleseisms

The density and distribution of the observed shallow teleseismic signal frequencies are displayed in figure 7.3. As depicted there, 90 percent of the average frequencies are in the band above 0.8 Hz; 85 percent are in the 0.8- to 2.0-Hz band; none are in the band above 2.4 Hz. Displays for signals received from deep earthquakes are given in figure 7.4. Here, 95 percent of the average frequencies are in the band above 0.8 Hz, and none are observed in the band above 3.2 Hz.

Figure 7.5 shows the average frequencies of shallow earthquake signals plotted as a function of their corresponding PDE-listed magnitudes for earthquakes having epicentral distances less than 90° from NORSAR. For earthquakes having magnitudes less than 5.0, approximately 80 percent show average frequencies in the 1- to 2-Hz band, with a range of 0.8 to 2.4 Hz. A similar display for deep earthquakes is given in figure 7.6, showing that they have signals mainly in the 1- to 3-Hz band, with a range of 0.9 to 3.2 Hz.

7.4 Discussion

By studying seismograms produced by a single sensor positioned in a 60-m well, Kelly (1966) investigated the detection threshold at the Large Aperture Seismic Array (LASA) site located in eastern Montana. From his study, made for the distance range 40° to 90° from LASA, he

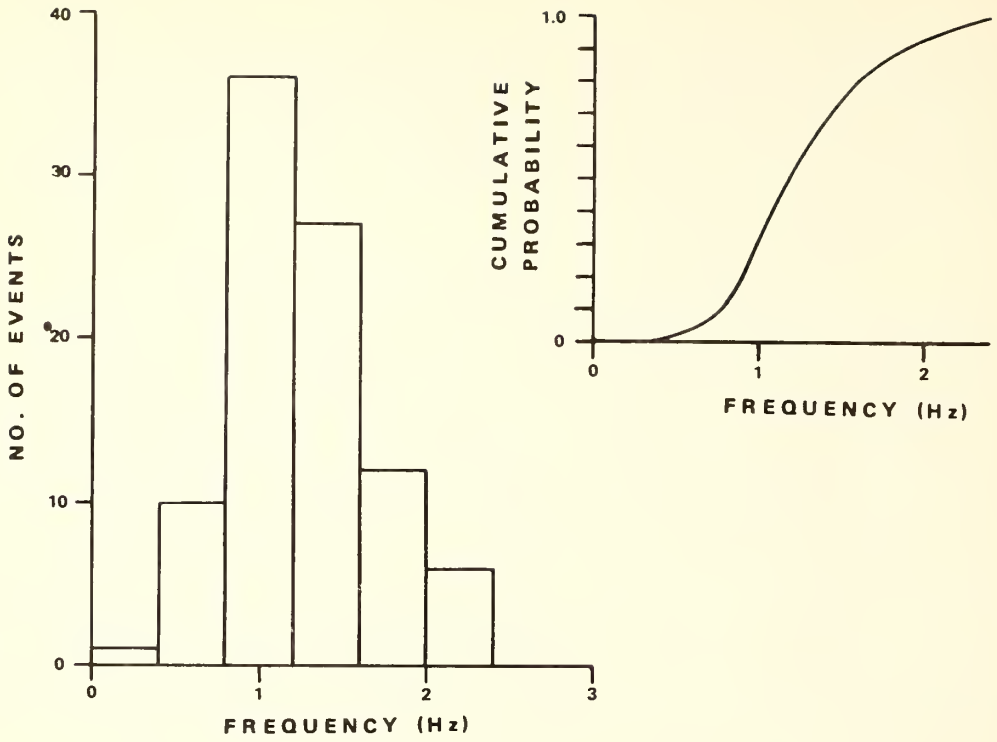

Figure 7.3. Density and distribution of shallow teleseimic signal frequencies.

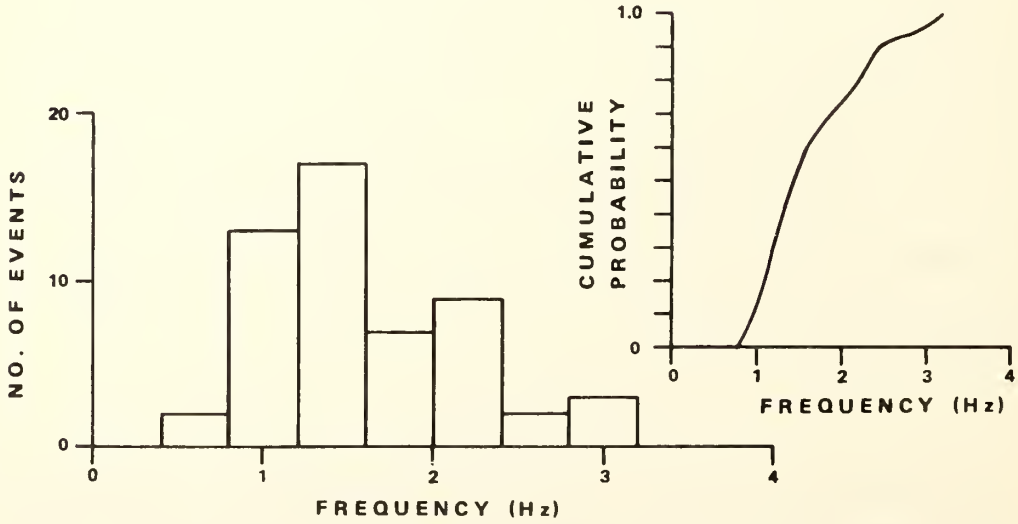

Figure 7.4. Density and distribution of deep teleseismic signal frequencies.

reported (p. 7):

> Our conclusion is that the 75% detection threshold on a single sensor is at a magnitude of..... 4.3 at the C. and G. S. level.

For the corresponding distance range, data portrayed in figure 7.1 (shallow teleseisms) suggest a detection threshold of 4.7 to 5.4 for NORSAR; we detected only 2 shallow events having a reported magnitude equal to, or less than, 4.3.

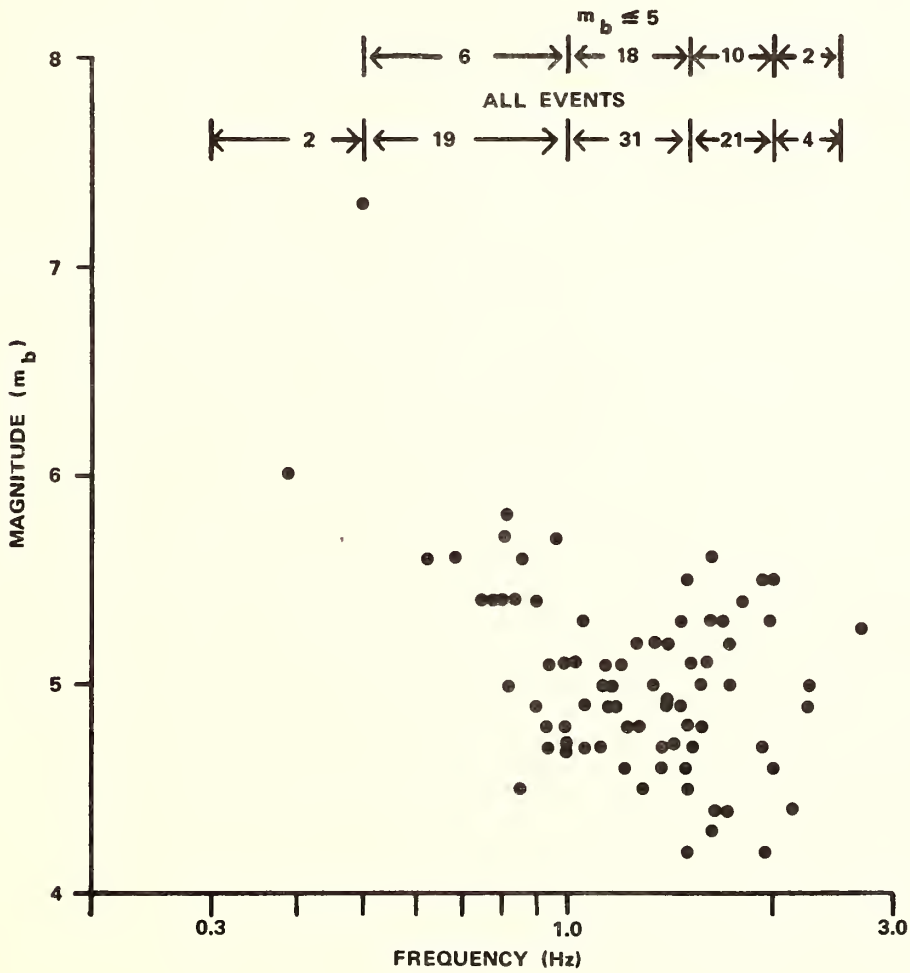

Figures 7.5. Signal frequencies of shallow teleseisms plotted as a function of their PDE-listed magnitudes.

Relative to the shallow events, deep events seem to show a lower detection threshold (figs. 7.1 and 7.2). The lower threshold is probably due, at least in part, to the relatively higher signal frequencies of the deep events. In general, the microseism amplitudes decrease proportionally to an increase in frequency, producing a better signal-to-noise ratio for deep events than for shallow events.

We must emphasize that the frequencies described in this section are average values. Some shallow teleseismic recordings showed frequencies as high as 3.5 Hz.

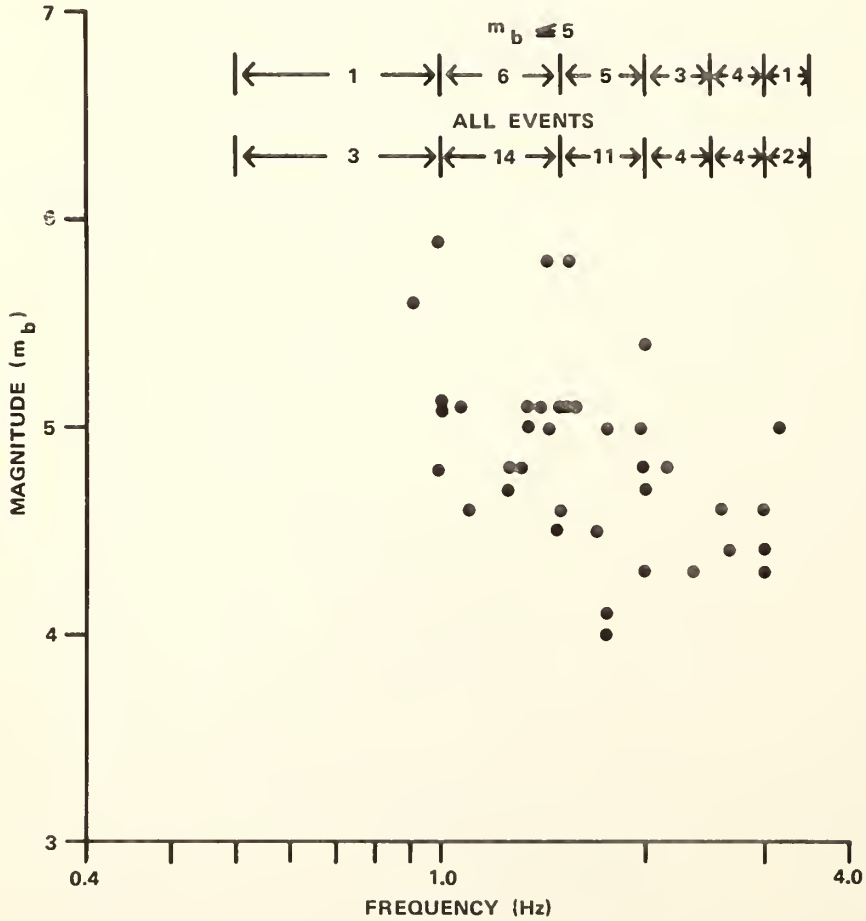

Figure 7.6. Signal frequencies of deep teleseisms plotted as a function of their PDE-listed magnitudes.

8. SUMMARY

The following is a summary of observations and interpretations made from a study of seismic data recorded by EML at NORSAR:

(1) Quite small differences exist between the surface and subsurface (-60 m) microseismic field, even during times of high wind velocity. For the dominant P signal band (0.8 to 2.0 Hz), the surface and subsurface field normally differs by less than 1 dB (see figs. 3.2 to 3.11, and seismograms shown in app.). Environment of a typical recording site is illustrated in figure 2.2; the EML instrument package, in figure A.1; the responses, in figure A.2.

(2) Teleseismic signals produce almost identical recordings from the surface and subsurface seismometers (see fig. 3.12).

(3) Between adjacent subarray sensors, the coherence of microseisms, in the P signal band, approaches values we estimate for unrelated samples (see figs. 5.10, 5.2 to 5.9). As indicated by the coherence polygons (defined in section 5.1), the coherence has a strong azimuthal dependency.

(4) We interpret the NORSAR noise field to be an interference process (fig. 5.14), composed of waves approaching from a broad band of azimuths. A mathematical model of the noise field (sec. 5.3) produces coherence graphs similar to those estimated from the real data (compare figs. 5.11 and 5.16). For a constant model velocity the computed time delays are frequency dependent (fig. 5.18).

(5) The NORSAR microseismic field is approximately space stationary (see figs. 4.1 through 4.4).

(6) The average microseismic amplitude at 1.0 Hz is approximately 6 mμ/Hz RMS (sec. 4.3).

(7) There is a weak correlation between microseismic trends and regional barometric gradient trends (figs. 6.6, 6.7, and 6.8). Similar correlations were found by us and others by studying data EML recorded in Australia (see figs. 6.4 and 6.5).

(8) Approximately 90 percent of the shallow teleseisms recorded have average signal frequencies (estimated from paper seismograms) greater than 0.8 Hz; 85 percent of the average frequencies are in the 0.8- to 2.0-Hz band (see fig. 7.3). Signal frequency may increase as a function of decreasing source magnitude (see figs. 7.5 and 7.6).

(9) For the distance range 20° to 90°, the single seismometer shallow-teleseism P detection threshold ranges from 4.6 to 5.4 m_b; the threshold for deep earthquakes is somewhat lower (see figs. 7.1 and 7.2).

9. ACKNOWLEDGMENTS

This work was supported by the Advanced Research Projects Agency (ARPA) and was monitored by the Electronics Systems Division of the United States Air Force. Mr. Rudolph Black of ARPA, and Lt. Col. W. R. Lauterbach, ESD Program Manager, defined the broad project objectives and participated in program planning. During the interpretation phase of the

project, Lt. Col. J. X. Brennan was the ESD Program Manager. The Norway field program was coordinated by Major Ø. Brandtzæg of the Norwegian Defense Research Establishment, and Lt. Col. N. Orsini, assisted by Captain R. Jedlicka (both of ESD). The EML efforts were guided by Dr. Don Tocher, Director.

Professor Markvard A. Sellevoll, Director of the Seismological Observatory at the University of Bergen, contributed support including the use of his playback facility. Our discussions with him and his staff were very informative; particularly stimulating were those with Professor Sellevoll and Messrs. Hilman Bungum, Leif Bruland, Eivind Rygg, and Reidar Kanestrøm. The cooperation of Professor Sellevoll allowed data presentations to the NORSAR managers during March 1969, and permitted quality control tests of the EML gear during the field program.

Mr. Lars Dalland of Tele-plan worked with the EML field crew, providing engineering consultation and acting as liaison with the construction crews. The Tele-plan tests, calibrations, and other contributions were directed by Mr. Thorbjørn Johansen, assisted by Mr. Bjarne Goplen and Mr. Gunnar Hansen. The cooperation of Mr. Johansen and Mr. Dalland permitted our success in data aquisition.

EML personnel who made contributions included Lt. Thomas Kalil, who performed almost all of the EML data reduction and quality control at the University of Bergen facility, and who advised and assisted in preparation, installation, and maintenance of the EML instruments; Mr. Ralph Humphrey, who, to make our equipment NORSAR compatible, designed new instruments, modified existing ones, and also supervised instrument con-

struction, preparation, and installation; Mr. Erick Young and Ensign Raymond Reilly, who wrote computer programs, reduced a large portion of the data at EML, and made valuable suggestions that were incorporated into the data reduction and analysis programs; Mr. Michael Blackford, who modifield the spectral analyses program; and Mr. Wesley Hall, who assisted Mr. Humphrey in construction and preparation of EML instruments; Miss Nancy Crossley and Miss Susan Larson, who prepared the manuscript.

Almost all of the artwork and drafting was by Mrs. Patricia Sposato, who also contributed technical assistance.

10. REFERENCES

Backus, Milo, John Burg, Dick Baldwin, and Ed Bryan (1964), Wide-band extraction of mantle P waves from ambient noise, Geophysics, XXIX, No. 5, 692.

Bendat, Julius S., and Allan G. Piersol (1964), Design considerations and use of analog power spectral density analyzers, Minneapolis-Honeywell Regulator Company, Denver, Colorado.

Bungum, Hilmar, Leif Bruland, and Eivind Rygg (1969), Seismic noise structure at the Norwegian Seismic Array, Sci. Rept. No. 4, Seismological Observatory, University of Bergen, Bergen, Norway.

Hasselmann, K. (1963), A statistical analysis of the generation of microseisms, Rev. Geophys., 1, No. 2, 177-210.

Jenkins, Gwilym M., and Donald G. Watts (1968), Spectral Analysis and Its Applications (Holden-Day, San Francisco, California).

Kelly, E. J. (1966), LASA on-line detection, location and signal-to-noise enhancement, Tech. note 1966-36, Lincoln Laboratory, Lexington, Massachusetts.

Longuet-Higgins, M. S. (1950), A theory on the origin of microseisms, Phil. Trans. Roy. Soc. London, A, 243, 1-35.

Longuet-Higgins, M. S. (1952), Can sea waves cause microseisms? Symposium on microseisms, U. S. Natl. Acad. Sci. Publ. 306, 74-93.

Murdock, James N., John H. Pfluke, Roger Kraynick, Michael E. Blackford, and James D. Van Wormer (1968), Microseisms and teleseisms recorded in Australia, ESSA Tech. Rept. ERL 66-ESL 4 (U.S. Government Printing Office, Washington, D.C.).

Rygg, Eivind, Hilmar Bungum, and Leif Bruland (1969), Spectral analysis and statistical properties of microseisms at NORSAR, Sci. Rept. No. 1, Seismological Observatory, University of Bergen, Bergen, Norway.

Santô, Tetsuo A. (1962), Energy sources of microseisms in Sweden, Annali de Geophysica, XV, No. 4, 335-377.

APPENDIX

A.1 Field Instrumentation, Field Tests, and System Frequency Responses

The following describe the NORSAR and EML systems:

Seismometers:	Hall-Sears HS-10-1/A.
NORSAR Seismic Data Amplifiers:	Texas Instruments Incorporated Model RA-5 (located in the vaults).
EML Seismic Data Amplifiers:	Constructed by EML.
Anemometers:	Climet Model 011-1. Output frequency proportional to wind velocity.
Primary Time Base Generators:	Astrodata Model 6195 time code generator, 100-Hz carrier, directly recorded.
Tape Recorders:	Precision Instruments Model 5100, record speed 15/160 ips, FM center frequency 84.4 Hz.

The following describe field tests and system frequency responses:

System Calibrations:	Signal generator sine waves (20.0 V P-P) normally for frequencies of 0.3, 0.5,

	0.8, 1.0, 1.2, 1.5, 2.0, 4.0, 8.0, 10.0 Hz. Normally made for each NORSAR element every 10 days.
NORSAR Seismic Data Amplifier Calibrations:	Same as above, but with seismometer-equivalent impedence emplaced at input to the amplifiers. Also, gain tests at 1.0 Hz performed at 10-day intervals.
EML Seismic Data Amplifiers:	Gain tests made at 10-day intervals, 1.0 Hz.
Seismometer Free Period:	1.0 Hz, from Lissajous pattern and frequency response tests conducted by Tele-plan, a NORSAR contractor.
System Noise Tests:	Seismometer-equivalent impedence emplaced at input to NORSAR amplifiers. Normally, conducted at 10-day intervals for each element.
Compensation:	For power spectral density estimates and seismogram displays--none For coherence estimates--discriminator center frequency controlled by frequency of time code carrier.
Filter Settings for Digitizing:	For power spectral density estimates only--low pass at 5.5 Hz, 36 dB/octave.

For coherence estimates--low pass at 2.2 Hz, 36 dB/octave.

Anemometer Channel Calibrations: Electrical analog of the anemometer output made for wind velocities of 1 to 30 mph. One test made for each system.

The EML field system is displayed in figure A.1. Typical system frequency responses, computed from the composite field calibrations of EML and Tele-plan, are given in figure A.2. Shown are frequency responses for the NORSAR-EML system, the NORSAR-EML University of Bergen system, and for the NORSAR-EML-GDC (General Dynamics Corporation, the digitizing contractor) system. Not shown is the NORSAR-EML-GDC system used for digitizing data for coherence estimates; the 3-dB point for it is at 2.2 Hz, 36 dB/octave.

A.2 Digital Data Reduction

Program: Written at ESSA Research Laboratories, Boulder, Colorado. Modified for EML use by Harold Williams and Roger Kraynick under the direction of John H. Pfluke. Literature referenced: Blackman and Tukey, 1958.

Sample length: For power spectral density estimates--170 s sampled at 20 samples/s, 511 digital counts for full FM deviation.

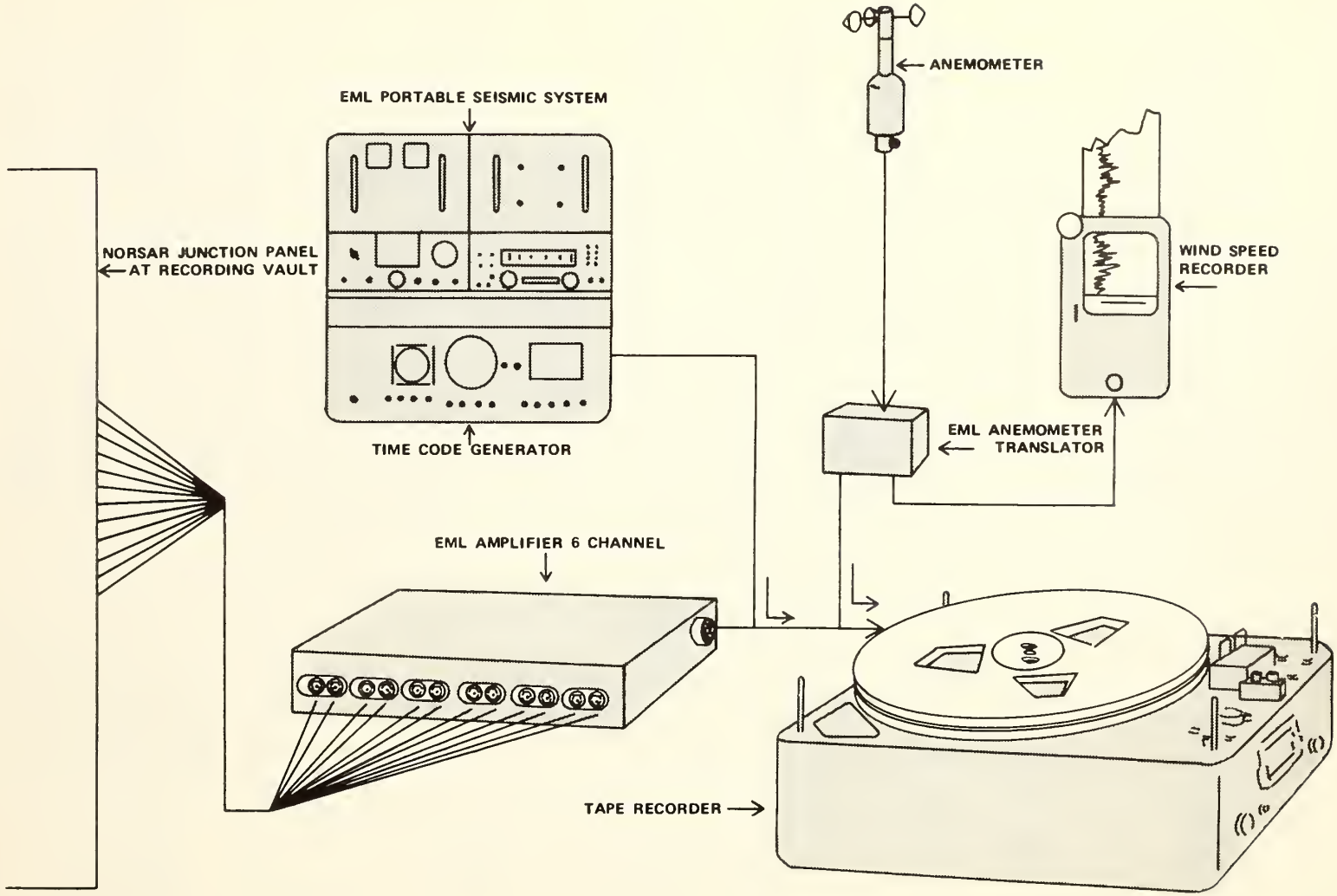

Figure A.1. Artist's concept of EML instrumentation at the recording vault.

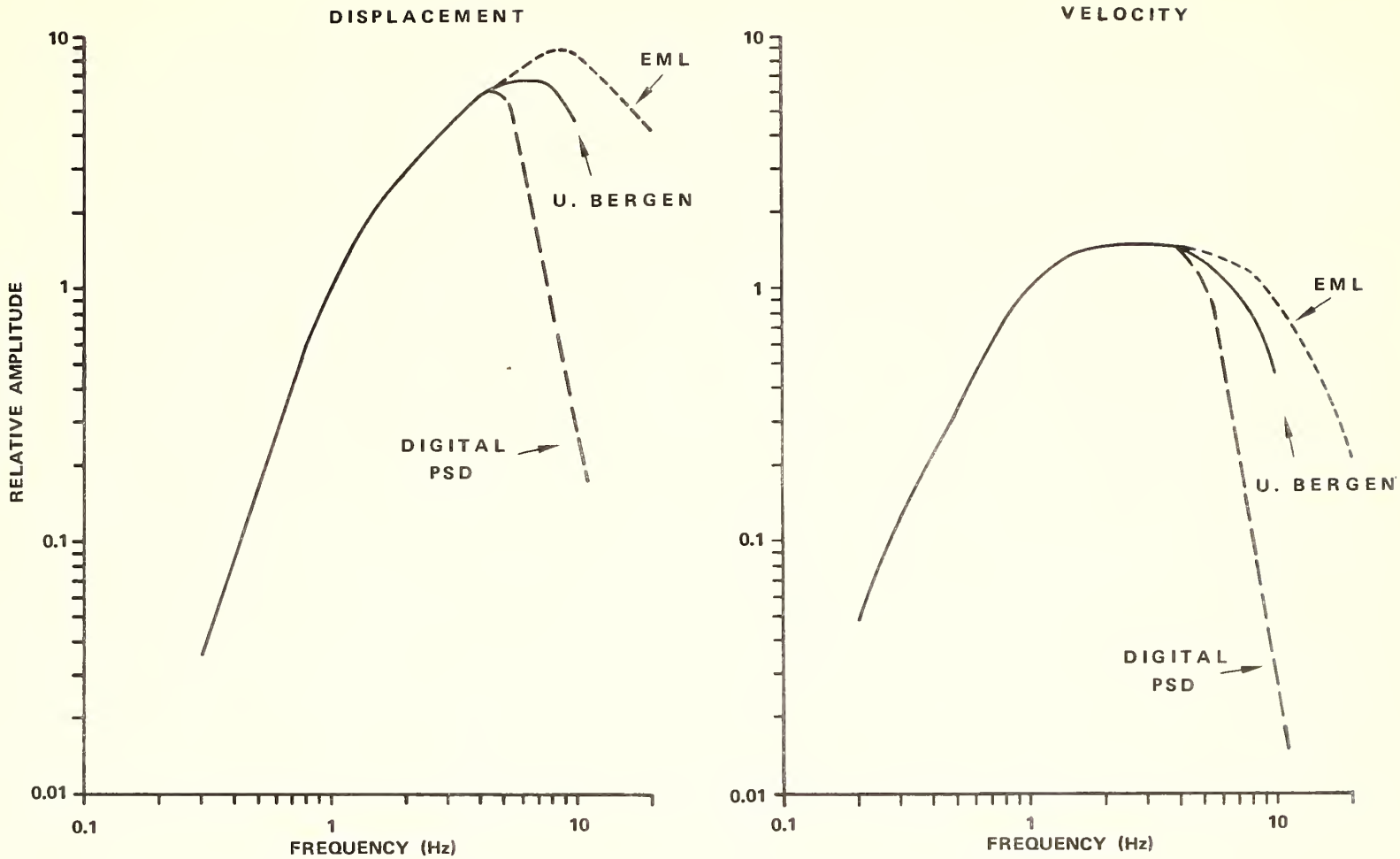

Figure A.2. Typical frequency responses for the different systems. Shown are the EML responses, the EML-University of Bergen responses, and the EML-GDC (labeled "digital PSD") responses.

For coherence estimates--340 s sampled at 10 samples/s, 511 digital counts for full FM deviation.

Prewhitening: $A_k = 0.5\ A_k - 0.5\ A_{k+1}$. A_k is the amplitude of the kth point of the time series.

Spectral Estimates: From auto-correlation and cross-correlation estimates.

Number of Lags: 100.

Smoothing Parzen lag window.

$$1 - 6\frac{k^2}{m^2} + 6\frac{k^3}{m^3},\ k \leq \frac{m}{2}$$

$$2\left(1-\frac{k}{m}\right)^3,\ \frac{m}{2} < k \leq m,$$

where m = number of lags, and

k = point number of the lag window.

Spectral Computations: For power spectral density estimates--at each 0.1-Hz interval from 0.1 Hz to 10 Hz.

For coherence estimates-- at each 0.5-Hz interval from 0.05 Hz to 5.0 Hz.

Magnification Corrections: From computed magnification at 1.0 Hz

Frequency Response Corrections: Normally none. For difference estimates, subsurface data channels normalized to their respective surface (LPV) channels.

Computer: Control Data Corporation Model 3600.

A test for the probability density distribution of a typical microseism sample (fig. A.3) approximates a Gaussian curve.

A.3 Seismograms Recorded During Times of High Wind Velocities

The seismograms displayed in this section depict microseisms recorded during times of high wind velocity. The subsurface recording is the first seismic trace of each seismogram; the surface, LPV-emplaced seismometer, is the second trace. The maps in section 5 show the sensor positions. Arrows on the seismograms indicate the time the highest wind gust was recorded, and the velocity of the gust is noted. Average wind velocities were as follows:

Sub-array	Average Wind mph
01A	10
01B	15
02B	10
03B	12

A.4 Reference

Blackman, R.B. and J.W. Tukey (1958), the Measurement of Power Spectra, Dover Publications, New York.

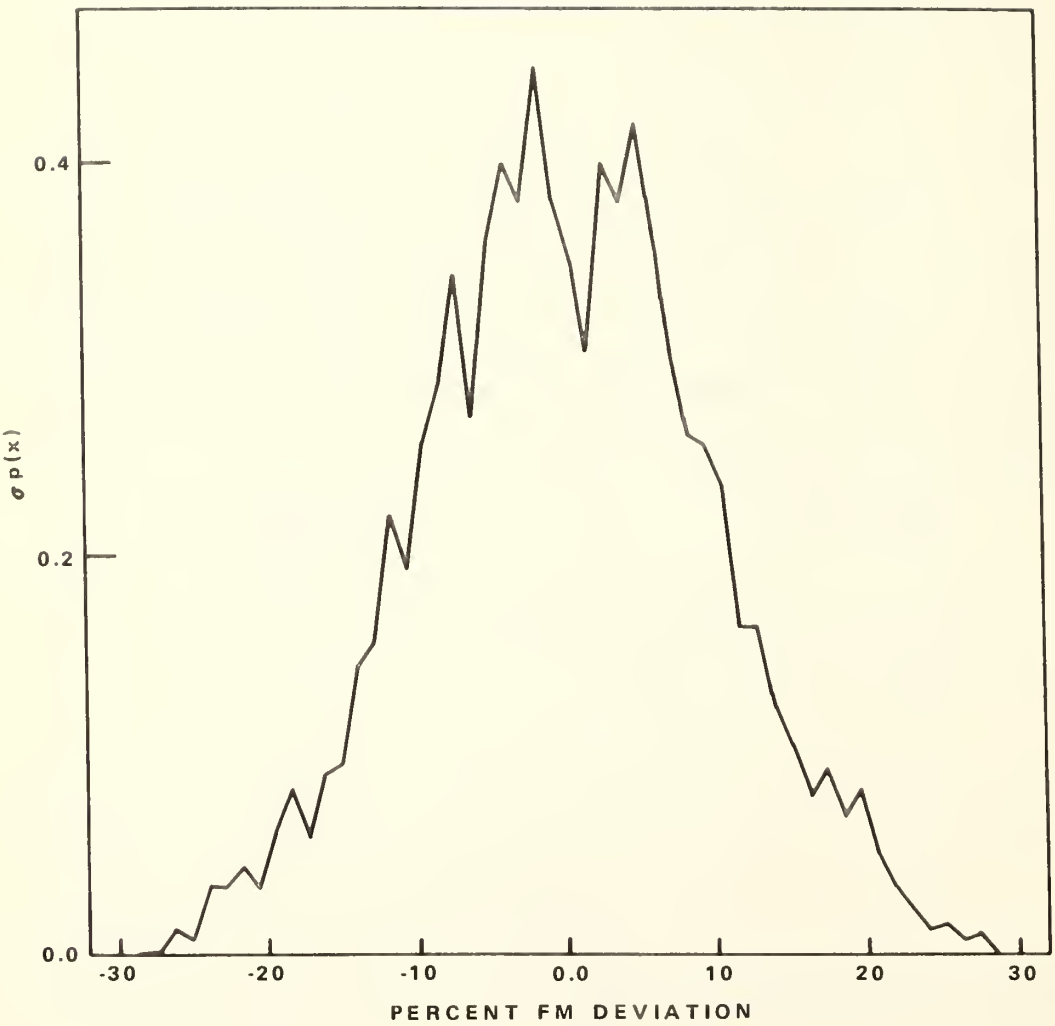

Figure A.3. Probability density distribution of a typical microseism sample.

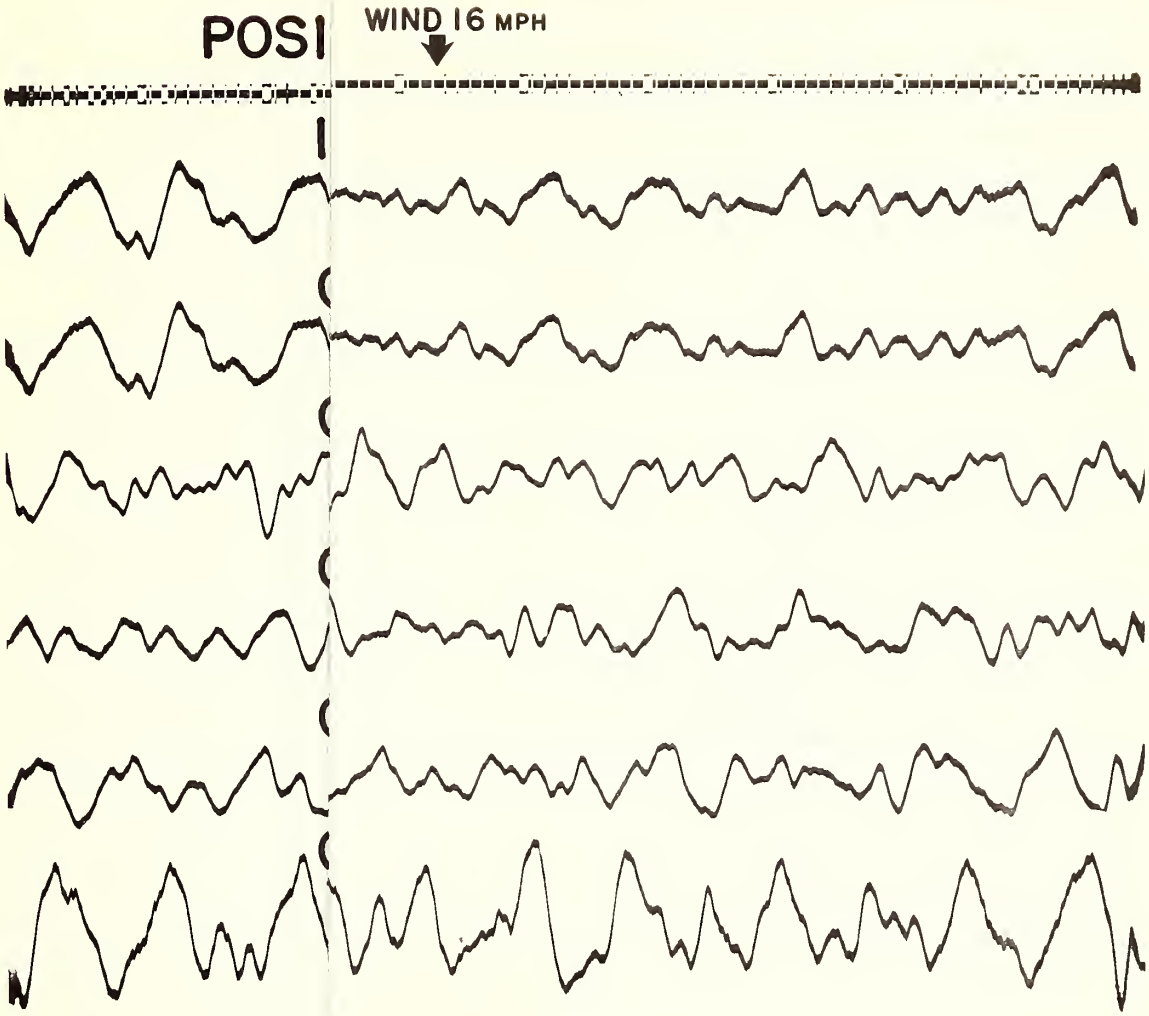

SEISMOGRAM 0-1a

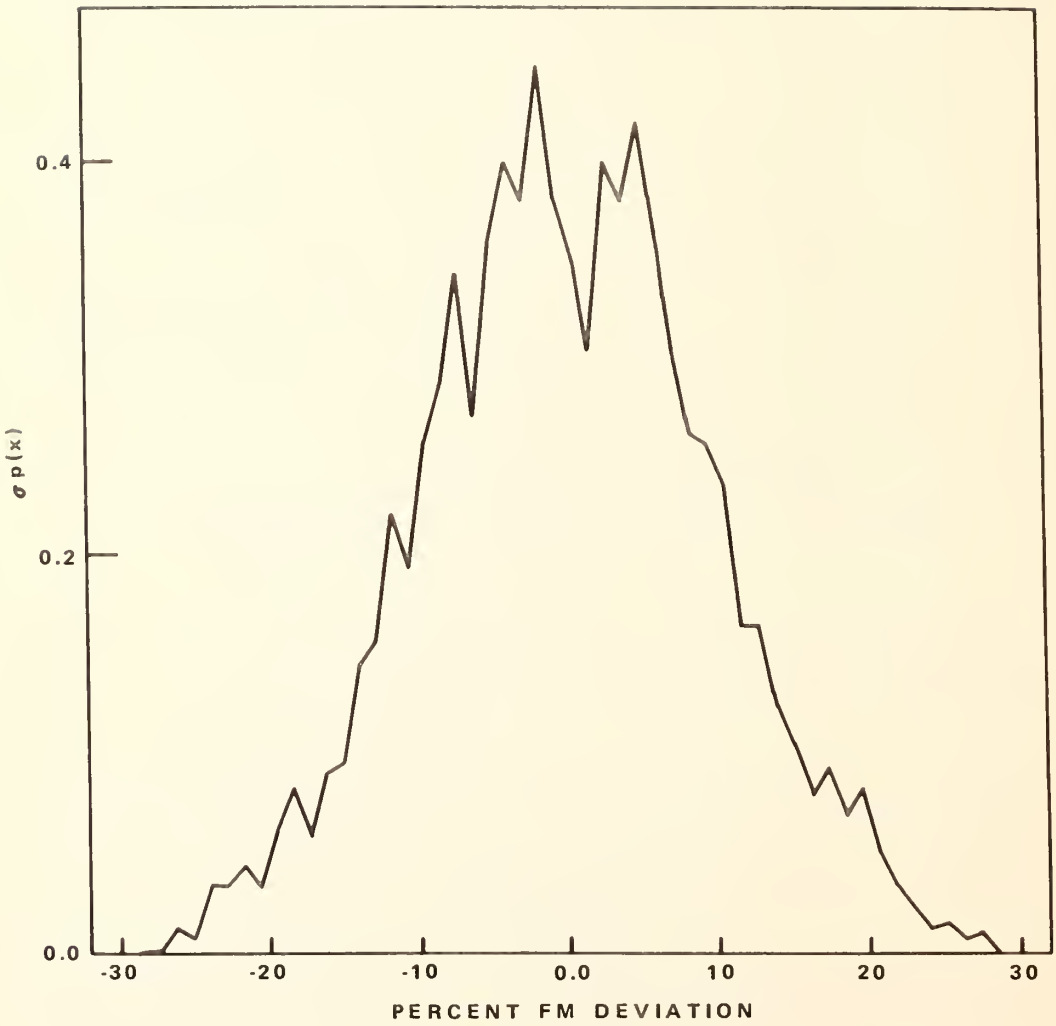

Figure A.3. Probability density distribution of a typical microseism sample.

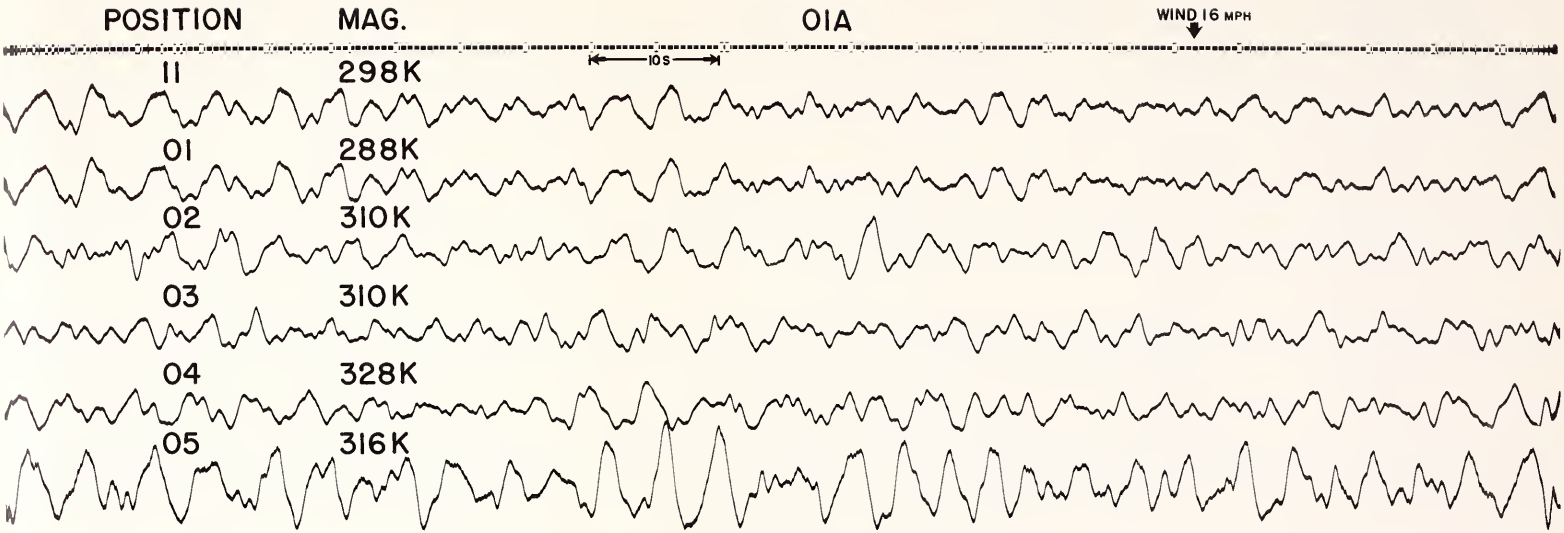

SEISMOGRAM 0-1a

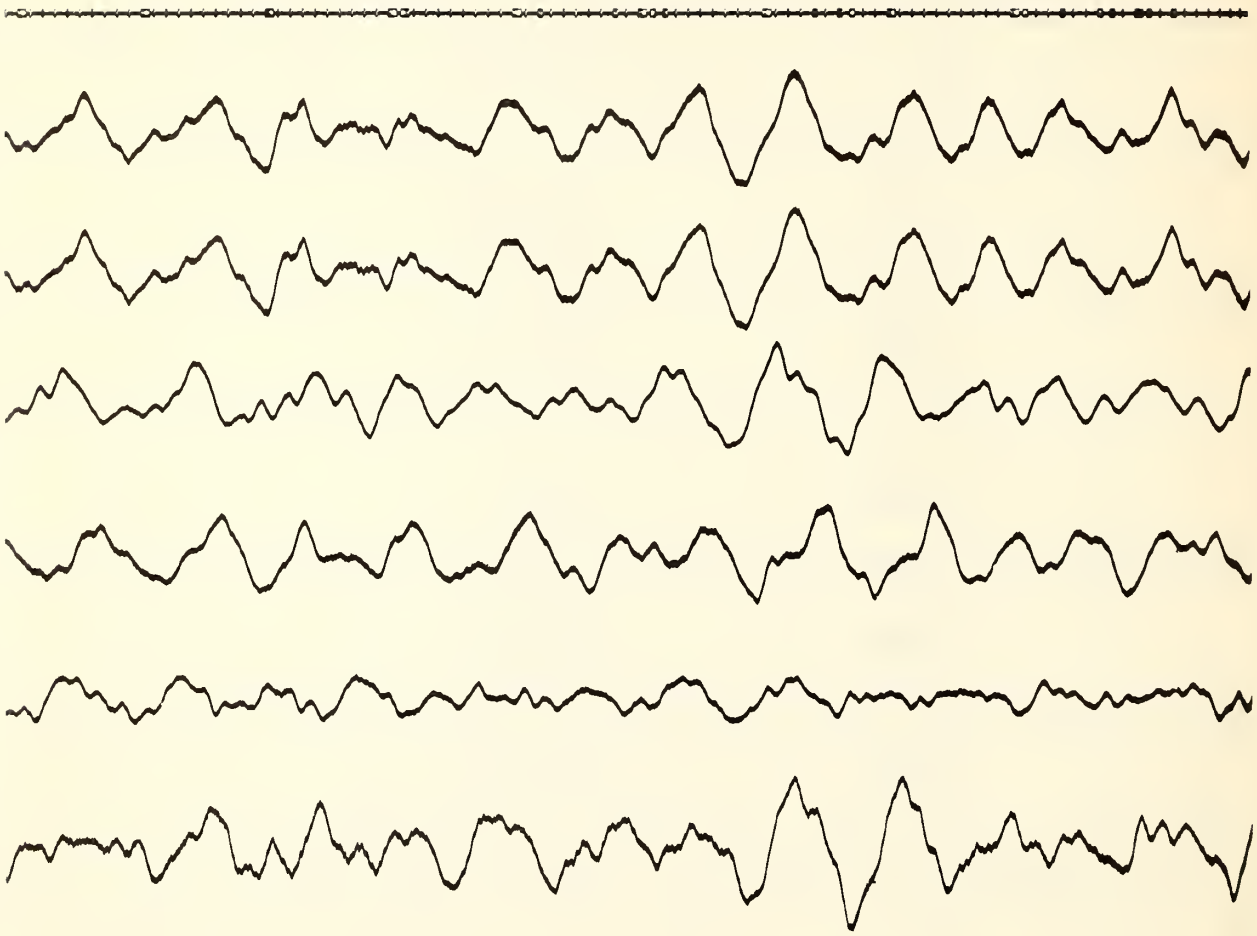

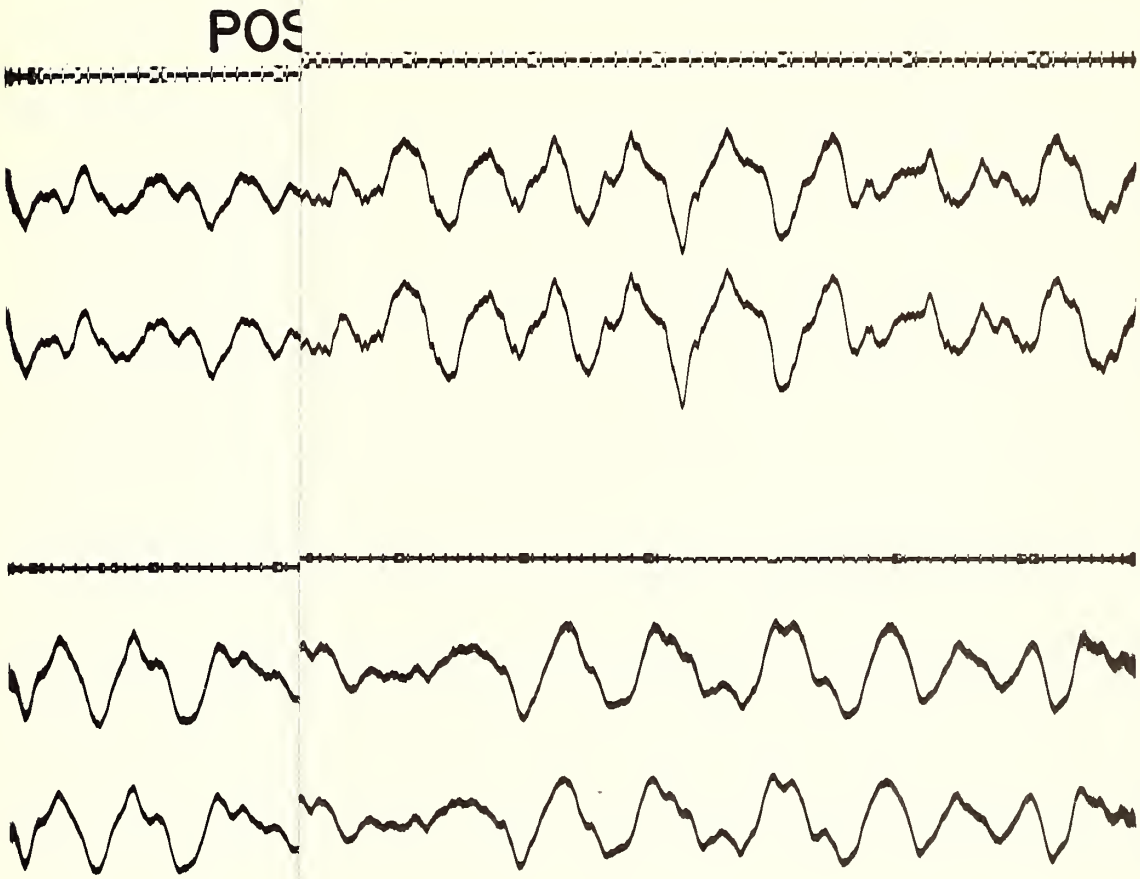

SEISMOGRAM 0-2b

GPO 830-195

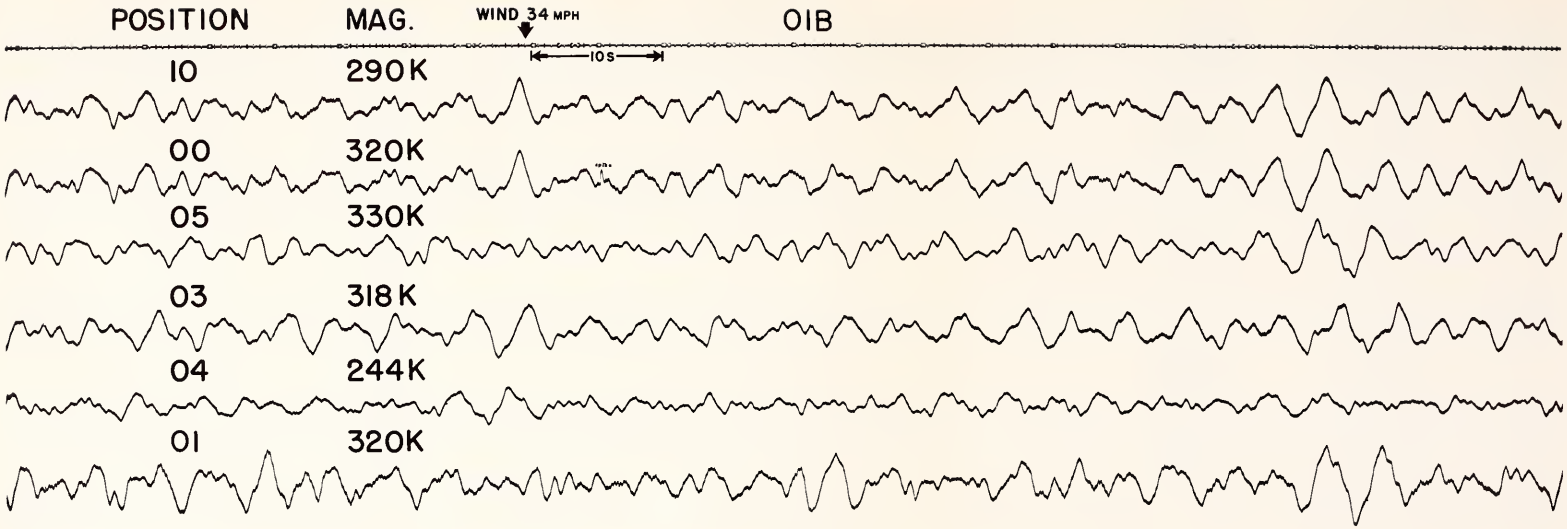

SEISMOGRAM 0-1b

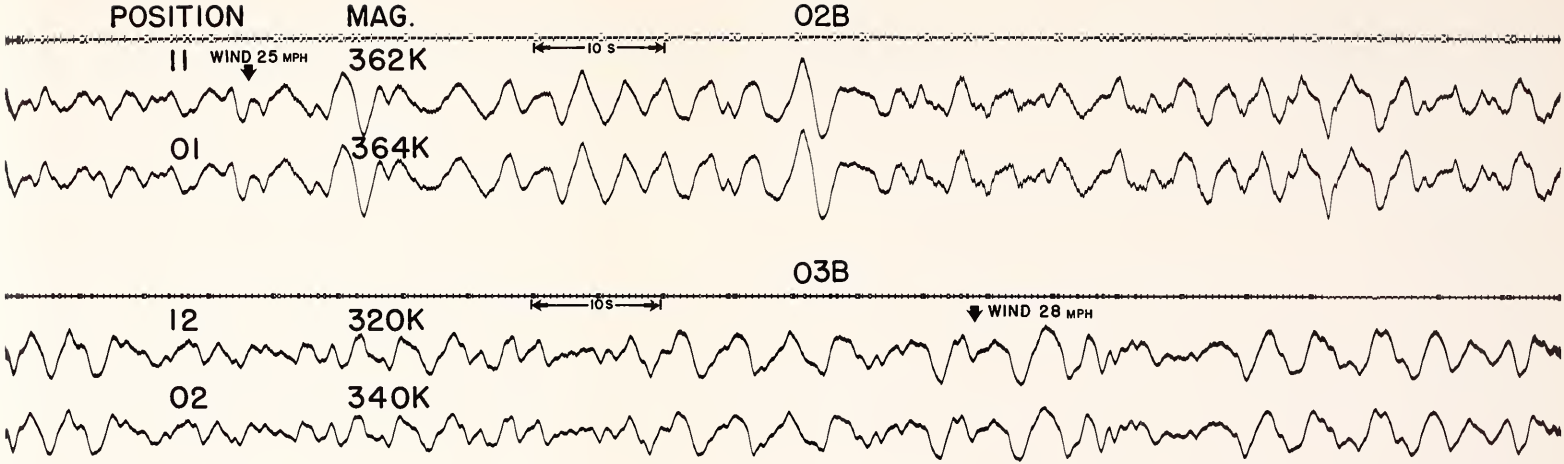

SEISMOGRAM 0-2b

GPO 830-195

PENN STATE UNIVERSITY LIBRARIES
A000072020128